UNIVERSITY OF CALIFORNIA, SAN DIEGO

Continuous surface ocean measurements of dissolved oxygen isotopes

A dissertation submitted in partial satisfaction of the
requirements for the degree
Doctor of Philosophy

in

Oceanography

by

Lauren Elmegreen Rafelski

Committee in charge:

Professor Ralph Keeling, Chair
Professor Lihini Aluwihare
Doctor Ralf Goericke
Professor Jeffrey Severinghaus
Professor Mark Thiemens
Professor Ray Weiss

2012

The dissertation of Lauren Elmegreen Rafelski is approved, and it is acceptable in quality and form for publication on microfilm and electronically:

_____

_____

_____

_____

_____

_____
Chair

University of California, San Diego

2012

EPIGRAPH

It is a capital mistake to theorize before one has data.
Insensibly one begins to twist facts to suit theories,
instead of theories to suit facts.
—Sir Arthur Conan Doyle, The Adventures of Sherlock Holmes

TABLE OF CONTENTS

Signature Page iii

Epigraph iv

Table of Contents v

List of Figures viii

List of Tables x

Acknowledgements xi

Vita and Publications xiii

Abstract of the Dissertation xiv

Chapter 1 Introduction 1
1.1 The carbon cycle 1
1.2 Methods of measuring primary production 2
1.3 The use of oxygen isotopes to measure production 4
1.4 Overview of this thesis 6
References 9

Chapter 2 An equilibrator to measure dissolved oxygen and its isotopes . 14
2.1 Introduction 14
2.2 Methods 18
2.2.1 Mass spectrometer 18
2.2.2 Equilibrator 19
2.2.3 Gas tension device 23
2.2.4 Field setup 25
2.3 Mathematical model of equilibrator 28
2.4 Results 33
2.4.1 Equilibration time of the equilibrator 33
2.4.2 Corrections for incomplete equilibration 35
2.4.3 Verification of model-based correction 39
2.4.4 Equilibration time of the GTD 41
2.4.5 Accuracy of the GTD 41
2.5 Discussion 44
2.6 Conclusions 46
2.7 Acknowledgements 47
References 48

Chapter 3 Mass spectrometer methods for measuring dissolved oxygen isotopes . . . 52
3.1 Introduction . . . 52
3.2 Sampling method . . . 53
3.3 Interferences . . . 56
3.3.1 Nitrogen . . . 57
3.3.2 Carbon dioxide . . . 59
3.3.3 Water vapor . . . 61
3.3.4 Dimethyl Sulfide . . . 63
3.4 Corrections to data . . . 65
3.5 Conclusions . . . 67
3.6 Acknowledgements . . . 68
References . . . 69

Chapter 4 Measurements of O_2 and $\delta^{18}O$ in the Southern California coastal ocean . . . 71
4.1 Introduction . . . 71
4.2 Methods . . . 73
4.3 O_2 and $\delta^{18}O$ model . . . 76
4.4 Experimental results . . . 78
4.4.1 Timeseries of O_2 and $\delta^{18}O$ . . . 78
4.4.2 Observed diurnal cycle . . . 82
4.4.3 Observed relationship between biological O_2 concentration and $\delta^{18}O$ . . . 83
4.5 Model results . . . 88
4.5.1 Modeled diurnal cycle . . . 88
4.5.2 Modeled relationship between O_2 and $\delta^{18}O$ . . . 95
4.6 Discussion . . . 98
4.7 Conclusions . . . 102
4.8 Acknowledgements . . . 102
References . . . 103

Chapter 5 Measurements of $^{17}\Delta$ in the coastal surface ocean . . . 108
5.1 Introduction . . . 108
5.2 Methods . . . 110
5.2.1 Nonlinear correction . . . 110
5.2.2 Filtering of $\delta^{17}O$ . . . 112
5.3 Model . . . 114
5.4 Results . . . 116
5.4.1 Observed $^{17}\Delta$ . . . 116
5.4.2 Modeled $^{17}\Delta$ . . . 118
5.4.3 Production calculations . . . 120
5.5 Discussion . . . 121

5.6 Conclusions 124
5.7 Acknowledgements 125
References 126

Chapter 6 Climate effects on atmospheric carbon dioxide over the last century 129
6.1 Introduction 129
6.2 Methods 133
6.2.1 Description of data 133
6.2.2 Ocean model 134
6.2.3 Land model 136
6.3 Results 138
6.3.1 Residual flux from deconvolution 138
6.3.2 Temperature-independent model 139
6.3.3 Temperature-dependent model 143
6.3.4 Sensitivity analyses 143
6.3.5 Adjustment of ice core data 152
6.4 Discussion 154
6.5 Conclusions 158
6.6 Acknowledgements 159
References 160

LIST OF FIGURES

Figure 2.1: Flow diagram for the mass spectrometer inlet 20
Figure 2.2: Equilibrator used to measure dissolved oxygen 22
Figure 2.3: Air flow in the pressure-controlled equilibrator loop 24
Figure 2.4: Schematic of the gas tension device 26
Figure 2.5: Water flow at the Scripps Institution of Oceanography pier . . . 27
Figure 2.6: Model of gas transfer between the water and headspace 30
Figure 2.7: Response in $\delta(Ar/N_2)$ to N_2 gas addition 34
Figure 2.8: Response of the time constant for $\delta(Ar/N_2)$ to k_{O_2} 36
Figure 2.9: Model prediction of the sensitivities of $\delta(O_2/N_2)$, $\delta(O_2/Ar)$, $\delta^{18}O$, and $\Delta^{17}O$ to equilibrator pressure changes and gas composition changes 38
Figure 2.10: Percent oxygen saturation measured with the optode and the mass spectrometer 42
Figure 2.11: Gas tension device response after a pressure perturbation . . . 43
Figure 2.12: Gas tension measured from the gas tension device, and calculated using optode and mass spectrometer measurements 44

Figure 3.1: Custom mass spectrometer inlet system, with a nitrogen bleed into the sample line 55
Figure 3.2: Nitrogen interference on $\delta(33/32)$ and $\delta(34/32)$ measured on cylinder air 58
Figure 3.3: Nitrogen interference on $\delta(33/32)$ and $\delta(34/32)$ measured from equilibrated air 59
Figure 3.4: Interference in $\Delta^{17}O$ from water vapor 62
Figure 3.5: Raw m/z 18 signal, and the timing of the changeover valve . . . 64
Figure 3.6: Phase shift of m/z 18 data 64

Figure 4.1: One-box model of biological O_2 concentration 77
Figure 4.2: O_2 and $\delta^{18}O$ timeseries from the SIO pier 79
Figure 4.3: O_2 and $\delta^{18}O$ shown as a function of time and date 81
Figure 4.4: Temperature profile 82
Figure 4.5: Periodogram of O_2 and $\delta^{18}O$ 84
Figure 4.6: Mean diurnal cycle in biological O_2 concentration, $\delta^{18}O$, PAR, salinity and chlorophyll. 85
Figure 4.7: O_2 and $\delta^{18}O$ data compared with previous measurements 86
Figure 4.8: Relationship between biological O_2 concentration and $\delta^{18}O$ . . . 87
Figure 4.9: Mean diurnal cycle in O_2 and $\delta^{18}O$ for different regimes 88
Figure 4.10: O_2 profiles from the August 2011 CalCOFI cruise 91
Figure 4.11: Mean diurnal cycle in water temperature, with depth 92
Figure 4.12: Mean measured diurnal cycle and modeled diurnal cycle 94
Figure 4.13: Modeled diurnal cycle for a doubling of the photosynthesis rate 96

Figure 4.14: Evolution of a water parcel starting at 90% oxygen saturation . 97

Figure 5.1: Schematic of the values needed to compute the nonlinear correction in m/z 33 and m/z 34 111
Figure 5.2: Effects of filtering $\delta^{17}O$ measured from a cylinder of gas 113
Figure 5.3: $\delta^{17}O$ versus $\delta^{18}O$ from the equilibrator data 116
Figure 5.4: Timeseries of $^{17}\Delta$ measurements at the Scripps Institution of Oceanography pier 117
Figure 5.5: Mean diurnal cycle in $^{17}\Delta$ 117
Figure 5.6: Data and model results of biological O_2, $\delta^{18}O$, and $^{17}\Delta$ diurnal cycles 119

Figure 6.1: Atmospheric CO_2 record based on ice core data before 1958, and yearly averages of direct observations from Mauna Loa and the South Pole after 1958 130
Figure 6.2: Fossil fuel emissions per year 132
Figure 6.3: Terrestrial two-box model 137
Figure 6.4: Residual land carbon fluxes based on a deconvolution and based on the temperature-independent model 140
Figure 6.5: Atmospheric CO_2 record, atmospheric CO_2 modeled using the temperature-independent model, and a curve depicting 57% of cumulative industrial emissions 142
Figure 6.6: Residual land carbon fluxes based on a deconvolution and based on the temperature-dependent model 144
Figure 6.7: Atmospheric CO_2 record, atmospheric CO_2 modeled using the temperature-dependent model, and a curve depicting 57% of cumulative industrial emissions 145
Figure 6.8: The integrated difference between the residual land flux and temperature-independent model results 148
Figure 6.9: The integrated difference between the residual land flux and temperature-dependent model results 150
Figure 6.10: Unfiltered residual land flux, showing variability on short (e.g. El Niño) time scales 152
Figure 6.11: Constant airborne fraction anomaly of the atmospheric record and model results, with the ice core record shifted down 2 ppm 153

LIST OF TABLES

Table 2.1: Examples of corrections needed to account for incomplete equilibration 46

Table 3.1: Interference in $\delta(33/32)$ and $\delta(34/32)$ from N_2 and CO_2 60

Table 4.1: Best-fit parameters for the O_2 and $\delta^{18}O$ diurnal cycle model . . 90
Table 4.2: Estimates of production rates using chlorophyll concentration, the diurnal cycle model, and the amplitude of the observed oxygen cycle 99

Table 5.1: Constants used to model $\delta^{18}O$ and $\delta^{17}O$ 115
Table 5.2: Mean measured $^{17}\Delta$ 118
Table 5.3: Best-fit parameters for the $^{17}\Delta$ model 119
Table 5.4: Gross and net production in the mixed layer 122

Table 6.1: Parameters used for calculations of the residual land flux 139
Table 6.2: CO_2 box model parameters 139
Table 6.3: CO_2 model best-fit parameters, and land temperature feedback . 147

ACKNOWLEDGEMENTS

This thesis would not have been possible without the help of many people. I would first like to thank my advisor, Ralph Keeling, for all of his help, encouragement, and guidance. He has helped me become a better researcher and a better scientific writer. I would also like to thank my committee members, Lihini Aluwihare, Ralf Goericke, Jeffrey Severinghaus, Mark Thiemens, and Ray Weiss, for their help over the years.

I feel lucky to have joined a lab with knowledgable people who taught me a lot about working with mass spectrometers. I am thankful for years of their support and friendship. I thank Bill Paplawsky for teaching me a lot about working with instruments in the lab, for brainstorming with me about instrumentation ideas, and for helping make sure that having a mass spectrometer in the same room as a lot of salt water did not turn into a disaster. I thank Adam Cox for always being willing to help with my project, and Kim Spalding for her support. I would also like to thank Steve Piper, Lisa Welp, Heather Graven, Jonathan Bent, Yann Bozec, Roberta Hamme, and Angeline Ta for many helpful discussions over the years.

I am also grateful to the larger Scripps community. I thank Todd Martz and Yui Takeshita for their generous loan of an optode, which was crucial for validating my data. There have been many people at Scripps who have given valuable feedback over the years, including John McGowan, Drew Lucas, and Christina Frieder. I also thank my undergraduate research advisors at Princeton, Edward Stiefel and François Morel, who first introduced me to oceanographic research, and helped me get to Scripps in the first place.

I would like to thank the friends I have made here at Scripps, who have ensured that the past several years have been a lot of fun. I thank Anaïs Orsi for being such a wonderful officemate, and for making sure we never ran out of chocolate. I would also like to thank Dian Putrasahan, Stephanie Fried, Robert Todd, Sylvia Cole, Danny Richter, Taylor Stratton, Yvonne Firing, Ben Reineman, Peter Sutherland, Marcel Croon, Rose Anderson, Laura Brooks, Chad and Carrie Kishimoto, and Wendell Misch, for many wonderful memories.

Finally, this thesis would not have been possible without the support of my family. I thank my parents, Debbie and Bruce, for a lifetime of encouraging my curiosity and for always believing that I could achieve my dreams. I also thank my brother, Scott, for always being so supportive and for being a great friend. I thank my family-in-law, Jan, Vicky, and Susanne, for their support. Last, but not least, I thank my husband and best friend, Marc. I am grateful for his unwavering optimism, for helping me keep perspective, and for supporting me during every step of this process.

Chapter 2, in full, is a reprint of material previously submitted as "An equilibrator to measure dissolved oxygen and its isotopes," by Lauren Elmegreen Rafelski, Bill Paplawsky, and Ralph F. Keeling, to the *Journal of Atmospheric and Oceanic Technology*, 2012. I was the primary investigator and author of this paper.

Chapter 3, in part, is being prepared for publication. Lauren Elmegreen Rafelski, Bill Paplawsky, and Ralph F. Keeling. I am the primary investigator and author of this paper.

Chapter 4, in part, is being prepared for publication. Lauren Elmegreen Rafelski, Bill Paplawsky, and Ralph F. Keeling. I am the primary investigator and author of this paper.

Chapter 5, in part, is being prepared for publication. Lauren Elmegreen Rafelski, Bill Paplawsky, and Ralph F. Keeling. I am the primary investigator and author of this paper.

Chapter 6, in full, is a reprint of material previously published as "Climate effects on atmospheric carbon dioxide over the last century," by Lauren Elmegreen Rafelski, Stephen C. Piper, and Ralph F. Keeling, in *Tellus*, 2009, Vol, 61B, pp. 718-731. I was the primary investigator and author of this paper.

This work was supported in part by a National Science Foundation Graduate Research Fellowship and by an Achievement Rewards for College Scientists (ARCS), Los Angeles Chapter, scholarship.

VITA

2005	A. B. in Chemistry, *magna cum laude* Princeton University
2006	M. S. in Oceanography Scripps Institution of Oceanography University of California, San Diego
2006-2009	NSF Graduate Research Fellowship
2010	Achievement Rewards for College Scientists (ARCS), Los Angeles Chapter, scholarship
2012	Ph. D. in Oceanography Scripps Institution of Oceanography University of California, San Diego

PUBLICATIONS

Rafelski, L. E., B. Paplawsky, and R. F. Keeling. 2012. An equilibrator to measure dissolved oxygen and its isotopes. Submitted to the Journal of Atmospheric and Oceanic Technology.

Rafelski, L. E., S. C. Piper, and R. F. Keeling. 2009. Climate effects on atmospheric carbon dioxide over the last century. Tellus 61B: 718-731.

Castruita, M., Y. Shaked, **L. A. Elmegreen**, E. I. Stiefel, and F. M. M. Morel. 2008. Availability of iron from iron-storage proteins to marine phytoplankton. Limnology and Oceanography 53: 890-899.

Castruita, M., **L. A. Elmegreen**, Y. Shaked, E. I. Stiefel, and F. M. M. Morel. 2007. Comparison of the kinetics of iron release from a marine (*Trichodesmium erythraeum*) Dps protein and mammalian ferritin in the presence and absence of ligands. Journal of Inorganic Biochemistry 101: 1686-1691.

Castruita, M., M. Saito, P. C. Schottel, **L. A. Elmegreen**, S. Myneni, E. I. Stiefel, and F. M. M. Morel. 2006. Overexpression and characterization of an iron storage and DNA-binding Dps protein from *Trichodesmium erythraeum*. Applied and Environmental Microbiology 72: 2918-2924.

ABSTRACT OF THE DISSERTATION

Continuous surface ocean measurements of dissolved oxygen isotopes

by

Lauren Elmegreen Rafelski

Doctor of Philosophy in Oceanography

University of California, San Diego, 2012

Professor Ralph Keeling, Chair

Continuous measurements of dissolved oxygen isotopes can provide insight into how oceanic primary production varies over time and space. For example, $^{17}\Delta$, the deviation from the expected mass-dependent isotopic fractionation, is a tracer of gross primary production. This thesis focuses on techniques for continuously measuring dissolved oxygen isotopes, and showcases measurements from the Scripps Institution of Oceanography pier. We developed a counterflow-type equilibrator with a time constant of 7-8 minutes for oxygen. When interfaced to a mass spectrometer, this equilibrator allows for a sampling flow rate of 3 mL min^{-1}. Using a model of O_2, N_2, and Ar, the behavior of major gases in an equilibrator is explored, and the corrections needed to account for incomplete equilibration are determined. We also quantify possible sources of interference to the measurement

of oxygen isotopes, and find that CO_2 and N_2 contribute to the interference, while the interferences from water vapor and DMS are negligible. In addition, we describe a technique for keeping the O_2/N_2 ratio constant, to reduce the interference from N_2.

Dissolved oxygen isotopes were measured near the surface ocean at the Scripps Institution of Oceanography pier for five weeks. The data show diurnal cycles in O_2 and $\delta^{18}O$, with amplitudes of 19 mmol m^{-3} and 1.1 per mil, respectively. The diurnal cycles are well described by a box model that includes photosynthesis, respiration, air-sea gas exchange, and mixing. The timing of the cycle can be explained using a photosynthesis rate proportional to photosynthetically active radiation. The maximum daily photosynthesis rate is 4.7 mmol O_2 m^{-3} hr^{-1} (40.3 mgC m^{-3} hr^{-1} using a photosynthetic quotient of 1.4). This is in agreement with the production estimated from the chlorophyll concentration. Although the $^{17}\Delta$ data did not have a resolvable diurnal cycle, modeled $^{17}\Delta$ shows a diurnal cycle with an amplitude of 11 per meg. The oxygen isotope data also show variability over longer timescales, suggesting a change in the production rate over time. In the future, these techniques could be used around the world to improve our understanding of variability in oceanic primary production.

Chapter 1

Introduction

1.1 The carbon cycle

Human activities have caused an increase in atmospheric CO_2 concentration, which has been measured at Mauna Loa since 1958, and is currently measured at several stations around the world (e.g. Keeling et al., 2005). In 2009, fossil fuel burning and cement manufacturing emitted 8.4 $\pm$ 0.5 Pg C into the atmosphere (Friedlingstein et al., 2010). However, only around half of these emissions remain in the atmosphere (Keeling et al., 1995). Understanding the processes that remove CO_2 from the atmosphere, and how these processes change over time, is essential for predicting how future CO_2 emissions could impact climate.

Without human influences, the carbon cycle averaged over several years would be approximately in balance, with fluxes of CO_2 to the atmosphere nearly equal to fluxes of CO_2 from the atmosphere (Denman et al., 2007). CO_2 is added to the atmosphere from respiration, biomass burning, and volcanism, and removed via photosynthesis and weathering. In addition, CO_2 is exchanged between the surface ocean and atmosphere. In the ocean, some CO_2 is converted to organic carbon through photosynthesis, and some of this organic carbon sinks to the deeper ocean (the biological pump), where a small fraction of the carbon is buried in sediments. Also, dissolved CO_2 can be brought to the deeper ocean through sinking of cold water masses (the solubility pump).

Human activities have altered the natural carbon cycle. Fossil fuel emissions

and land use change (e.g. deforestation and biomass burning) add CO_2 to the atmosphere. These additional sources of CO_2 are in part offset by increased uptake of CO_2 by the terrestrial biosphere and the ocean, such that only around half of the anthropogenic CO_2 remains in the atmosphere.

This thesis focuses primarily on techniques for measuring the biological carbon uptake in the ocean (i.e. primary production) using continuous measurements of dissolved oxygen isotopes. Primary production has a role in how much carbon will be transported to the deeper ocean. Also, photosynthetically fixed carbon forms the base of the oceanic food chain. Therefore, it is important to have good measurements of the carbon fluxes due to marine biota. Continuous measurements could increase our understanding of the variability in production and carbon export over time and space.

1.2 Methods of measuring primary production

One way to measure primary production is using incubations of bottle samples. Once a sample of water has been collected, production in the sample can be measured in a few different ways. For example, ^{14}C bicarbonate can be added to the sample. This bicarbonate gets assimilated into organic carbon through photosynthesis, and the carbon uptake is measured by filtering out the particulate organic carbon and measuring its radioactivity (e.g. Peterson, 1980). This technique measures a value of production that lies somewhere between gross primary production (GPP: the total amount of photosynthesis) and net community production (NCP: GPP minus autotrophic and heterotrophic respiration) (Bender et al., 1999). Another method is add $H_2^{18}O$ to the sample, and measure the change in ^{18}O of dissolved oxygen, which is produced during photosynthesis (Bender et al., 1987). This technique measures GPP. Finally, growth can be measured by incubating the bottle in the light or dark, and measuring the change in dissolved O_2 or CO_2. The dark incubations give a measure of community respiration, and the light incubations give a measure of NCP (Bender et al., 1987).

There are some drawbacks to measuring production using bottle incuba-

tions. Production has been shown to be highly variable over time (Karl et al., 2003). Bottle incubations may miss this variability because they only measure production in discrete times and places, and therefore an average estimate of production based on the bottle incubations may overestimate or underestimate the true average production. Furthermore, bottle incubations may not replicate the ecosystem of the ocean. For example, there may be differences in temperature or irradiance that affect the growth of the organisms (e.g. Marra et al., 1988; Marra, 2002). For these reasons, efforts have been made to measure production using techniques that do not involve incubations.

Alternatively, global primary production can be estimated using ocean color satellites, such as CZCS (Coastal Zone Color Scanner) and SeaWiFS (Sea-viewing Wide Field-of-view Sensor). Ocean color can be used to determine chlorophyll concentration, which is a proxy for production (e.g. Antoine et al., 1996; Westberry et al., 2008). Although these satellites provide very high spatial coverage, there are a few problems with using satellite measurements. For example, the relationship between color and chlorophyll may vary regionally, such that global algorithms converting color to chlorophyll content are not as accurate for regional estimates of production (O'Reilly et al., 1998). In addition, satellite-based production measurements are calibrated using bottle incubations, so any drawbacks of using bottle incubations (with the exception of temporal and spatial coverage) also apply to satellite measurements. Finally, satellite measurements are ineffective during periods of cloud cover, which is especially problematic at high latitudes and during the winter at mid-latitudes. The limitations of bottle incubation and satellite methods of measuring production have led to the development of in-situ techniques for measuring production, such as using dissolved O_2 and its isotopes. In addition, extreme spatial heterogeneity ("patchiness") has made continuous shipboard measurements increasingly useful.

1.3 The use of oxygen isotopes to measure production

Measurements of dissolved oxygen in the ocean can be used to quantify aspects of the carbon cycle, because many processes that affect CO_2 affect O_2 as well. For example, photosynthesis uses CO_2 and produces O_2, and respiration produces CO_2 and uses O_2. In the ocean, measurements of dissolved O_2 (e.g. Emerson et al., 2008) or O_2/Ar (e.g. Kaiser et al., 2005; Quay et al., 2012) have been used to determine NCP. Also, GPP has recently been measured using continuous measurements of dissolved O_2/Ar (Hamme et al., 2012).

In addition to measuring production using O_2 concentration, production can be measured by looking at changes in the isotopic composition of dissolved O_2. Oxygen has three major isotopes, at mass 16 (99.76%), mass 17 (0.04%), and mass 18 (0.2%). Since oxygen 16 is so much more abundant than the other isotopes, the most common form of O_2 gas is the isotopologue $^{16}O^{16}O$ (mass 32), followed by $^{16}O^{18}O$ (mass 34) and $^{16}O^{17}O$ (mass 33). The isotopic composition of dissolved oxygen is affected by photosynthesis, respiration, and air-sea gas exchange.

The isotopic composition of oxygen can be expressed using δ notation:

$$\delta^x O = \frac{(^xO/^{16}O)_s}{(^xO/^{16}O)_r} - 1 \tag{1.1}$$

where x is 17 or 18, s is the sample composition, and r is the reference composition. δ^xO is multiplied by 10^3 to give units of per mil, or 10^6 to get units of per meg.

Simultaneous measurements of oxygen concentration and δ^{18}O can be used to determine production. Respiration increases δ^{18}O, because ^{16}O is used preferentially over ^{18}O, a process known as fractionation (Lane and Dole, 1956). Photosynthesis decreases δ^{18}O because photosynthesis produces oxygen with a composition similar to the isotopic composition of oxygen in H_2O, which has proportionally more ^{16}O than air (Kroopnick and Craig, 1972; Guy et al., 1993). Air-sea gas exchange will bring dissolved O_2 and δ^{18}O towards atmospheric values. Models that include these processes have been used with dissolved gas measurements to determine various measures of production, such as GPP and the ratio of photosyn-

thesis to respiration (Bender and Grande, 1987; Quay et al., 1993; Venkiteswaran et al., 2007; Quiñones-Rivera et al., 2007, 2009).

In recent years, GPP has also been measured using simultaneous measurements of all three oxygen isotopes (i.e. the triple isotopic composition). Photochemical ozone reactions in the stratosphere influence the isotopic composition of O_2 in the troposphere (Luz et al., 1999). Experiments and observations have shown that the oxygen isotopes of stratospheric CO_2 reflect mass-independent fractionation, with a nearly 1:1 relationship between δ^{18}O and δ^{17}O (Thiemens et al., 1995). By comparison, fractionation that is mass-dependent (such as respiration) would result in a δ^{17}O that is about half of δ^{18}O. The photolysis of ozone creates an excited oxygen atom, which can exchange with the oxygen in CO_2. During this exchange, CO_2 ends up becoming enriched in heavier oxygen isotopes (i.e. ^{17}O and ^{18}O). Because molecular oxygen is involved in ozone formation, O_2 becomes mass-independently depleted in heavier oxygen isotopes as a result (Luz et al., 1999).

The triple isotopic composition of O_2 is represented using:

$$\Delta^{17}O = \delta^{17}O - \lambda\delta^{18}O \tag{1.2}$$

where λ is the relationship between δ^{17}O and δ^{18}O for mass-dependent fractionation, and is close to 0.52 (Luz and Barkan, 2000). This is an approximation of:

$$^{17}\Delta = ln\left(\frac{^{17}R}{^{17}R_{ref}}\right) - \lambda ln\left(\frac{^{18}R}{^{18}R_{ref}}\right) \tag{1.3}$$

where ^{17}R or ^{18}R is the ratio of the oxygen isotope to $^{16}O_2$ (e.g. $^{17}O^{16}O/^{16}O_2$) and R_{ref} is the reference ratio (Angert et al., 2003).

In the ocean, the two sources of O_2 are air-sea gas exchange and photosynthesis. Typically, the atmospheric value of Δ^{17}O is used as the reference, so air-sea gas exchange will bring dissolved Δ^{17}O close to zero (plus a temperature-dependent offset from fractionation during dissolution, Luz and Barkan, 2009). Photosynthesis will increase Δ^{17}O, because the oxygen atoms in water have not been affected by the stratospheric fractionation processes. Respiration has no effect on Δ^{17}O, because it is a mass-dependent fractionation process. Because the two sources of

dissolved O_2 in the ocean have different values of $\Delta^{17}O$, this measurement can be used to determine the ratio of O_2 originating from photosynthesis, to O_2 from the atmosphere (Hendricks et al., 2004). By using wind speed parameterizations to estimate the air-sea gas exchange, the gross production can then be obtained. Importantly, the O_2 equilibration time of the ocean mixed layer is a few weeks, so this tracer integrates episodic blooms over this timescale, which could be missed by bottle sampling.

The $\Delta^{17}O$ technique has been used in the Southern Ocean (Hendricks et al., 2004; Reuer et al., 2007; Hamme et al., 2012), the equatorial and tropical Pacific (Hendricks et al., 2005; Juranek and Quay, 2010; Stanley et al., 2010), the subtropical Pacific (Juranek and Quay, 2005; Quay et al., 2010), and the north Atlantic (Luz and Barkan, 2009; Quay et al., 2012), as well as coastal areas near Israel and Japan (Luz and Barkan, 2009; Sarma et al., 2005, 2008). Variations in $\Delta^{17}O$ and the corresponding calculations of GPP have been observed on seasonal and daily timescales (Sarma et al., 2005; Juranek and Quay, 2005; Luz and Barkan, 2009; Quay et al., 2010, 2012). In particular, the coastal regions show strong variability in $\Delta^{17}O$ on daily timescales. In addition, recent work determining NCP using continuous measurements of O_2 and Ar showed that NCP can be highly spatially variable. In order for production measurements to be meaningfully extrapolated over time or space, the variability must be understood. These observations suggest that more frequent measurements of dissolved oxygen isotopes could increase our understanding of the variability in production.

1.4 Overview of this thesis

Previous studies using $\delta^{18}O$ and $\Delta^{17}O$ to measure production have used discrete samples of water, from which the gases are later extracted and measured on a mass spectrometer. This limits the timescales of changes that can be measured. Although dissolved oxygen concentration has been measured continuously using optical or electrochemical sensors (e.g. McNeil and Farmer, 1995; DeGrandpre et al., 1998; Emerson et al., 2002) or mass spectrometers (e.g. Tortell, 2005;

Kaiser et al., 2005; Cassar et al., 2009), no one has previously taken continuous measurements of dissolved oxygen isotopes. Continuous measurements of dissolved oxygen isotopes would give information about changes in production over time and space.

The aim of this thesis is to continuously measure dissolved oxygen isotopes. We originally attempted to measure dissolved oxygen isotopes using a "Weiss equilibrator" - a showerhead equilibrator designed to measure CO_2 (Johnson, 1999). We measured dissolved isotopes at sea on the R/V New Horizon using this equilibrator. Although the mass spectrometer performed well at sea, we subsequently found that, because of the slow equilibration of O_2, this equilibrator caused errors in dissolved oxygen isotope measurements that were too high to be corrected. This prompted the development of an equilibrator with a much smaller headspace volume that could be used to equilibrate dissolved oxygen. This equilibrator is described in Chapter 2. This chapter also describes a model that can be used to understand the behavior of major gases (O_2, N_2, and Ar) in an equilibrator.

Continuously measuring dissolved oxygen isotopes on a mass spectrometer has the additional challenge that oxygen isotopes are relatively rare, and therefore highly susceptible to interferences. For traditional techniques using bottle samples, O_2 and Ar are typically isolated from other gases before measurement on a mass spectrometer. However, this is impractical with continuous measurements. Because the biggest source of interference is N_2, we used a method of stabilizing the O_2/N_2 ratio, rather than removing N_2. Chapter 3 discusses this method, and describes and quantifies various sources of interference on oxygen isotopes, and methods to correct for these interferences.

Chapter 4 highlights measurements of $\delta^{18}O$ near the surface of the ocean at the Scripps Institution of Oceanography (SIO) pier. The equilibrator and mass spectrometer methods described in Chapters 2 and 3 were used at the SIO pier to collect data over five weeks. This chapter explores the variability in O_2 and $\delta^{18}O$, on timescales from one day to a few weeks. Using these data, along with a box model that includes photosynthesis, respiration, air-sea gas exchange, and mixing, it is possible to estimate gross photosynthesis rates, and to understand the

observed variability in $\delta^{18}O$.

Chapter 5 discusses measurements of $\Delta^{17}O$ at the Scripps Institution of Oceanography pier. It describes further corrections that must be made to the $\Delta^{17}O$ measurements. Although the $\Delta^{17}O$ measurements were much noisier than the $\delta^{18}O$ measurements, we can determine the mean value of $\Delta^{17}O$. The model presented in Chapter 4 is modified to include $\Delta^{17}O$. Results from this model show the expected diurnal variability in $\Delta^{17}O$.

Although most of this thesis focuses on measuring dissolved oxygen isotopes in the ocean, Chapter 6 investigates another important aspect of the carbon cycle: carbon exchange between the atmosphere and the terrestrial biosphere. We explore the variability in the atmospheric CO_2 record over the 20th century. We show that temperature variations, which affect the land carbon uptake, can account for some of the observed multidecadal variability. We also show that there is a connection between variability on multidecadal and El Niño timescales.

References

Angert, A., Rachmilevitch, S., Barkan, E., and Luz, B., 2003: Effects of photorespiration, the cytochrome pathway, and the alternative pathway on the triple isotopic composition of atmospheric O_2. *Global Biogeochemical Cycles*, **17**(1), 1030, doi:10.1029/2002GB001933.

Antoine, D., Andre, J.-M., and Morel, A., 1996: Oceanic primary production 2. Estimation at global scale from satellite (coastal zone color scanner) chlorophyll. *Global Biogeochemical Cycles*, **10**(1), 57–69.

Bender, M., Grande, K., Johnson, K., Marra, J., Williams, P. J. B., Sieburth, J., Pilson, M., Langdon, C., Hitchcock, G., Orchardo, J., Hunt, C., Donaghay, P., and Heinemann, K., 1987: A comparison of four methods for determining planktonic community production. *Limnology and Oceanography*, **32**(5), 1085–1098.

Bender, M., Orchardo, J., Dickson, M.-L., Barber, R., and Lindley, S., 1999: In vitro O_2 fluxes compared with ^{14}C production and other rate terms during the JGOFS Equatorial Pacific experiment. *Deep Sea Research I*, **46**, 637–654.

Bender, M. L., and Grande, K. D., 1987: Production, respiration, and the isotope geochemistry of O_2 in the upper water column. *Global Biogeochemical Cycles*, **1**(1), 49–59.

Cassar, N., Barnett, B. A., Bender, M. L., Kaiser, J., Hamme, R. C., and Tilbrook, B., 2009: Continuous high-frequency dissolved O_2/Ar measurements by equilibrator inlet mass spectrometry. *Analytical Chemistry*, **81**, 1855–1861.

DeGrandpre, M. D., Hammar, T. R., and Wirick, C. D., 1998: Short-term pCO_2 and O_2 dynamics in California coastal waters. *Deep-Sea Research II*, **45**, 1557–1575.

Denman, K. L., Brasseur, G., Chidthaisong, A., Ciais, P., Cox, P. M., Dickinson, R. E., Hauglustaine, D., Heinze, C., Holland, E., Jacob, D., Lohmann, U., Ramachandran, S., da Silva Dias, P. L., Wofsy, S. C., and Zhang, X., 2007:

Couplings between changes in the climate system and biogeochemistry. In *Climate change 2007: The physical science basis. Contribution of Working Group I to the Fourth Assessment Report of the Intergovernmental Panel on Climate Change*, editors S. Solomon, D. Qin, M. Manning, Z. Chen, M. Marquis, K. B. Averyt, M. Tignor, and H. L. Miller. Cambridge University Press, Cambridge, United Kingdom and New York, NY, USA.

Emerson, S., Stump, C., Johnson, B., and Karl, D. M., 2002: In situ determination of oxygen and nitrogen dynamics in the upper ocean. *Deep-Sea Research I*, **49**, 941–952.

Emerson, S., Stump, C., and Nicholson, D., 2008: Net biological oxygen production in the ocean: Remote in situ measurements of O_2 and N_2 in surface waters. *Global Biogeochemical Cycles*, **22**(GB3023), doi:10.1029/2007GB003095.

Friedlingstein, P., Houghton, R. A., Marland, G., Hackler, J., Boden, T. A., Conway, T. J., Canadell, J. G., Raupach, M. R., Ciais, P., and Le Quéré, C., 2010: Update on CO_2 emissions. *Nature Geoscience*, **3**, 811–812.

Guy, R. D., Fogel, M. L., and Berry, J. A., 1993: Photosynthetic fractionation of the stable isotopes of oxygen and carbon. *Plant Physiology*, **101**, 37–47.

Hamme, R. C., Cassar, N., Lance, V. P., Vaillancourt, R. D., Bender, M. L., Strutton, P. G., Moore, T. S., DeGrandpre, M. D., Sabine, C. L., Ho, D. T., and Hargreaves, B. R., 2012: Dissolved O_2/Ar and other methods reveal rapid changes in productivity during a Lagrangian experiment in the Southern Ocean. *Journal of Geophysical Research*, **117**(C00F12), doi:10.1029/2011JC007046.

Hendricks, M. B., Bender, M. L., and Barnett, B. A., 2004: Net and gross O_2 production in the Southern Ocean from measurements of biological O_2 saturation and its triple isotope composition. *Deep-Sea Research I*, **51**, 1541–1561.

Hendricks, M. B., Bender, M. L., Barnett, B. A., Strutton, P., and Chavez, F. P., 2005: Triple oxygen isotope composition of dissolved O_2 in the equatorial Pacific: A tracer of mixing, production, and respiration. *Journal of Geophysical Research*, **110**(C12021), doi:10.1029/2004JC002735.

Johnson, J. E., 1999: Evaluation of a seawater equilibrator for shipboard analysis of dissolved oceanic trace gases. *Analytica Chimica Acta*, **395**, 119–132.

Juranek, L. W., and Quay, P. D., 2005: In vitro and in situ gross primary and net community production in the North Pacific Subtropical Gyre using labeled and natural abundance isotopes of dissolved O_2. *Global Biogeochemical Cycles*, **19**(GB3009), doi:10.1029/2004GB002384.

Juranek, L. W., and Quay, P. D., 2010: Basin-wide photosynthetic production rates in the subtropical and tropical pacific ocean determined from dissolved oxygen isotope ratio measurements. *Global Biogeochemical Cycles*, **24**(GB2006), doi:10.1029/2009GB003492.

Kaiser, J., Reuer, M. K., Barnett, B., and Bender, M. L., 2005: Marine productivity estimates from continuous O_2/Ar ratio measurements by membrane inlet mass spectrometry. *Geophysical Research Letters*, **32**(L19605), doi:10.1029/2005GL023459.

Karl, D. M., Laws, E. A., Morris, P., Williams, P. J. B., and Emerson, S., 2003: Metabolic balance of the open sea. *Nature*, **426**, 32.

Keeling, C. D., Piper, S. C., Bacastow, R. B., Wahlen, M., Whorf, T. P., Heimann, M., and Meijer, H. A., 2005: Atmospheric CO_2 and $^{13}CO_2$ exchange with the terrestrial biosphere and oceans from 1978 to 2000: Observations and carbon cycle implications. In *A History of Atmospheric CO_2 and its effects on Plants, Animals, and Ecosystems*, editors J. R. Ehleringer, T. E. Cerling, and M. D. Dearing, 83–113. Springer Verlag, New York.

Keeling, C. D., Whorf, T. P., Wahlen, M., and van der Plicht, J., 1995: Interannual extremes in the rate of rise of atmospheric carbon dioxide since 1980. *Nature*, **375**, 666–670.

Kroopnick, P., and Craig, H., 1972: Atmospheric oxygen: Isotopic composition and solubility fractionation. *Science*, **175**(4017), 54–55.

Lane, G. A., and Dole, M., 1956: Fractionation of oxygen isotopes during respiration. *Science*, **123**(3197), 574–576.

Luz, B., and Barkan, E., 2000: Assessment of oceanic productivity with the triple-isotope composition of dissolved oxygen. *Science*, **288**, 2028–2031.

Luz, B., and Barkan, E., 2009: Net and gross oxygen production from O_2/Ar, $^{17}O/^{16}O$ and $^{18}O/^{16}O$ ratios. *Aquatic Microbial Ecology*, **56**, 133–145.

Luz, B., Barkan, E., Bender, M. L., Thiemens, M. H., and Boering, K. A., 1999: Triple-isotope composition of atmospheric oxygen as a tracer of biosphere productivity. *Nature*, **400**, 547–550.

Marra, J., 2002: Approaches to the measurement of plankton production. In *Phytoplankton Productivity: Carbon Assimilation in Marine and Freshwater Ecosystems*, editors P. J. B. Williams, D. N. Thomas, and C. S. Reynolds, 78–108. Blackwell, Malden, MA.

Marra, J., Haas, L. W., and Heinemann, K. R., 1988: Time course of C assimilation and microbial food web. *Journal of Experimental Marine Biology and Ecology*, **115**, 263–280.

McNeil, C. L., and Farmer, D. M., 1995: Observations of the influence of diurnal convection on upper ocean dissolved gas measurements. *Journal of Marine Research*, **53**, 151–169.

O'Reilly, J. E., Maritorena, S., Mitchell, B. G., Siegel, D. A., Carder, K. L., Garver, S. A., Kahru, M., and McClain, C., 1998: Ocean color chlorophyll algorithms for SeaWiFS. *Journal of Geophysical Research*, **103**(C11), 24937–24953.

Peterson, B. J., 1980: Aquatic primary productivity and the ^{14}C-CO_2 method: A history of the productivity problem. *Annual Review of Ecology and Systematics*, **11**, 359–385.

Quay, P., Stutsman, J., and Steinhoff, T., 2012: Primary production and carbon export rates across the subpolar N. Atlantic Ocean basin based on triple oxygen isotope and dissolved O_2 and Ar gas measurements. *Global Biogeochemical Cycles*, **26**(GB2003), doi:10.1029/2010GB004003.

Quay, P. D., Emerson, S., Wilbur, D. O., and Stump, C., 1993: The δ^{18}O of dissolved O_2 in the surface waters of the Subarctic Pacific: A tracer of biological productivity. *Journal of Geophysical Research*, **98**(C5), 8447–8458.

Quay, P. D., Peacock, C., Björkman, K., and Karl, D. M., 2010: Measuring primary production rates in the ocean: Enigmatic results between incubation and non-incubation methods at station ALOHA. *Global Biogeochemical Cycles*, **24**(GB3014), doi:10.1029/2009GB003665.

Quiñones-Rivera, Z. J., Wissel, B., and Justić, D., 2009: Development of productivity models for the northern Gulf of Mexico based on oxygen concentrations and stable isotopes. *Estuaries and Coasts*, **32**, 436–446.

Quiñones-Rivera, Z. J., Wissel, B., Justić, D., and Fry, B., 2007: Partitioning oxygen sources and sinks in a stratified, eutrophic coastal ecosystem using stable oxygen isotopes. *Marine Ecology Progress Series*, **342**, 69–83.

Reuer, M. K., Barnett, B. A., Bender, M. L., Falkowski, P. G., and Hendricks, M. B., 2007: New estimates of Southern Ocean biological production rates from O_2/Ar ratios and the triple isotope composition of O_2. *Deep-Sea Research I*, **54**, 951–974.

Sarma, V. V. S. S., Abe, O., Hashimoto, S., Hinuma, A., and Saino, T., 2005: Seasonal variations in triple oxygen isotopes and gross oxygen production in the Sagami Bay, central Japan. *Limnology and Oceanography*, **50**(2), 544–552.

Sarma, V. V. S. S., Abe, O., and Saino, T., 2008: Spatial variations in time-integrated plankton metabolic rates in Sagami Bay using triple oxygen isotopes and O_2:Ar ratios. *Limnology and Oceanography*, **53**(5), 1776–1783.

Stanley, R. H. R., Kirkpatrick, J. B., Cassar, N., Barnett, B. A., and Bender, M. L., 2010: Net community production and gross primary production rates in the western equatorial Pacific. *Global Biogeochemical Cycles*, **24**(GB4001), doi:10.1029/2009GB003651.

Thiemens, M. H., Jackson, T., Zipf, E. C., Erdman, P. W., and van Egmond, C., 1995: Carbon dioxide and oxygen isotope anomalies in the mesosphere and stratosphere. *Science*, **270**(5238), 969–972.

Tortell, P. D., 2005: Dissolved gas measurements in oceanic waters made by membrane inlet mass spectrometry. *Limnology and Oceanography: Methods*, **3**, 24–37.

Venkiteswaran, J. J., Wassenaar, L. I., and Schiff, S. L., 2007: Dynamics of dissolved oxygen isotopic ratios: A transient model to quantify primary production, community respiration, and air-water exchange in aquatic ecosystems. *Oecologia*, **153**, 385–398.

Westberry, T., Behrenfeld, M. J., Siegel, D. A., and Boss, E., 2008: Carbon-based primary productivity modeling with vertically resolved photoacclimation. *Global Biogeochemical Cycles*, **22**(GB2024), doi:10.1029/2007GB003078.

Chapter 2

An equilibrator to measure dissolved oxygen and its isotopes

2.1 Introduction

Measurements of dissolved gases in the ocean can give information about air-sea gas exchange, oceanic carbon uptake, and other biological and physical processes. Because biological oxygen production and consumption are closely tied to carbon consumption and production, measurements of processes affecting oxygen can be used to determine gross and net biological carbon uptake in the ocean.

Dissolved oxygen isotopes can be used together with dissolved oxygen concentration to determine relative rates of gross and net primary production. δ^{18}O, defined as:

$$\delta^{18}O = \frac{(^{18}O/^{16}O)_{sample}}{(^{18}O/^{16}O)_{reference}} - 1 \tag{2.1}$$

has been used with oxygen measurements as a tracer of water masses (Bender, 1990; Levine et al., 2009), as well as a measure of the ratio of gross to net primary production (Bender and Grande, 1987; Quiñones-Rivera et al., 2007). These computations rely on the fact that oxygen produced during photosynthesis is isotopically lighter than oxygen in air (i.e. less ^{18}O) and respiration preferentially consumes lighter oxygen isotopes. For example, oxygen in air has a δ^{18}O of 23.88

per mil (Barkan and Luz, 2005) on the SMOW scale, whereas photosynthetic oxygen has a δ^{18}O close to zero. However, these calculations are sensitive to uncertainties in the fractionation factor of respiration (Bender and Grande, 1987; Quay et al., 1993).

The triple isotopic composition of dissolved O_2 (isotopes 16, 17 and 18) can be used to measure gross primary production without making assumptions about the respiration fractionation factor (Luz and Barkan, 2000). Using the triple isotopic composition of oxygen to measure gross primary production is possible because in the stratosphere, photochemical reactions related to ozone production cause mass-independent fractionation of oxygen isotopes, with the heavier ^{17}O and ^{18}O preferentially ending up in CO_2 (Thiemens et al., 1995). This is in contrast to fractionation processes such as respiration, where the degree of fractionation is roughly proportional to the mass difference between the major isotope and the minor isotope ("mass-dependent fractionation"). The mass-independent fractionation of oxygen in the stratosphere causes an excess in ^{17}O relative to ^{18}O, defined as:

$$\Delta^{17}O = \delta^{17}O - \lambda\delta^{18}O \tag{2.2}$$

where λ is the relationship between δ^{17}O and δ^{18}O due to mass-dependent fractionation (approximately 0.52, Luz and Barkan, 2000). Equation 2.2 is an approximation of:

$$^{17}\Delta = ln\left(\frac{^{17}R}{^{17}R_{ref}}\right) - \lambda ln\left(\frac{^{18}R}{^{18}R_{ref}}\right) \tag{2.3}$$

where ^{17}R or ^{18}R is the ratio of the oxygen isotope to $^{16}O_2$ (e.g. $^{17}O^{16}O/^{16}O_2$) and R_{ref} is the reference ratio (Angert et al., 2003).

Because of the mass-independent fractionation of O_2 in the stratosphere, O_2 in the atmosphere has a different Δ^{17}O than O_2 produced by photosynthesis. For example, photosynthetic O_2 has a typical Δ^{17}O of 249 per meg relative to atmospheric O_2 (Luz and Barkan, 2000). This makes it possible to separate these two sources of oxygen in the ocean.

In order to measure the isotopic composition of dissolved oxygen, a mass

spectrometer must be used. To make measurements of dissolved gases, the gases must first be extracted from solution, because only the gases themselves can be measured on the mass spectrometer. One common method of extracting gases to measure oxygen isotopes is to take bottle samples of water and allow the dissolved gases to exchange with gases in the headspace. After an equilibration time of 8 hours (Emerson et al., 1999) to 24 hours (Sarma et al., 2005), the headspace gas can be sampled on a mass spectrometer. This technique has been used to measure $\Delta^{17}O$ around the world (e.g. Hendricks et al., 2004; Juranek and Quay, 2005; Sarma et al., 2005; Reuer et al., 2007; Stanley et al., 2010). A major limitation of this method is that it is time consuming, which limits the number of samples that can be measured, and the timescales of the processes that can be observed.

A technique used to take continuous measurements of dissolved gases is Membrane Inlet Mass Spectrometry (MIMS). In this method, the mass spectrometer has a semi-permeable membrane at its inlet. Dissolved gases pass through the membrane and are measured in the mass spectrometer. This technique has been used to measure O_2, N_2, Ar, CO_2, dimethyl sulfide (DMS), and H_2S (Tortell, 2005; Kaiser et al., 2005; Guéguen and Tortell, 2008), but has not been used to measure oxygen isotopes.

Another method of taking rapid measurements of dissolved gases is to use an equilibrator. In an equilibrator, a large surface area of contact between headspace gas and water allows gases in the water to exchange rapidly with gases in the headspace. The headspace gas is then sampled in real time, allowing for continuous measurements of the gas of interest. A large surface area at the air-water interface can be achieved through the use of a showerhead, where water "rains" down into a headspace, and gases can exchange on the surfaces of water droplets (e.g. Johnson, 1999), a bubbling system, where gases can exchange on bubble surfaces (e.g. Copin-Montegut, 1985; Schneider et al., 1992), or other surfaces inside the equilibrator, such as marbles (e.g. Frankignoulle et al., 2001). These equilibrators have been used very successfully for measurements of carbon dioxide, because carbon dioxide is very soluble in water and therefore exchanges quickly.

Using an equilibrator to measure O_2 is more challenging than measuring

CO_2. O_2 is much less soluble than CO_2, which means the gas flux of O_2 is lower, and the equilibration time is longer. For example, an equilibrator described by Schneider et al. (2007) has a time scale for equilibration of around 1 hour for O_2, compared with around 1 minute for CO_2 (Körtzinger et al., 1996). Faster equilibration of O_2 can be achieved by reducing the headspace volume or increasing the surface area of the air-water interface. For example, Schneider et al. (2007) describe a bubble-type equilibrator used to measure O_2 that has a much smaller headspace volume than a similar equilibrator used for CO_2, an increased airflow, and a "frit" to increase bubble formation. In another study, Cassar et al. (2009) use a very small device ("Liquicel MicroModule Membrane Contactor") as an equilibrator for O_2. This device contains porous membranes that create a large, compact surface area that separates water from a very small headspace volume. This device was used to measure O_2 and Ar, and had a time constant of 7-8 minutes.

The techniques described above for measuring dissolved oxygen could also be used to measure dissolved oxygen isotopes if the equilibrating instrument were interfaced with an appropriate mass spectrometer. The isotope ratio mass spectrometer that we use requires a high flow rate of gas to stabilize the pressure in the mass spectrometer as the changeover valve switches, which allows for faster switching between the sample and reference gases (Keeling et al., 2004). Additionally, a high flow rate allows water vapor to be removed from the sample using a cold trap. For these reasons, a device such as the MicroModule Membrane contactor employed by Cassar et al. (2009) would be unsuitable because it provides a sampling flow rate that is much too low. In this chapter, we describe an equilibrator that was designed for rapid equilibration of oxygen and allows for a sampling flow rate of 3 mL/min. It allows gas exchange on the surfaces of water droplets from a showerhead, bubbles, and Raschig rings, and has a headspace volume of approximately 930 mL. We also present a model to describe the equilibration of major gases (O_2, N_2, and Ar), as well as oxygen isotopes, which differs from models for CO_2 equilibration because of the need to account for dilution of major gases by other major gases. The equilibrator, when interfaced with an IsoPrime isotope ratio mass spectrometer, allows for continuous measurements of dissolved oxygen

and its isotopes, and has the potential to aid in our understanding of dissolved gas processes.

2.2 Methods

2.2.1 Mass spectrometer

An IsoPrime isotope ratio mass spectrometer was used to measure dissolved gas composition. This mass spectrometer has a flight tube, source, and detector integrated into a single stainless steel enclosure, and has ten collectors to simultaneously measure ten m/z ratios: 28, 29, 30, 32, 33, 34, 36, 40, 44, and 45. This allows for the measurement of $\delta(O_2/N_2)$, $\delta(Ar/N_2)$, and $\delta(O_2/Ar)$, as well as $\delta^{18}O$ and $\delta^{17}O$, where $\delta(a/b)$ is defined similarly to Equation 2.1:

$$\delta(a/b) = \frac{(a/b)_{sample}}{(a/b)_{reference}} - 1 \tag{2.4}$$

The difference in ratios between the sample and the reference gases is very small, so the delta values are multiplied by 10^3 to give units of per mil, or 10^6 to give units of per meg.

The mass spectrometer employs an inlet system (Figure 2.1) designed following Keeling et al. (2004) to allow for continuous sampling, but modified to run at a lower flow rate. Specifically, a Licor NDIR CO_2 analyzer was removed and the lines were changed to 1/16" stainless steel to reduce the volume of the inlet system. Sample and reference gases flow through precision flow control valves at 3 mL/min and pressures of 500 torr. The pressure is controlled by MKS Type 250 controllers and 10 torr differential pressure transducers, which are referenced to a volume with a pressure of 500 torr. Gases then flow through a changeover valve, which determines whether the sample gas or the reference gas enters the mass spectrometer. The pressure in the line to the mass spectrometer is controlled at 300 torr to minimize pressure fluctuations as the changeover valve switches. The selected line flows through a pickoff "T," where some gas flows through a capillary tube into the mass spectrometer, and most of the gas is wasted to a vacuum.

Gas in the unselected line is also wasted, to maintain flow. The changeover valve switches every ten seconds, which allows for the calculation of delta values every 20 seconds. Upstream of the mass flow meter in Figure 2.1, sample gas flows through a -55^{o}C trap made of a 16.5 cm long piece of 1/4" stainless steel tubing filled with 3 mm glass beads to reduce its volume. This trap removes water vapor from the sample.

The mass spectrometer is calibrated to account for scale contraction due to incomplete sample/reference replacement during switching ("cross-over contamination"), as in Keeling et al. (2004). This calibration is of the form:

$$\delta(O_2/N_2) = a\delta(32/28) \tag{2.5}$$

where $\delta(32/28)$ is the measured value from the mass spectrometer, and a is the correction factor needed to convert the measurement to $\delta(\mathrm{O_2/N_2})$.

To find a, a gravimetric method was used in which a cylinder of air was prepared to be highly enriched in $\mathrm{O_2}$, by adding pure $\mathrm{O_2}$ to an evacuated cylinder, and then filling the remainder of the cylinder with air. The cylinder was weighed after evacuation, after $\mathrm{O_2}$ addition, and after it was filled. From these weights, the final composition of the gas in the cylinder was determined. The gas composition was then measured on the mass spectrometer. The ratio between the $\delta(\mathrm{O_2/N_2})$ of the gas in the cylinder, calculated from the weights of the added gases, and the $\delta(32/28)$ measured on the mass spectrometer gives the correction factor, a. For this mass spectrometer, a was determined to be 1.2. This high correction factor is likely due to the low flow rate of the gases, which would increase the cross-over contamination.

2.2.2 Equilibrator

The equilibrator is a "counterflow" type equilibrator, where gas and water flow in opposite directions. It uses water droplets, bubbling, and Raschig rings to create the surface area for gas exchange. The equilibrator is made of clear, 5.2 cm I.D. PVC pipe which is 53.3 cm long (Figure 2.2). Water showers down from the top of the equilibrator and gas bubbles up from the bottom. The equilibrator is

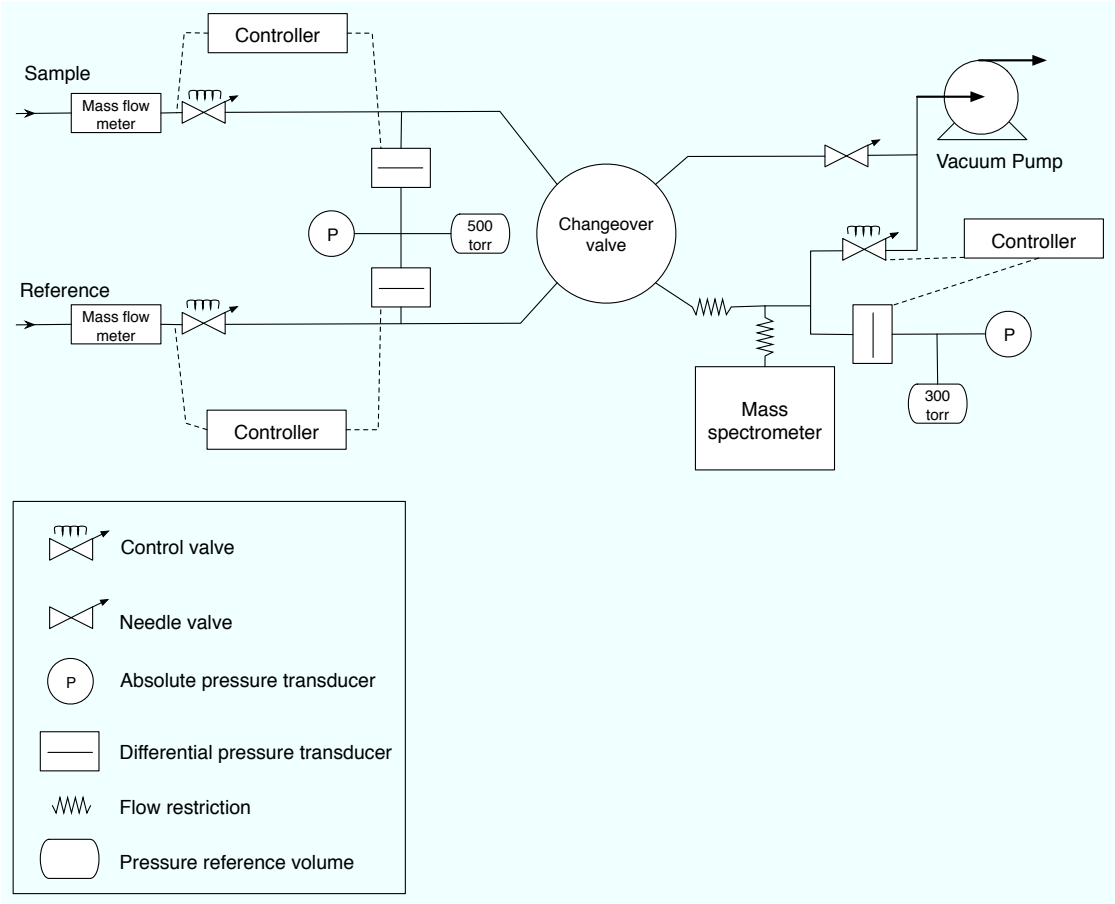

Figure 2.1: Flow diagram for the mass spectrometer inlet. Pressures in the sample and reference lines and the line going to the mass spectrometer are controlled by MKS Type 250 controllers. The changeover valve selects between the sample and reference gases every 10 seconds. A fraction of the selected gas goes through a capillary into the mass spectrometer for sampling. The rest of the selected gas and the unselected gas are wasted to a vacuum pump.

filled with 12 mm glass Raschig rings, which are small hollow cylinders that provide a large surface area for gas exchange between the air and water, and increase the time it takes for water and gas to travel through the equilibrator. The air pressure in the equilibrator is controlled using a pressure-control loop, as described below.

Water falls from a showerhead at the top of the equilibrator and exits the equilibrator through a parallel 5.2 cm I.D. PVC pipe, with 2.5 cm diameter holes drilled every 7.6 cm. Rubber stoppers can be placed inside the holes to change the height of the water outlet. A balance between the water outlet height and the air pressure inside the equilibrator determines the water height inside the equilibrator. If the water level of the outlet is too low relative to the pressure inside the equilibrator, the water level inside the equilibrator will be too low, and large bubbles will escape from the equilibrator, making full equilibration of the headspace gas impossible. If the water level of the outlet is too high, water will rise inside the equilibrator and eventually be pulled into the air lines. The adjustable water outlet height allows the equilibrator to be used under a wide range of pressures without the water level inside the equilibrator getting too low or too high. The water level in the equilibrator also determines how much of the gas exchange occurs on bubble surfaces, and how much of the exchange occurs on Raschig rings or water droplets. A clear 1/2" diameter tube runs parallel to the main equilibrator tube, and is connected at the bottom and top of the equilibrator. This tube fills with water to a height equal to the mean water level in the equilibrator and acts as a "sight glass" to observe the water level. It is difficult to observe the mean water level in the equilibrator itself because there are many large air pockets as the water and air flow around the Raschig rings.

Gas enters the equilibrator through a 1/4" stainless steel tube in the bottom of the equilibrator, and exits through the top of the equilibrator, via an opening next to the showerhead. An absolute pressure transducer is connected to the top of the equilibrator to measure the headspace pressure. A KNF Type N05 diaphragm pump circulates the air in the equilibrator at 0.5-1 L/min through a loop made of 1/8" stainless steel tubing (Figure 2.3). The total volume of the gas and water in the loop and equilibrator is approximately 1200 mL. 3 mL/min of gas (STP) is

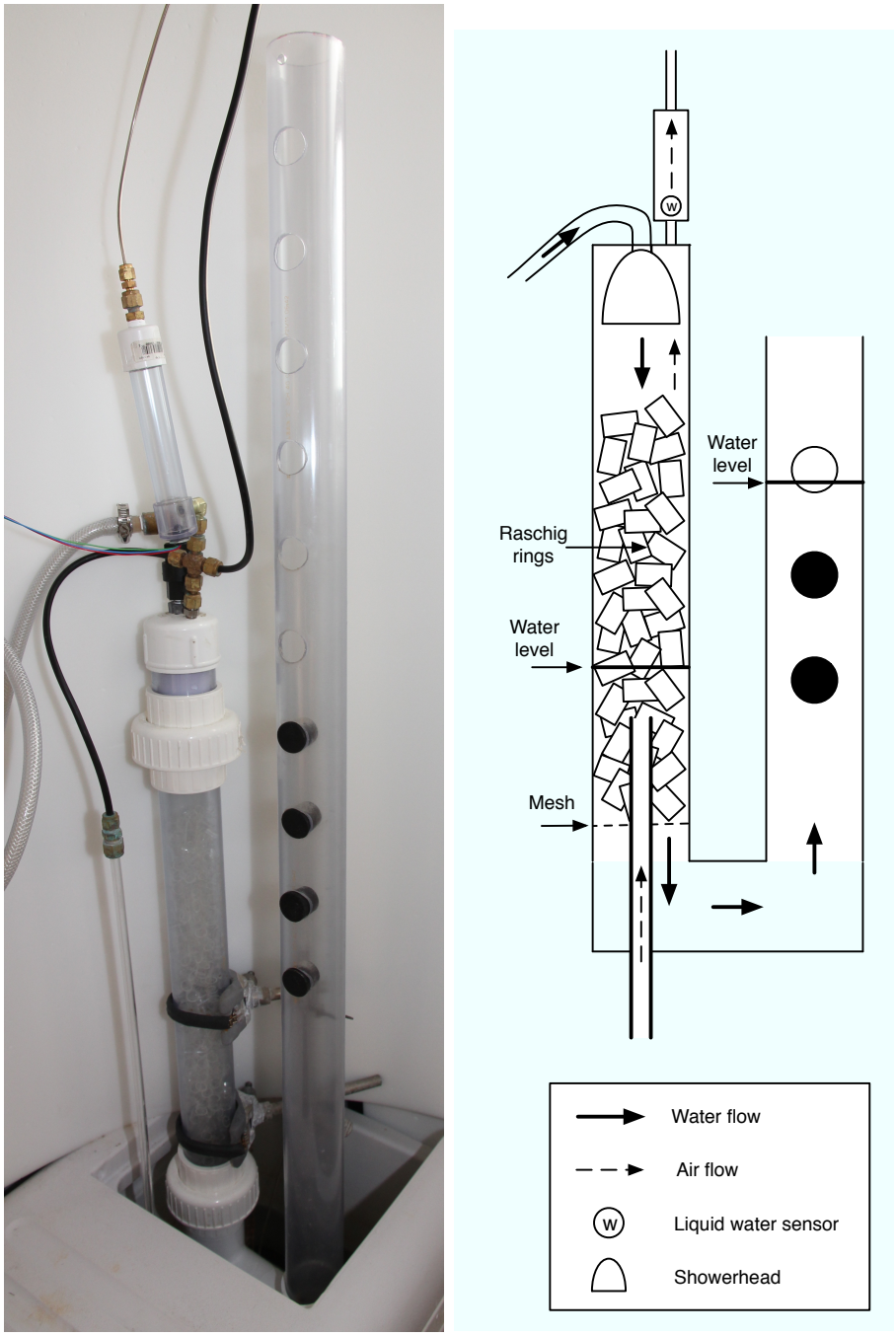

Figure 2.2: Equilibrator used to measure dissolved oxygen. The line drawing (right) shows the air and water flows in the equilibrator.

continuously drawn into the mass spectrometer, via a "T" in the loop that connects to 1/16" stainless steel tubing, which connects to the cold trap, and then to the mass spectrometer inlet system.

In most equilibrators, the headspace pressure is kept at atmospheric pressure, using a vent to the surrounding air. The headspace pressure in this equilibrator can be actively set. In order to keep the loop pressure at the setpoint, the gas lost to the mass spectrometer or to bubbles escaping from the equilibrator is replaced by gas from a makeup cylinder. The flow rate of gas from the makeup cylinder to the loop is measured by an electronic bidirectional mass flowmeter (Honeywell, AMW2150V) with a range of ±30 mL/min. The amount of gas that enters from the makeup cylinder is controlled using an absolute pressure transducer, a precision flow control valve, and an MKS Type 250 controller. If the pressure in the loop is too low, the valve opens and gas from the makeup cylinder enters the loop. If the pressure is too high, the valve closes and air is pulled out of the loop through a continuously running 300 torr vacuum until the pressure in the loop drops to the setpoint. This system keeps the equilibrator at the setpoint pressure.

One of the biggest risks of running equilibrated gas into a mass spectrometer is the possibility of seawater entering the mass spectrometer. This risk is in part avoided by having a cold trap upstream of the mass spectrometer; small amounts of water will freeze out of the sample before going into the mass spectrometer. However, a large pressure spike in the loop could draw more water into the sample line than can be removed by the cold trap. To eliminate the possibility of seawater getting into the mass spectrometer, a liquid water sensor was installed in a clear, 2.0 cm I.D. PVC pipe in the air line at the top of the equilibrator. If water from the equilibrator gets into the air line, a 4-port, 2-position valve that is interfaced to the sensor will isolate the equilibrator from the sampling loop.

2.2.3 Gas tension device

For the setpoint pressure inside the equilibrator, we chose to target the total gas tension of water, which was independently measured. Gas tension is defined as

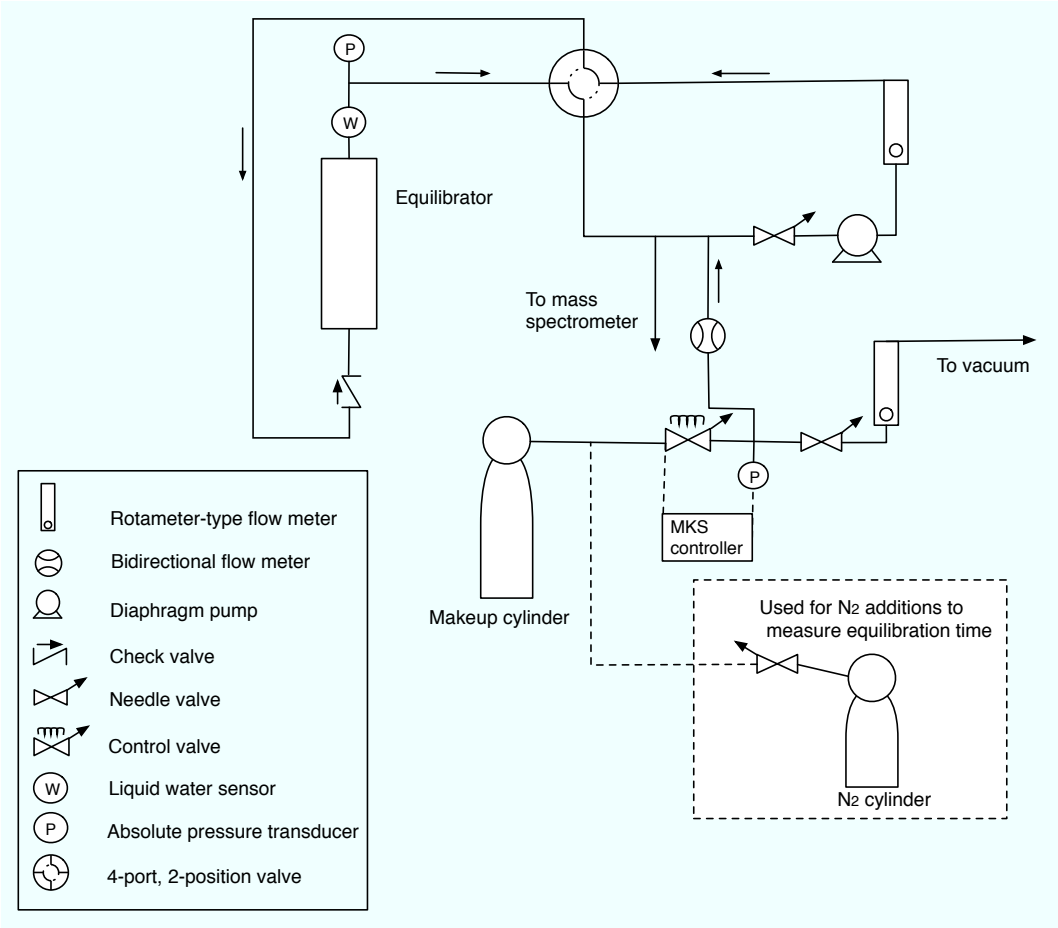

Figure 2.3: Air flow in the pressure-controlled equilibrator loop. Dashed region and line show the setup for N_2 gas additions to determine the equilibration time, as described in Section 2.4.1.

the sum of the partial pressures of gases dissolved in water, including water vapor. It can be approximated as:

$$P_T = P_{N_2} + P_{O_2} + P_{Ar} + P_{H_2O} \tag{2.6}$$

where P_T is the total gas tension and P_x is the partial pressure of gas x.

Commercial devices exist to measure gas tension (McNeil et al., 2005, 2006). However, these devices either have a long time constant (e.g. 11 minutes, McNeil et al., 2005), or need to be a few meters underwater to work properly (e.g. McNeil et al., 2006). We built a fast-responding gas tension device (GTD) using a Liquicel 0.75x1 MicroModule Membrane Contactor (Membrana, Figure 2.4). The MicroModule Membrane Contactor is a polycarbonate housing containing a porous polypropylene membrane shaped into hollow fibers, with a total surface area of 392 cm^2. Inside the hollow fibers, there is an air volume of 3.4 mL. Because the membrane is hydrophobic, liquid water cannot pass through the pores unless a pressure threshold is exceeded. Water vapor, however, will pass through the pores. At equilibrium, the pressure of the gas in the air volume equals the total gas tension.

The contactor housing has two tubes for water flow, and one tube that connects to the air volume. Water is pumped over the outside of the fibers, allowing gases to exchange between the water and the air volume. A needle valve downstream of the GTD keeps the water pressure inside the GTD constant and high (around 25 kPa) so that gas tension measurements are not affected by changes in the pump pressure. A differential pressure transducer (All-Sensors Corp., range of 56 torr) is attached to the air tube via a 68.6 cm long, 1/16" diameter stainless steel tube to measure the pressure of the gas in the air volume. A barometer is used to convert the differential pressure to absolute pressure.

2.2.4 Field setup

The equilibrator, gas tension device, and mass spectrometer were used at the end of the pier at the Scripps Institution of Oceanography (SIO), in La Jolla, CA (32^o 52.52' N, 117^o 15.30' W) from June 22-August 1, 2011. The pier extends 330.4 m from shore and is 10.2 m above mean lower low water level (MLLW). The

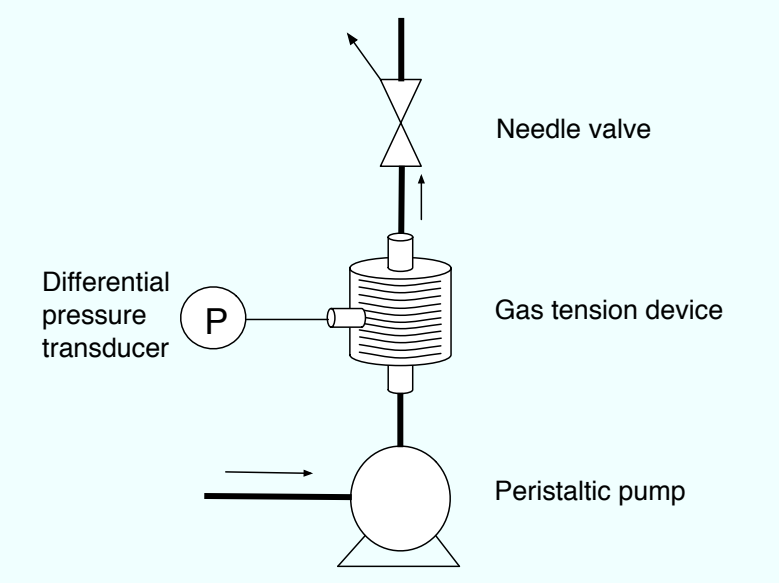

Figure 2.4: Schematic of the gas tension device. A peristaltic pump pushes water through a MicroModule Membrane Contactor, which is connected to a differential pressure transducer. A needle valve keeps the hydrostatic pressure high in the gas tension device. Thick lines show water flow, and the thin line is a static air volume.

instruments were housed in an air conditioned room with a hole in the floor that allowed for water sampling. A "filtered effluent pump" (Little Giant) was lowered through the hole to around 2 m below MLLW. It pumped water up through a 18 m long 3/4" diameter rubber hose at a flow rate of 40 L/min into a line which filtered and diverted the water to different water streams (Figure 2.5). The high flow rate kept the residence time in the hose short (8 seconds), which helped prevent warming of the water before it went through the equilibrator.

Most of the water was diverted into a 95 L insulated tank (Igloo Products Corp.), in which the GTD and an Aanderaa optode O_2 sensor were submerged. The rest of the water flowed through a 130 micron Amiad strainer that was modified to be self-cleaning, as explained below. The water flow then split, with 5.6-5.8 L/min flowing to the equilibrator, measured using a paddlewheel-type water flow sensor (Gems Sensors), and the rest of the water flowing into a 2 L metal beaker lined with nested filter bags (50, 25, and 10 microns). The filtered water was pumped from this beaker through the GTD at 100 mL/min using a peristaltic pump. Water

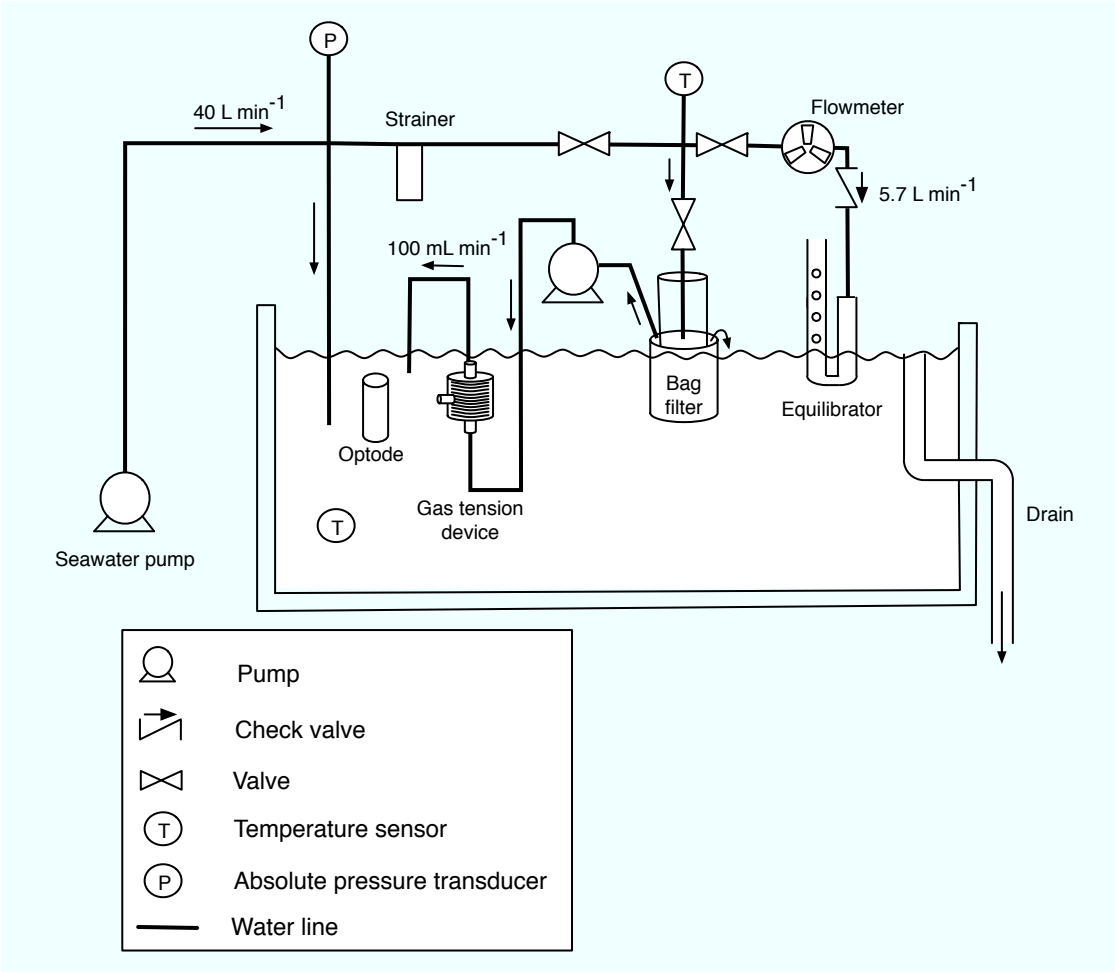

Figure 2.5: Water flow at the Scripps Institution of Oceanography pier. Water is pumped from a depth of 2 m below MLLW. Most of the water goes into a tank which houses the optode and gas tension device. The rest of the water is filtered with a 130 micron strainer. This water goes into a bag filter, from which water is pumped through the gas tension device, or into the equilibrator, which is shown in Figure 2.2.

exited the 95 L tank through a pipe inserted into a 5.1 cm hole cut into the side of the tank. The height of the pipe inlet inside the tank set the water level in the tank. Temperature sensors were placed in the line to the equilibrator and in the tank. A pressure transducer was placed at the downstream end of the hose to monitor the pump head pressure.

In the nearshore environment, there is so much algae and sand in the water that the strainer would clog quickly. The strainer had a removable valve at the bottom, which could be opened so that instead of water flowing through the strainer to the rest of the water line, water would flow inside the strainer and out the bottom, clearing out filtered particles that had collected inside the strainer. However, the strainer clogged so quickly (often in less than 1 hour) that manually clearing the strainer was not practical for continuous use. Furthermore, the filtered algae caused the particles to be too sticky to be flushed away from the strainer when the valve was opened. To correct this issue, the valve was removed and a bottle brush which just fit into the strainer cylinder was inserted through a "T" into the bottom of the strainer. The end of the brush was coupled to a rotating motor. At the arm of the "T," a solenoid valve was attached. When the flow rate to the equilibrator dropped below 5.3 L/min, signaling that the strainer was clogging, the motor automatically started rotating, and the valve opened. The rotating brush swept away sand and organic matter from the strainer, while the diverted flow washed the filtered sediment out of the bottom of the strainer. This stopped the flow to the equilibrator for 5-10 seconds at a time. When the water flow to the equilibrator stopped and started again, the pressure would change in the equilibrator, and the loop would have to adjust back to the pressure setpoint. The self-cleaning strainer allowed the water to flow continuously without manual intervention.

2.3 Mathematical model of equilibrator

Understanding the equilibration time in this equilibrator is complex for two reasons. Firstly, we are equilibrating major gases, and not just the minor species.

Therefore, changes in the mole fraction of one gas (such as oxygen) will cause changes in the mole fraction of another gas (such as nitrogen) because of dilution. Secondly, because our equilibrator is kept at constant pressure, gas must enter from a cylinder or leave the equilibrator in order to keep the pressure constant. To understand the behavior of our equilibrator, we use a forward model. Following Johnson (1999), we first present a closed model, where headspace gas is only influenced by exchange with gas dissolved in water, and then expand to a more realistic model where gas is removed from the headspace for sampling, and replaced with gas from a makeup cylinder.

For a closed model, the rate of change in the number of moles in the headspace can be defined as:

$$\frac{\delta N_i}{\delta t} = F_{i,water} \tag{2.7}$$

where N_i is the number of moles of gas i in the headspace, and $F_{i,water}$ is the flow rate of gas i entering the headspace from the water (mol/min).

$F_{i,water}$ is determined using an idealized case where water flows through a box without mixing and exchanges with gas in a headspace (Figure 2.6). For this case, $F_{i,water}$ can be derived to be:

$$F_{i,water} = Q(C_i - SP_i)(1 - e^{-k/Q}) \tag{2.8}$$

where Q is the water flow rate (L/min), S is the Henry's law solubility constant (mol/(L atm)), P_i is the pressure of gas i in the headspace (atm), C_i is the concentration of gas i dissolved in the water entering the equilibrator (mol/L), and k is the gas exchange coefficient (L/min). All of these parameters can be measured directly except k. This equation is applied to N_2, O_2, and Ar. k is set for O_2, and then scaled to N_2 and Ar using a square root dependency on the ratio of the Schmidt numbers (Wanninkhof, 1992). The sum of Equation 2.8 for N_2, O_2 and Ar is used to determine the change in the total number of moles in the headspace.

This model differs from the model described in Johnson (1999) in that the gas exchange is explicitly computed using a gas exchange coefficient, k, rather than assuming that a constant fraction of total possible equilibration occurs as a water

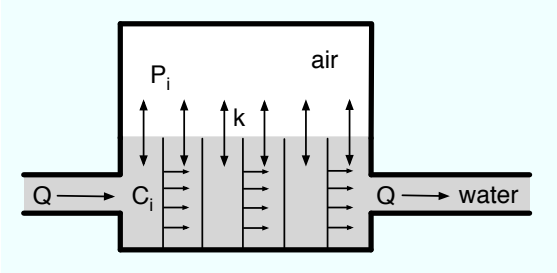

Figure 2.6: Model of gas transfer between water and headspace. Q is the water flow rate, P_i is the headspace pressure of gas i, C_i is the concentration of gas i in the water entering the equilibrator, and k is the gas exchange coefficient

parcel flows through the equilibrator. Our model allows gas exchange to be limited by either Q or k, as shown in Equation 2.8. In the limit where the gas exchange coefficient is much higher than the water flow rate ($k/Q >> 1$), the flux of gas becomes:

$$F_{i,water} = Q(C_i - SP_i) \tag{2.9}$$

and is limited by the flow rate, Q. In the limit where the water flow rate is much higher than the gas exchange coefficient ($k/Q << 1$), the flux of gas becomes:

$$F_{i,water} = k(C_i - SP_i) \tag{2.10}$$

and is limited by the gas exchange coefficient, k.

Assuming C_i is constant with time, Equations 2.7-2.8 can be integrated to determine $N_i(t)$, by substituting $\frac{P_d N_i}{N_d}$ for P_i:

$$N_i(t) = \frac{C_i N_d}{SP_d} + \left(N_0 - \frac{C_i N_d}{SP_d} \right) e^{-t/\tau_c} \tag{2.11}$$

where P_d is the total headspace pressure of dry air, defined as $P_{total} - P_{H_2O}$, N_d is the total number of moles of dry air, N_0 is the initial value of N_i, and the time constant for the closed system, τ_c, is given by:

$$\tau_c = \frac{N_d}{QSP_d(1 - e^{-k/Q})} \tag{2.12}$$

If we consider the limits above ($k/Q >> 1$ or $k/Q << 1$), the time constant simplifies to:

$$\tau_c = \frac{N_d}{QSP_d} \qquad (k/Q >> 1) \tag{2.13}$$

or

$$\tau_c = \frac{N_d}{kSP_d} \qquad (k/Q << 1) \tag{2.14}$$

Oxygen isotopes are also modeled to determine δ^{18}O and Δ^{17}O. The flux of $^{18}O^{16}O$ or $^{17}O^{16}O$ can be expressed as:

$$F_{x,water} = Q(C_{O_2} - SP_{O_2}R_x\alpha_{eq,x})(1 - e^{-k\alpha_{k,x}/Q}) \tag{2.15}$$

where x is $^{18}O^{16}O$ or $^{17}O^{16}O$, R_x is the ratio of the oxygen isotope to $^{16}O_2$ in the air, $\alpha_{eq,x}$ is the equilibrium fractionation factor for oxygen dissolution into water, and $\alpha_{k,x}$ is the kinetic fractionation factor for oxygen dissolution into water. $\alpha_{eq,18}$ is 1.00073 at a water temperature of 19^{o}C (Benson and Krause, 1980) and $\alpha_{k,18}$ is 0.9972 (Knox et al., 1992). $\alpha_{eq,17}$ and $\alpha_{k,17}$ are determined by assuming that the fractionations are mass-dependent with a relationship of 0.52, giving values of 1.00038 and 0.9985, respectively. The modeled $^{18}O^{16}O$ and $^{17}O^{16}O$ values can be used with O_2 to determine δ^{18}O and Δ^{17}O.

We now explore a more realistic model where, instead of a closed system, gas is removed for sampling and added from a cylinder to keep the pressure constant at a setpoint. In this case, the rate of change in the number of moles in the headspace becomes:

$$\frac{\delta N_i}{\delta t} = F_{i,water} + X_{i,cyl}F_{cyl} - X_{i,h}F_{exit} \tag{2.16}$$

where $X_{i,cyl}$ is the mole fraction of gas i in the cylinder, F_{cyl} is the flow rate of gas entering the headspace from the cylinder (mol/min), $X_{i,h}$ is the mole fraction of gas i in the headspace, and F_{exit} is the flow rate of gas leaving the headspace (mol/min), from bubble loss and sampling. Here, the mole fractions and flow rates are for water-free headspace air. This model does not explicitly account for gas loss due to bubbles escaping from the equilibrator.

The pressure in the headspace, and therefore the total number of moles, remains constant. This means that the sum of Equation 2.16 for O_2, N_2 and Ar is defined as zero, which allows for the calculation of F_{cyl}, since F_{exit} is prescribed by the mass spectrometer sampling rate and bubble loss. Through the calculation of F_{cyl}, the equilibration of one major gas is linked to the equilibration of other

major gases. This differentiates our model from models of trace gas equilibration, including Johnson (1999).

When the headspace pressure is close to the total gas tension, the net flux of gas into the headspace will be close to zero. In this typical case, F_{exit} will be greater than the net flux of gas from the water, and gas will need to be added from the cylinder. If F_{water} is the sum of the fluxes of all the gases ($F_{water} = \Sigma F_{i,water}$), then in the typical case where $\mathrm{F}_{exit} > \mathrm{F}_{water}$,

$$F_{cyl} = F_{exit} - F_{water} \tag{2.17}$$

If the setpoint pressure in the headspace were much lower than the gas tension, gases would be stripped out of the water. In this case, F_{water} could be greater than F_{exit}, and no gas would be added to the loop from the cylinder. Instead, gas would be lost from the loop to the vacuum, through the bidirectional flow meter shown in Figure 2.3, to maintain the setpoint pressure.

The model described in Equation 2.16, where gas is sampled from the loop and added to the loop from a cylinder, introduces a new time constant due to sampling, τ_s:

$$\tau_s = \frac{N}{F_{cyl}} \tag{2.18}$$

This time constant reduces the total adjustment time of the system, as also described in Johnson (1999). Furthermore, when gas is constantly added, the headspace gas composition can never reach complete equilibrium with gas in the water. The time constants can be combined to get the overall time constant, as in Johnson (1999):

$$\frac{1}{\tau_o} = \frac{1}{\tau_c} + \frac{1}{\tau_s} \tag{2.19}$$

As mentioned above, every parameter in this model can be measured experimentally except for k. Also, although the flow to the mass spectrometer is known, F_{exit} is not, because gas loss due to bubbles contributes to F_{exit}. However, F_{cyl} can be directly measured and is equal to F_{exit} in steady state. The model is run with forward time-stepping of Equation 2.16 to compute the gas composition of the headspace as equilibration occurs. Below, we use experiments and model runs to

determine the value of k, and explore the equilibration time and the measurement errors introduced by the equilibrator.

2.4 Results

2.4.1 Equilibration time of the equilibrator

The equilibration time of the equilibrator determines its time resolution relative to ambient changes. As shown in Equations 2.12 and 2.19, the time constant, τ_o, depends on both the water flow rate (Q) and k. The water flow rate is measured during experiments, but k is not. However, τ_o can be determined experimentally to derive k.

We measured the equilibration time by running seawater through the equilibrator as explained in Section 2.2.4, with gas circulating through the equilibrator at a fixed pressure. A "T" was put into the makeup cylinder line, and attached to a valve and a cylinder filled with nitrogen gas (dashed box in Figure 2.3). After the headspace gas composition stabilized, the valve connecting to the N_2 cylinder was opened to add a small amount of N_2 gas into the makeup gas stream, perturbing the headspace gas composition. Because the natural variability of $\delta(Ar/N_2)$ is lower than $\delta(O_2/N_2)$, we looked at the response in $\delta(Ar/N_2)$ as the headspace returned to the gas composition before the N_2 gas addition.

This test was repeated 4 times. For each test, a function of the form:

$$\delta(Ar/N_2) = H[t-a] \times be^{(-t/\tau)} + d + et \tag{2.20}$$

was fit to the data (e.g. Figure 2.7), where H is the Heaviside step function. The resulting values of τ were then averaged using a weight of $1/\sigma^2$. The weighted average and standard deviation of τ is 7.36 $\pm$ 0.74 minutes.

The model described in Equation 2.16 can be used to relate τ_o to k. The model was initialized with the headspace gas composition simulating a N_2 spike; the initial N_2 concentration was high, and the O_2 and Ar concentrations were diluted proportionally. Parameters were set to reflect values measured during sampling at the SIO pier. We used a water flow rate of 5.6 L/min (the mean water flow during

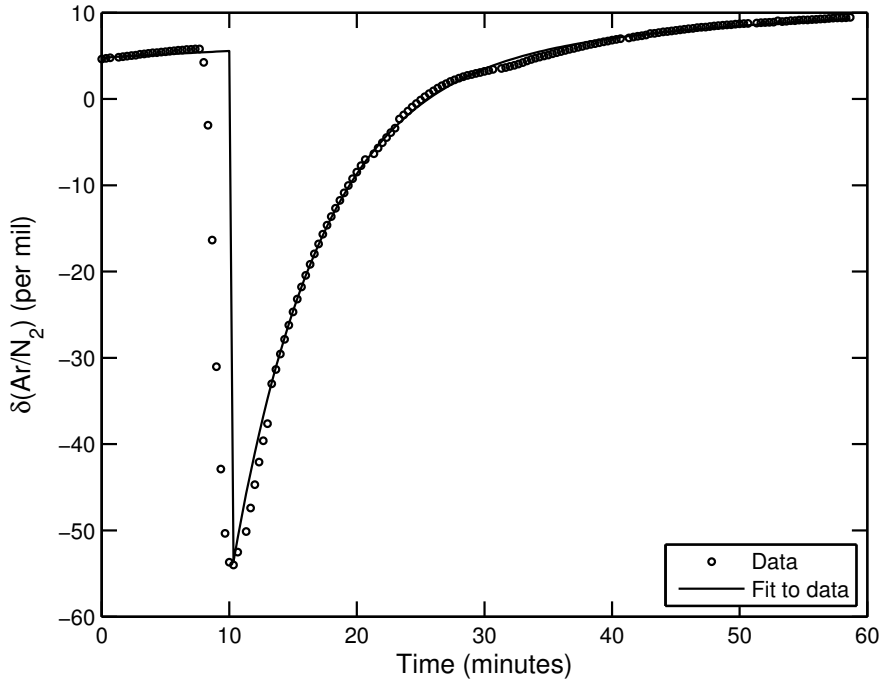

Figure 2.7: Response in $\delta(\mathrm{Ar}/\mathrm{N}_2)$ to N_2 gas addition during one test. The line shows the fit using Equation 2.20. Data between 6 and 13 minutes were removed for the fit. The weighted average of τ based on four tests is 7.36 ± 0.74 minutes.

sampling), a headspace volume of 930 mL (the measured total equilibrator loop volume minus the estimated water volume in the equilibrator, based on the water height), and an F_{cyl} of 5 mL/min (measured using the bidirectional flowmeter). Equation 2.16 was run with forward time-stepping to model the response of the headspace gas as water with a different dissolved gas composition flowed through the equilibrator. The model was run until $\delta(Ar/N_2)$ of the headspace was stable. An equation of the form:

$$y = ae^{(-t/\tau)} + c \tag{2.21}$$

was fit to the model output of $\delta(Ar/N_2)$ versus time, where τ is the e-folding time of equilibration. This was repeated for 18 values of k_{O_2} between 5 and 75 L/min. The results are shown in Figure 2.8.

Although k is a fixed property of the equilibrator, the model results show that τ for a given k varies depending on the dissolved oxygen concentration of the water (not shown). However, this variability is small relative to the uncertainty in the measured τ. We show results of the response of τ to k for a dissolved gas composition in the middle of the range of measured O_2 concentration.

As shown in Figure 2.8, τ, approaches an asymptote at large values of k_{O_2}. Using Equations 2.13, 2.18, and 2.19, τ_o can be computed for the limit where k/Q approaches infinity. τ_o is 5.14 minutes for O_2, and 10.74 minutes for N_2. The forward model asymptotes to a τ of 6.0 minutes for $\delta(O_2/N_2)$ at large values of k. This value falls between the values of τ_o for O_2 and N_2.

Based on the model results shown in Figure 2.8, k_{O_2} at the mean measured τ is 9.1 L/min. The range in k_{O_2} based on the standard deviation in the measured τ is 7.3-12.8 L/min. Our system is approaching the high k/Q limit where τ is insensitive to k.

2.4.2 Corrections for incomplete equilibration

The observed steady state headspace composition can differ from what is expected from true equilibration due to the influence of the makeup gas, as well as the differences between the actual gas tension and the headspace pressure. The overall difference can be expressed as an additive correction, x. For example, for

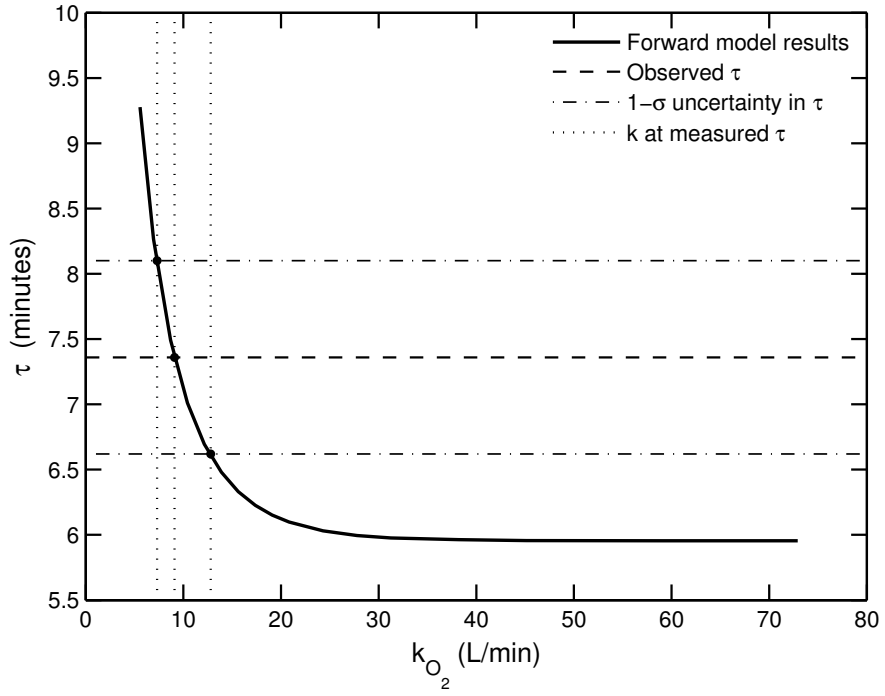

Figure 2.8: Response of the time constant for $\delta(\mathrm{Ar}/\mathrm{N}_2)$ (τ), to k_{O_2} at a water flow rate of 5.6 L/min. At large k_{O_2}, τ becomes insensitive to k_{O_2}. Horizontal dashed lines show the mean and 1-σ uncertainty of τ determined experimentally (7.36 ± 0.74 minutes). Vertical dotted lines show the values of k_{O_2} corresponding to the measured τ (7.3 L/min, 9.1 L/min, and 12.8 L/min).

$\delta(O_2/N_2)$,

$$x = \delta(O_2/N_2)_{water} - \delta(O_2/N_2)_{observed} \tag{2.22}$$

where $\delta(O_2/N_2)_{observed}$ is the observed steady state headspace composition, and $\delta(O_2/N_2)_{water}$ the composition in equilibrium with the water.

To determine how the correction varies with headspace pressure and dissolved gas composition, we ran the model with a range of headspace pressures and dissolved gas compositions using conditions similar to our typical operating conditions, with a total gas tension of 790 torr and a Q of 5.6 L/min. The correction also varies with F_{cyl}, for which we used the makeup flow rate, measured by the bidirectional flow meter. Here we only show results using an F_{cyl} of 5 mL/min.

The correction takes into account the extent of equilibration, the sensitivity to pressure, and the sensitivity to the difference between the measured and makeup gas compositions. The model was run for two values of k_{O_2} to illustrate the sensitivity to k_{O_2}. We show results using a k_{O_2} of 7.3 L/min and a k_{O_2} approaching infinity. As shown in Figure 2.9, the results using these values of k_{O_2} are similar.

Figure 2.9A shows results for $\delta(O_2/N_2)$. Corrections at a ΔP of 0 torr show the effect of the makeup gas addition on equilibration. For example, when the observed $\delta(O_2/N_2)$ is 50 per mil greater than the makeup gas, the correction is 2.50 per mil using a k_{O_2} of 7.3 L/min, and 1.86 per mil using a k_{O_2} approaching infinity. This is a 3.7-5.0% correction, which means that the headspace gas is around 95-96% equilibrated, and around 4-5% of the sampled gas is makeup gas. For headspace pressures higher than the gas tension ($\Delta P > 0$), the correction becomes more positive, and for headspace pressures lower than the gas tension, the correction becomes more negative. This behavior results because O_2 equilibrates faster than N_2, so pO_2 is more able than pN_2 to match the equilibrium partial pressure.

Figure 2.9B-D also shows results for $\delta(O_2/Ar)$, $\delta^{18}O$, and $\Delta^{17}O$. Compared with $\delta(O_2/N_2)$, the corrections in $\delta(O_2/Ar)$, $\delta^{18}O$, and $\Delta^{17}O$ are less sensitive to pressure. This is because the differences among the equilibration rates of Ar, $^{16}O_2$, $^{17}O^{16}O$, and $^{18}O^{16}O$ are small compared with the difference between O_2 and N_2, so the influence of pressure is not as strong.

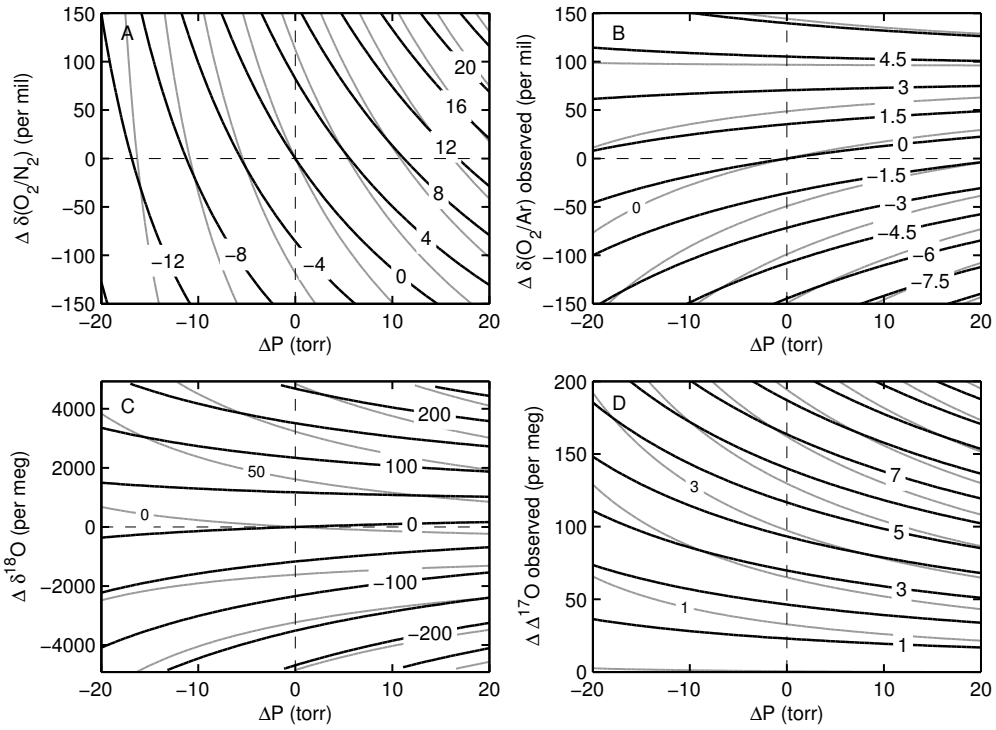

Figure 2.9: Model prediction of the sensitivity of (A) $\delta(O_2/N_2)$, (B) $\delta(O_2/Ar)$, (C) $\delta^{18}O$, and (D) $\Delta^{17}O$ to equilibrator pressure changes and gas composition changes, for a gas tension of 790 torr, a sampling flow rate of 5 mL/min, a Q of 5.6 L/min and a k_{O_2} of 7.3 L/min (black lines) or a k_{O_2} approaching infinity (gray lines). ΔP is the headspace pressure minus the gas tension. The y-axis shows the difference between the steady state delta value of the headspace (i.e. the values that would be observed) and the delta value of the makeup gas. The contour values show the correction, defined in Equation 2.22, for a k_{O_2} of 7.3 L/min, in units of per mil ($\delta(O_2/N_2)$ and $\delta(O_2/Ar)$) or per meg ($\delta^{18}O$ and $\Delta^{17}O$). Some contour values are also shown for a k_{O_2} approaching infinity.

2.4.3 Verification of model-based correction

The model-based correction to the data, described in Section 2.4.2, can be verified using simultaneous measurements of gas tension, percent O_2 saturation from the optode, and $\delta(O_2/N_2)$ and $\delta(Ar/N_2)$ from the mass spectrometer. If the presence of makeup gas were undercorrected, the apparent changes in O_2 (measured by the mass spectrometer) would be smaller than the actual changes (measured by the optode). For a three-week period, all four measurements were taken at the SIO pier.

The optode measures O_2 concentration and water temperature, and uses the solubility relationship of Garcia and Gordon (1992) to compute percent oxygen saturation. The optode was initially calibrated with a 2-point calibration using air-saturated water and a zero-oxygen solution, as described in the Aanderaa manual. This gives an internal calibration to define 100% oxygen saturation and 0% oxygen saturation. During the optode deployment at the SIO pier, Winkler titrations were taken periodically to provide an independent calibration of the optode. Based on these results, the optode readings were on average 2.9 ± 5.3 μM below the Winkler results, a mean difference of around 1.2%. The variability in ambient dissolved O_2 is small enough that correcting by applying an additive offset is roughly equivalent to multiplying by a constant factor. We multiplied the optode data by 1.012 so that the optode data matched the Winkler titrations.

A cross-correlation analysis revealed that the mass spectrometer measurements lagged the optode measurements by 8.3 minutes. The travel time from the equilibrator to the mass spectrometer is roughly 2.5 minutes, leaving a 5.8 minute lag due to the time constant of the equilibrator. This is similar but slightly lower than our measured e-folding time. In addition to a time offset, the optode can measure variability at a higher frequency than the equilibrator, because of the e-folding time of the equilibrator. To account for these effects, a 10 minute moving boxcar average was applied to the optode data, as well as a lag of 8.3 minutes.

In addition to these corrections to the optode data, some of the optode and mass spectrometer data were masked out based on the makeup flow rate. There were many occasions where the makeup flow rate, measured by the bidirectional

flowmeter, became very high (>60 mL/min) or very low (<-20 mL/min, indicating that gas was leaving the loop). As mentioned in Section 2.2.4, some of these fluctuations were due to pressure changes as the strainer cleaned out, which stopped and restarted the water flow. At flows greater than 60 mL/min, so much gas would be added to the loop that the mass spectrometer measurements would be highly influenced by the makeup gas. We defined a "spike" in the makeup flow rate as flows greater than 50 mL/min or less than -10 mL/min. All data within 30 minutes after a spike in the makeup flow rate were removed, for both the optode and mass spectrometer data. After this masking, the remaining data were averaged into hourly means. Then, the mass spectrometer hourly means were corrected for incomplete equilibration, as described in Section 2.4.2, using the mean makeup flow for that hour as F_{cyl}.

To calculate the percent oxygen saturation from mass spectrometer data, measurements of gas tension, $\delta(O_2/N_2)$, and $\delta(Ar/N_2)$ are needed. As shown in Equation 2.6, the primary contributors to the gas tension are O_2, N_2, Ar and water vapor. Water vapor pressure can be determined from temperature using (Weiss and Price, 1980):

$$ln(pH_2O) = 24.4543 - 67.4509(100/T) - 4.8489 \times ln(T/100) - 0.000544 \times S \quad (2.23)$$

where T is the temperature in Kelvin and S is the salinity in parts per thousand.

Ratios of the partial pressures of O_2, Ar, and N_2 can be computed from the corrected $\delta(O_2/N_2)$ and $\delta(Ar/N_2)$ using:

$$\frac{P_{O_2}}{P_{N_2}} = \left(\frac{\delta(O_2/N_2)}{10^3} + 1\right) \times (0.20946/0.78084) \quad (2.24)$$

where $\delta(O_2/N_2)$ is in units of per mil and (0.20946/0.78084) is the ratio of O_2 to N_2 in the atmosphere, and:

$$\frac{P_{Ar}}{P_{N_2}} = \left(\frac{\delta(Ar/N_2)}{10^3} + 1\right) \times (0.00934/0.78084) \quad (2.25)$$

where $\delta(Ar/N_2)$ is in units of per mil and (0.00934/0.78084) is the ratio of Ar to N_2 in the atmosphere.

Equations 2.6 and 2.23-2.25 were combined to determine the partial pressure of O_2. This partial pressure was then divided by 159.1896 (the partial pressure of oxygen, in torr, at a total air pressure of 760 torr) to get the percent oxygen saturation.

Figure 2.10 shows the mass spectrometer percent O_2 saturation versus the optode percent O_2 saturation. The slope of the mass spectrometer versus the optode percent O_2 was 0.94 ± 0.02. We also tested this relationship using stability criteria. To eliminate periods with rapid fluctuations in oxygen, we stipulated that, for each hourly mean data point used, the hourly means of the optode data had to be stable to within 5% oxygen saturation for 5 hours before the data point. These results are also shown in Figure 2.10. Using the stability criteria achieves a slope of 1.03 ± 0.06. These tests show that our model-based correction to the data is valid to within the uncertainties of data.

2.4.4 Equilibration time of the GTD

Since the equilibrator pressure is controlled by the gas tension, it is useful to know how quickly the gas tension device can respond to changes in the gas tension. The e-folding time of the GTD can be measured by perturbing the pressure. This was achieved by opening a vent in the 1/16" tubing that connects the GTD air volume to a pressure transducer. When the vent was opened, the pressure dropped to 0 torr relative to atmospheric pressure. When the vent was closed, the pressure gradually returned to the gas tension as water was pumped through the GTD at 100 mL/min. Equation 2.20 was fit to the response curves from six tests, as shown in Figure 2.11. These results were averaged using $1/\sigma^2$ as the weight. The weighted mean e-folding time of the gas tension device is 5.35 ± 0.59 minutes.

2.4.5 Accuracy of the GTD

The accuracy of the GTD can be determined using simultaneous measurements of gas tension, percent O_2 saturation from the optode, and $\delta(O_2/N_2)$ and $\delta(Ar/N_2)$ from the mass spectrometer, using the equations presented in Sec-

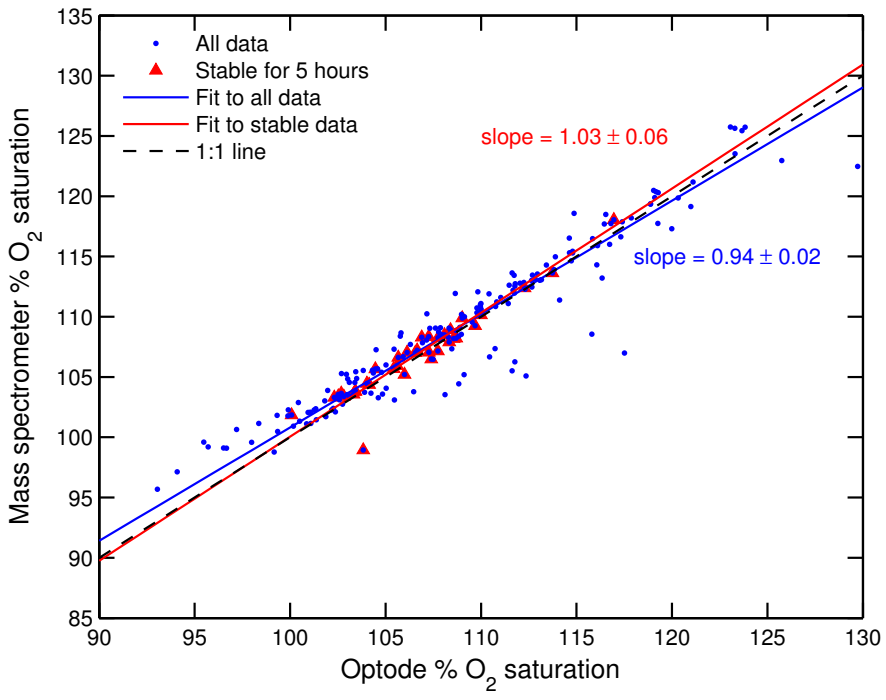

Figure 2.10: Percent oxygen saturation measured with the optode and the mass spectrometer. Data within 30 minutes after a flow rate greater than or equal to 50 mL/min or less than or equal to -10 mL/min were removed. Red triangles show points remaining after data have been removed using stability criteria stating that the oxygen percent saturation had to be within 5% for the last 5 hours for a point to be included. The blue text gives the slope of all the data, and the red text gives the slope of the stable data. Using the stability criteria, the slope of the data comes much closer to the ideal slope of 1.

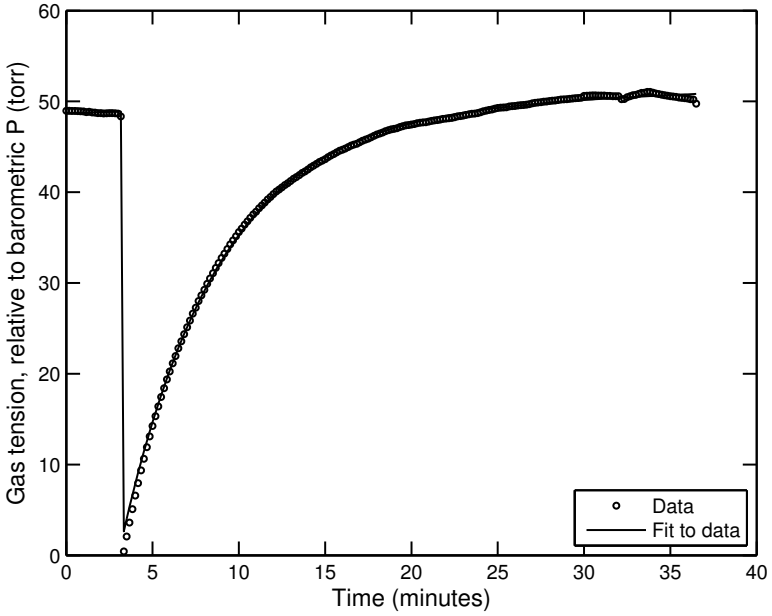

Figure 2.11: Example of gas tension device response after its air volume was vented to the atmosphere. Water was pumped through the GTD at 100 mL/min. The e-folding time is 5.35 ± 0.59 minutes.

tion 2.4.3. P_{O_2} was calculated using the optode percent O_2 saturation:

$$P_{O_2} = \%O_2 \times 159.1896 \tag{2.26}$$

and P_{N_2} and P_{Ar} were calculated using:

$$P_{N_2} = P_{O_2}/(P_{O_2}/P_{N_2}) \tag{2.27}$$

and

$$P_{Ar} = (P_{Ar}/P_{N_2}) \times P_{N_2} \tag{2.28}$$

The partial pressures of O_2, N_2, Ar, and water vapor were added together to calculate the expected total gas tension. This is compared with the measured total gas tension in Figure 2.12. On average, the measured gas tension shows variability that is similar in timing but lower in magnitude than the calculated gas tension. The measured gas tension is higher than the calculated gas tension by around 1.8

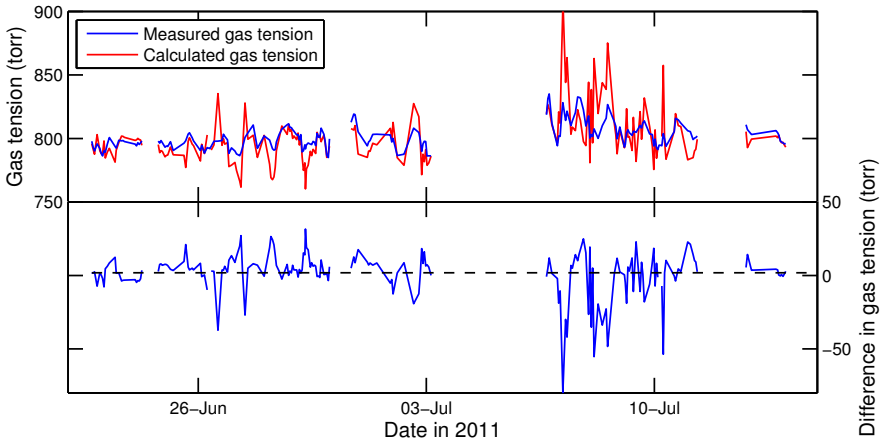

Figure 2.12: Top: Gas tension measured from the gas tension device, and calculated from the optode and mass spectrometer using Equations 2.6 and 2.23-2.28. Bottom: The calculated gas tension subtracted from the measured gas tension. The measured gas tension is on average 1.8 torr higher than expected based on the optode and mass spectrometer measurements.

torr. This is much smaller than the uncertainty, which is ±17 torr, based on the uncertainty in the optode calibration.

2.5 Discussion

The equilibrator presented here has an e-folding time of 6.5-8 minutes for O_2. This is as fast as the equilibration method described by Cassar et al. (2009), and is several times faster than using an equilibrator designed to measure CO_2. Based on model results, the e-folding time is limited by the water flow rate, rather than the gas exchange coefficient. With an e-folding time of 6.5-8 minutes, hourly changes are easily resolvable.

There are offsets introduced to the "equilibrated" air stream due to makeup gas being constantly added to the loop. The more gas added, either because of a high sampling flow rate or gas lost to bubbles escaping from the equilibrator, the further away from equilibrium the sample will be, and the larger correction that will be needed. For example, for a measured $\delta(O_2/N_2)$ of 50 per mil and no difference between the gas tension and headspace pressure, a flow rate of 3 mL/min

will need a correction of 1.5 per mil, and a flow rate of 20 mL/min will need a correction of 9.7 per mil. This emphasizes the need for a low sampling rate. Also, to avoid large bubbles escaping from the equilibrator, it is important to balance the pressure inside the equilibrator with the water outflow height, so that the water level inside the equilibrator is not too low.

The gas tension device has an e-folding time of around 5-6 minutes. This is around twice as fast the equilibrator presented in McNeil et al. (2005), and is within the range of the e-folding time of the equilibrator presented in McNeil et al. (2006). The mean measured gas tension agrees with the mean expected gas tension, which was calculated using simultaneous measurements of percent oxygen saturation, $\delta(O_2/N_2)$, and $\delta(Ar/N_2)$.

If there were an offset between the measured gas tension and the true gas tension, then the setpoint pressure inside the equilibrator would not match the true total gas tension. This would have implications for measurements of $\delta(O_2/N_2)$, $\delta(O_2/Ar)$, and oxygen isotopes, because the steady state values in the equilibrator are sensitive to differences between the headspace pressure and the total gas tension. Using our model, we computed the correction needed to bring the observed steady state values to the values in equilibrium with water for ΔP equal to ± 10 torr. The results are shown in Table 2.1. The correction expressed as a percent of the observed value (relative to makeup gas) is around 2-5% for $\delta(O_2/Ar)$, $\delta^{18}O$, and $\Delta^{17}O$. This percent correction for $\delta(O_2/N_2)$ is larger, at 10-20%, which illustrates the importance of matching the equilibrator headspace pressure to the total gas tension.

A drawback of bubble-type equilibrators is that they have been shown to cause biases in the equilibrated gas because the pressure in the bubble is higher than the ambient pressure due to hydrostatic pressure and the surface tension of the bubble (Murphy et al., 2001; Schneider et al., 2007). This equilibrator does use bubbles in its equilibration. However, the bubbles in this equilibrator are much larger than bubbles produced with a frit, so the surface tension effect is lower. Also, the circulating air only bubbles through the lower part of the equilibrator. After the air rises through the water, gases still exchange on the surface of the

Table 2.1: Examples of corrections to measured delta values needed for F_{cyl} = 5 mL/min. ΔP is the difference between the gas tension and the headspace pressure. The correction is a function of the assumed value of k_{O_2}. The range in correction values is from using a k_{O_2} of 7.3 L/min and infinity.

δ value	Observed value relative to makeup gas	Correction at ΔP = 10 torr	Correction at ΔP = -10 torr
$\delta(O_2/N_2)$	50 per mil	10.0 to 10.4 per mil	-6.3 to -5.4 per mil
$\delta(O_2/Ar)$	50 per mil	1.2 to 1.8 per mil	1.8 to 2.4 per mil
$\delta^{18}O$	-2000 per meg	-107.6 to -72.7 per meg	-66.5 to -53.6 per meg
$\Delta^{17}O$	100 per meg	3.9 to 5.1 per meg	2.3 to 3.5 per meg

Raschig rings and on the water droplets. If the bubbles did produce a bias in the gas composition, it would likely be largely removed by gas exchange on these air-water interfaces.

This equilibrator was used at a pier to measure gas composition in seawater. If the equilibrator were used on a ship, the motion of the ship would change the height of the water outlet tube relative to the equilibration tube. This would change the water height inside the equilibrator. Therefore, for measurements on a ship, the water outflow would need to be redesigned so that the motion of the ship would not affect the water height inside the equilibrator.

2.6 Conclusions

We have described an equilibrator with a fast time constant for dissolved oxygen that allows for a sampling flow rate of 3 mL/min. We have also presented a model that describes the equilibration of major gases and shows how changes in pressure, gas composition, and sampling flow rate influence the steady state gas composition in the equilibrator. Using this model, we have determined the corrections needed to account for these influences. The equilibrator, when interfaced with an IsoPrime isotope ratio mass spectrometer, can provide high frequency measurements of dissolved O_2 and its isotopes.

2.7 Acknowledgements

We thank Yann Bozec, for initial work on the mass spectrometer, Adam Cox, for assistance preparing gas cylinders, Todd Martz, for providing the optode, Roberta Hamme, for suggestions on ways to test the equilibrator, and Angeline Ta, for help testing the gas tension device and equilibrator. This material is based upon work supported by the National Science Foundation under Grant No. 0421546.

This chapter, in full, is a reprint of material previously submitted as "An equilibrator to measure dissolved oxygen and its isotopes," by Lauren Elmegreen Rafelski, Bill Paplawsky, and Ralph F. Keeling, to the *Journal of Atmospheric and Oceanic Technology*, 2012. I was the primary investigator and author of this paper.

References

Angert, A., Rachmilevitch, S., Barkan, E., and Luz, B., 2003: Effects of photorespiration, the cytochrome pathway, and the alternative pathway on the triple isotopic composition of atmospheric O_2. *Global Biogeochemical Cycles*, **17**(1), 1030, doi:10.1029/2002GB001933.

Barkan, E., and Luz, B., 2005: High precision measurements of $^{17}O/^{16}O$ and $^{18}O/^{16}O$ ratios in H_2O. *Rapid Communications in Mass Spectrometry*, **19**, 3737–3742.

Bender, M. L., 1990: The $\delta^{18}O$ of dissolved O_2 in seawater: A unique tracer of circulation and respiration in the deep sea. *Journal of Geophysical Research*, **95**(C12), 22243–22252.

Bender, M. L., and Grande, K. D., 1987: Production, respiration, and the isotope geochemistry of O_2 in the upper water column. *Global Biogeochemical Cycles*, **1**(1), 49–59.

Benson, B. B., and Krause, D., Jr., 1980: The concentration and isotopic fractionation of gases dissolved in freshwater in equilibrium with the atmosphere. 1. Oxygen. *Limnology and Oceanography*, **25**(4), 662–671.

Cassar, N., Barnett, B. A., Bender, M. L., Kaiser, J., Hamme, R. C., and Tilbrook, B., 2009: Continuous high-frequency dissolved O_2/Ar measurements by equilibrator inlet mass spectrometry. *Analytical Chemistry*, **81**, 1855–1861.

Copin-Montegut, C., 1985: A method for the continuous determination of the partial pressure of carbon dioxide in the upper ocean. *Marine Chemistry*, **17**, 13–21.

Emerson, S., Stump, C., Wilbur, D., and Quay, P., 1999: Accurate measurement of O_2, N_2 and Ar gases in water and the solubility of N_2. *Marine Chemistry*, **64**, 337–347.

Frankignoulle, M., Borges, A., and Biondo, R., 2001: A new design of equilibrator to monitor carbon dioxide in highly dynamic and turbid environments. *Water Research*, **35**(5), 1344–1347.

Garcia, H. E., and Gordon, L. I., 1992: Oxygen solubility in seawater: Better fitting equations. *Limnology and Oceanography*, **37**(6), 1307–1312.

Guéguen, C., and Tortell, P. D., 2008: High-resolution measurement of Southern Ocean CO_2 and O_2/Ar by membrane inlet mass spectrometry. *Marine Chemistry*, **108**, 184–194.

Hendricks, M. B., Bender, M. L., and Barnett, B. A., 2004: Net and gross O_2 production in the Southern Ocean from measurements of biological O_2 saturation and its triple isotope composition. *Deep-Sea Research I*, **51**, 1541–1561.

Johnson, J. E., 1999: Evaluation of a seawater equilibrator for shipboard analysis of dissolved oceanic trace gases. *Analytica Chimica Acta*, **395**, 119–132.

Juranek, L. W., and Quay, P. D., 2005: In vitro and in situ gross primary and net community production in the North Pacific Subtropical Gyre using labeled and natural abundance isotopes of dissolved O_2. *Global Biogeochemical Cycles*, **19**(GB3009), doi:10.1029/2004GB002384.

Kaiser, J., Reuer, M. K., Barnett, B., and Bender, M. L., 2005: Marine productivity estimates from continuous O_2/Ar ratio measurements by membrane inlet mass spectrometry. *Geophysical Research Letters*, **32**(L19605), doi:10.1029/2005GL023459.

Keeling, R. F., Blaine, T., Paplawsky, B., Katz, L., Atwood, C., and Brockwell, T., 2004: Measurement of changes in atmospheric Ar/N_2 ratio using a rapid-switching, single-capillary mass spectrometer system. *Tellus*, **56B**, 322–338.

Knox, M., Quay, P. D., and Wilbur, D., 1992: Kinetic isotopic fractionation during air-water gas transfer of O_2, N_2, CH_4, and H_2. *Journal of Geophysical Research*, **97**(C12), 20335–20343.

Körtzinger, A., Thomas, H., Schneider, B., Gronau, N., Mintrop, L., and Duinker, J. C., 1996: At-sea intercomparison of two newly designed underway pCO_2 systems - encouraging results. *Marine Chemistry*, **52**, 133–145.

Levine, N. M., Bender, M. L., and Doney, S. C., 2009: The $\delta^{18}O$ of dissolved O_2 as a tracer of mixing and respiration in the mesopelagic ocean. *Global Biogeochemical Cycles*, **23**(GB1006), doi:10.1029/2007GB003162.

Luz, B., and Barkan, E., 2000: Assessment of oceanic productivity with the triple-isotope composition of dissolved oxygen. *Science*, **288**, 2028–2031.

McNeil, C., D'Asaro, E., Johnson, B., and Horn, M., 2006: A gas tension device with response times of minutes. *Journal of Atmospheric and Oceanic Technology*, **23**, 1539–1558.

McNeil, C., Katz, D., Wanninkhof, R., and Johnson, B., 2005: Continuous shipboard sampling of gas tension, oxygen and nitrogen. *Deep-Sea Research I*, **52**, 1767–1785.

Murphy, P. P., Nojiri, Y., Fujinuma, Y., Wong, C. S., Zeng, J., Kimoto, T., and Kimoto, H., 2001: Measurements of surface seawater fCO_2 from volunteer commercial ships: Techniques and experiences from *Skaugran*. *Journal of Atmospheric and Oceanic Technology*, **18**, 1719–1734.

Quay, P. D., Emerson, S., Wilbur, D. O., and Stump, C., 1993: The $\delta^{18}O$ of dissolved O_2 in the surface waters of the Subarctic Pacific: A tracer of biological productivity. *Journal of Geophysical Research*, **98**(C5), 8447–8458.

Quiñones-Rivera, Z. J., Wissel, B., Justić, D., and Fry, B., 2007: Partitioning oxygen sources and sinks in a stratified, eutrophic coastal ecosystem using stable oxygen isotopes. *Marine Ecology Progress Series*, **342**, 69–83.

Reuer, M. K., Barnett, B. A., Bender, M. L., Falkowski, P. G., and Hendricks, M. B., 2007: New estimates of Southern Ocean biological production rates from O_2/Ar ratios and the triple isotope composition of O_2. *Deep-Sea Research I*, **54**, 951–974.

Sarma, V. V. S. S., Abe, O., Hashimoto, S., Hinuma, A., and Saino, T., 2005: Seasonal variations in triple oxygen isotopes and gross oxygen production in the Sagami Bay, central Japan. *Limnology and Oceanography*, **50**(2), 544–552.

Schneider, B., Kremling, K., and Duinker, J. C., 1992: CO_2 partial pressure in Northeast Atlantic and adjacent shelf water: Processes and seasonal variability. *Journal of Marine Systems*, **3**, 453–463.

Schneider, B., Sadkowiak, B., and Wachholz, F., 2007: A new method for continuous measurements of O_2 in surface water in combination with pCO_2 measurements: Implications for gas phase equilibration. *Marine Chemistry*, **103**, 163–171.

Stanley, R. H. R., Kirkpatrick, J. B., Cassar, N., Barnett, B. A., and Bender, M. L., 2010: Net community production and gross primary production rates in the western equatorial Pacific. *Global Biogeochemical Cycles*, **24**(GB4001), doi:10.1029/2009GB003651.

Thiemens, M. H., Jackson, T., Zipf, E. C., Erdman, P. W., and van Egmond, C., 1995: Carbon dioxide and oxygen isotope anomalies in the mesosphere and stratosphere. *Science*, **270**(5238), 969–972.

Tortell, P. D., 2005: Dissolved gas measurements in oceanic waters made by membrane inlet mass spectrometry. *Limnology and Oceanography: Methods*, **3**, 24–37.

Wanninkhof, R., 1992: Relationship between wind speed and gas exchange over the ocean. *Journal of Geophysical Research*, **97**(C5), 7373–7382.

Weiss, R. F., and Price, B. A., 1980: Nitrous oxide solubility in water and seawater. *Marine Chemistry*, **8**, 347–359.

Chapter 3

Mass spectrometer methods for measuring dissolved oxygen isotopes

3.1 Introduction

Bottle samples of dissolved O_2 isotopes have given a general view of the variability in O_2 isotopes around the world, as well as estimates of net and gross primary production (e.g. Hendricks et al., 2004; Juranek and Quay, 2005; Sarma et al., 2005; Reuer et al., 2007; Stanley et al., 2010; Hamme et al., 2012). Continuous measurements of dissolved O_2 isotopes would provide the ability to observe variability at higher temporal or spatial resolution. An equilibrator developed for oxygen and O_2 isotopes, described in Chapter 2, allows for continuous measurements when interfaced with a mass spectrometer. However, there are challenges with the mass spectrometer measurements themselves. For example, many gases can interfere with the measurement of oxygen isotopes. In discrete bottle samples, oxygen and argon gas can be isolated from other potentially contaminating gases. During continuous sampling, isolating oxygen and argon is impractical.

In this chapter, we describe the mass spectrometer methods used to take continuous measurements of dissolved oxygen isotopes. We quantify the interfer-

ences to the oxygen isotopes, describe a method for correcting these interferences, and describe other corrections that are made. These techniques resulted in continuous measurements of oxygen and oxygen isotopes at the Scripps Institution of Oceanography pier from June 22-August 1, 2011.

3.2 Sampling method

An IsoPrime isotope ratio mass spectrometer and counterflow type equilibrator, described in Chapter 2, were used to measure dissolved gases, including dissolved O_2 isotopes, at the Scripps Institution of Oceanography (SIO) pier. The mass spectrometer inlet system allows for a continuous flow of sample and reference gases. A changeover valve switches between the sample and reference gases every 10 seconds. The measurements of the sample and reference gases are used to calculate delta values, defined as:

$$\delta(a/b) = \frac{(a/b)_s}{(a/b)_{ref}} - 1 \tag{3.1}$$

where a and b are two m/z ratios, $(a/b)_s$ is the mean signal of the sample during a 10-second run, and $(a/b)_{ref}$ is the mean of the surrounding 10-second reference runs. The delta values are so small that they are multiplied by 10^3 to give units of per mil, or 10^6 to give units of per meg. For oxygen isotopes, the delta values are expressed as:

$$\delta^x O = \frac{(y/32)_s}{(y/32)_{ref}} - 1 \tag{3.2}$$

where x is 17 or 18, and y is m/z 33 or 34. These delta values can be combined to obtain Δ^{17}O:

$$\Delta^{17} O = \delta^{17} O - \lambda \delta^{18} O \tag{3.3}$$

where λ is the relationship between δ^{17}O and δ^{18}O due to mass-dependent fractionation.

The mass spectrometer calculates delta values using a linearization of Equation 3.1. First, single mass delta values are computed, defined as:

$$\delta(a) = \frac{a_s}{a_{ref}} - 1 \tag{3.4}$$

Then, $\delta(a/b)$ is calculated using:

$$\delta(a/b) = \delta(a) - \delta(b) \tag{3.5}$$

This approximation is valid when $\delta(a/b)$ is small.

A challenge of measuring O_2 isotopes is that their abundances are so low that other gases can interfere with the measurements. One of the strongest interferences is from N_2 gas, which possibly causes interference due to changes in the ionization efficiency. The O_2/N_2 ratio can be highly variable in the ocean, which would change the amount of interference from N_2. Most methods of measuring dissolved oxygen isotopes separate oxygen and argon from nitrogen using gas chromatography to eliminate any interference from N_2 gas (Luz et al., 1999; Blunier et al., 2002). However, when continuously sampling the gas, isolation of O_2 and Ar from other gases is impractical. Therefore, we instead forced the O_2/N_2 ratio to be constant, with the reasoning that if the ratios were the same in the sample and the reference gases, the interference would cancel out.

To keep the O_2/N_2 ratio constant, the mass spectrometer inlet system was modified so that pure N_2 gas could be added to the sample gas upstream of the changeover valve, as shown in Figure 3.1. A tank of pure nitrogen gas was connected to an MKS 640 pressure controller, which controlled the amount of the nitrogen added. The N_2 gas went through a 30 cm long, 0.005" diameter capillary tube and into a "T", with one outlet going into the sample stream, and one line connected to a vacuum. The vacuum allowed for fast changes in the amount of N_2 added, as well as a fast shutoff of the N_2 gas addition. When the nitrogen bleed pressure was set below the sample pressure (500 torr), the nitrogen flow would stop. The vacuum purge would quickly remove the N_2 gas remaining in the capillary line.

During sampling, the pressure of N_2 gas added was determined automatically using measurements of $\delta(32/28)$ and a feedback loop that targeted a $\delta(32/28)$ of zero (i.e. sample O_2/N_2 ratio equal to reference). This only worked when the ambient $\delta(32/28)$ was above zero, but the ambient $\delta(32/28)$ was rarely below zero.

When sampling, we alternated between adding N_2 gas so that oxygen iso-

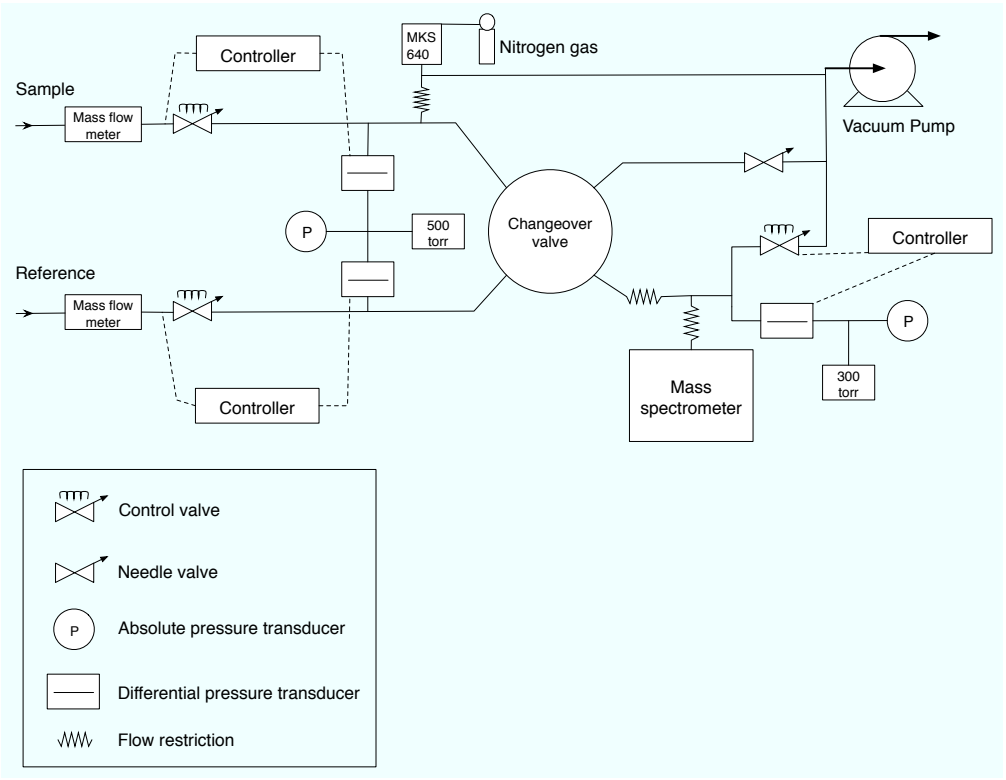

Figure 3.1: Custom mass spectrometer inlet system, with a nitrogen bleed into the sample line.

topes could be measured, and not adding N_2 so that the O_2/N_2 ratio could be measured. The equilibrator sample was run for 20 minutes without N_2 addition, and then 25 minutes with automatic N_2 addition. A "working tank," with composition close to ambient air, was run for 15 minutes every hour or 30 minutes every 2 hours to verify the stability of the reference gas.

Periodically, calibration cylinders with offsets in O_2 or $\delta^{18}O$ were run. The calibration cylinders were run 3 times for 30 minutes, alternating with 30 minute runs of the working tank. The O_2 calibration cylinder was made by mixing pure oxygen gas with air. 23.7 g of 99.9999% pure O_2 gas was added to an empty 5.9 L cylinder. Then, 993.6 g air was added to the cylinder. Using these weights, the final $\delta(O_2/N_2)$ in the cylinder was calculated to be 103.1 per mil.

Making a $\delta^{18}O$-enriched cylinder was less straightfoward, because $^{18}O^{16}O$ gas is not commercially available. Instead, we used $^{18}O^{18}O$ to produce $^{18}O^{16}O$. A 5 L round bottom flask was evacuated to 0.027 torr on a vacuum line. $^{18}O^{18}O$ gas was added to bring the pressure up to 0.123 torr. Then, isotopically normal, pure O_2 gas was added to bring the total pressure to 15.7 torr. To convert the $^{18}O^{18}O$ and $^{16}O^{16}O$ gas to $^{18}O^{16}O$, as tesla coil was used. A tesla coil is a high voltage transformer that operates at radio frequencies, and is commonly used for vacuum leak detection. The tesla coil was applied to the flask for 3-4 minutes, and the isotopic composition was monitored using a quadrupole mass spectrometer. Over time, as the tesla coil was applied, the amount of m/z 34 gas ($^{18}O^{16}O$) increased. After determining how long it took for m/z 34 gas to form, the procedure was repeated without sampling on the quadrupole mass spectrometer. This gas was added to a 29.5 L cylinder, which was then filled to 1150 psig (79 atm) with regular air. The final $\delta^{18}O$-enriched cylinder was run on a Finnegan mass spectrometer to obtain its $\delta^{18}O$ composition, and was found to have an enrichment of 570 per meg.

3.3 Interferences

Several gases have the potential to interfere with the measurement of oxygen isotopes, including N_2, CO_2, water vapor, and dimethyl sulfide (DMS). The

interference from each of these gases was quantified to allow for correction of the mass spectrometer measurements.

3.3.1 Nitrogen

Variations in $\delta(O_2/N_2)$ have been shown to cause interference in oxygen isotopes (Sowers et al., 1989; Abe and Yoshida, 2003). Work on Ar isotopes suggests that this interference is due to changes in the ionization efficiency with the presence of other gases (Severinghaus et al., 2003). We quantified the interference of N_2 on $\delta^{18}O$ and $\delta^{17}O$ using the N_2 bleed system described in Section 3.2.

To determine the interference, N_2 gas was added to sample gas from a cylinder for 30 minutes at a set pressure. The pressure was increased every 30 minutes to add more N_2 gas to the sample. The mean $\delta(33/32)$, $\delta(34/32)$ and $\delta(32/28)$ were computed for each 30-minute run. We assumed that the correction due to N_2 interference (x) was of the form:

$$\delta(X/32)_{corr} = \delta(X/32)_{meas} - x\delta(32/28)_{meas} \tag{3.6}$$

where X is m/z 33 or 34, *corr* is the corrected value, and *meas* is the measured value.

$\delta(33/32)_{meas}$ and $\delta(34/32)_{meas}$ were plotted against $\delta(32/28)_{meas}$, and the slope was found (Figure 3.2), giving an interference, x, of -0.017 $\pm$ 0.002 per meg (per meg change in $\delta(32/28))^{-1}$ for $\delta(33/32)$, and 0.0041 $\pm$ 0.0002 per meg (per meg change in $\delta(32/28))^{-1}$ for $\delta(34/32)$.

The N_2 interference was also quantified during the sampling of equilibrated air by looking at the difference between the times when N_2 was added ("N_2-addition jog"), and the times when N_2 was not added ("no-N_2-addition jog"). As explained in Section 3.2, we alternated between adding N_2 gas to the sample and not adding N_2 gas. The N_2-addition jogs were interpolated to the mean times of the no-N_2-addition jogs, and the difference in $\delta(32/28)$, $\delta(34/32)$, and $\delta(33/32)$ between the N_2-addition jogs and the no-N_2-addition jogs was calculated. The slope of the change in $\delta(33/32)$ or $\delta(34/32)$ versus the change in $\delta(32/28)$ gives the interference (Figure 3.3). Over the course of the timeseries, the correction did not have

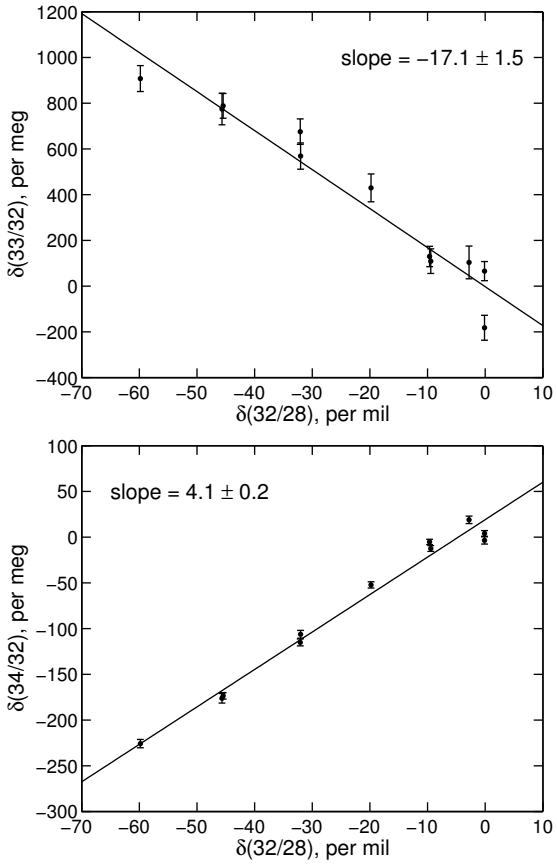

Figure 3.2: Nitrogen interference on $\delta(33/32)$ and $\delta(34/32)$ measured on cylinder air. The slope is divided by 1000 to get the correction, x, in units of per meg/per meg.

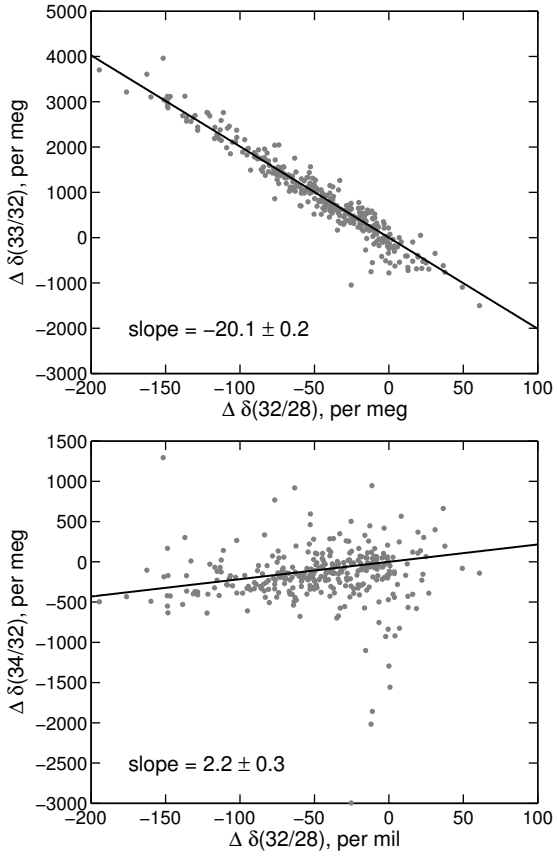

Figure 3.3: Nitrogen interference on $\delta(33/32)$ and $\delta(34/32)$ measured from equilibrated air. $\Delta\delta(32/28)$ is the difference in $\delta(32/28)$ between the no-N_2 addition jog and the interpolated N_2 addition jog. $\Delta\delta(33/32)$ and $\Delta\delta(34/32)$ are defined similarly. The slope is divided by 1000 to get the correction, x, in units of per meg/per meg.

a noticeable drift (not shown). This analysis shows that correction in $\delta(33/32)$ was -0.0201 $\pm$ 0.0002 per meg (per meg change in $\delta(32/28))^{-1}$, and the mean correction in $\delta(34/32)$ was 0.0022 $\pm$ 0.0003 per meg (per meg change in $\delta(32/28))^{-1}$ (Table 3.1). We use these values to correct for the N_2 interference.

3.3.2 Carbon dioxide

Carbon dioxide has been shown to interfere with measurements of $\delta(O_2/N_2)$ and $\delta(Ar/N_2)$ from the formation of CO^+, which is present at m/z 28 (Keeling et al., 2004). In addition, there is the potential for CO_2 to interfere with the mea-

Table 3.1: Interference in $\delta(33/32)$ and $\delta(34/32)$ from N_2 and CO_2, in units of per meg (per meg)$^{-1}$.

δ value	N_2 interference (cylinder)	N_2 interference (equilibrator)	CO_2 interference
$\delta(33/32)$	-0.0171 ± 0.0015	-0.0201 ± 0.0002	(2.1 ± 0.4)x10^{-4}
$\delta(34/32)$	0.0041 ± 0.0002	0.0022 ± 0.0003	(7.2 ± 0.4)x10^{-5}

surement of oxygen isotopes, such as through changes in the ionization efficiency or swapping of oxygen atoms between CO_2 and O_2. The interference from CO_2 can be quantified either by adding CO_2 to the sample stream, as with the N_2 interference measurement, or by removing CO_2 from the sample stream, and we tested both methods. However, the isotopic composition of the oxygen in the added CO_2 was unknown, and therefore the interference from oxygen atom swapping may have been different with this CO_2 gas than with ambient CO_2. Therefore, we chose to use CO_2 removal to quantify the interferences.

CO_2 was removed from a sample stream of gas using a glass trap filled with ascarite II (2/3 of trap) followed by magnesium perchlorate (1/3 of trap) to remove any water produced by the reaction of CO_2 with the ascarite II. The ascarite trap was switched in or out of the sample line every 90 minutes. The sample was run for two 90 minute jogs with the ascarite trap, and two 90 minute jogs without the ascarite trap. $\delta(33/32)$, $\delta(34/32)$, $\delta(32/28)$, $\delta(32/40)$ and $\delta(40/28)$ of these jogs were plotted against $\delta(44/28)$. The slope gives the CO_2 interference, defined as:

$$\delta(X/Y)_{corr} = \delta(X/Y)_{meas} - x\delta(44/28)_{meas} \tag{3.7}$$

The interferences in $\delta(33/32)$ and $\delta(34/32)$ are given in Table 3.1. The interference in $\delta(40/28)$ was -4.3x10^{-5} ± 0.5x10^{-5} per meg (per meg)$^{-1}$. The interferences in $\delta(32/28)$ and $\delta(32/40)$ were less well constrained in this test, at 5.9x10^{-5} ± 7.7x10^{-5} per meg (per meg)$^{-1}$ and 1.0x10^{-4} ± 7.2x10^{-5} per meg (per meg)$^{-1}$, respectively. Work by Blaine (2005) suggests that $\delta(40/28)$ and $\delta(32/28)$ should have similar interferences to each other, which Blaine measured as -6.3x10^{-5} per meg (per meg)$^{-1}$ and -6.2x10^{-5} per meg (per meg)$^{-1}$, respectively. These interference are so small for our observed values of dissolved $\delta(40/28)$, $\delta(32/28)$, and $\delta(32/40)$ that the interference due to CO_2 can be ignored for these measurements.

However, we correct for the CO_2 interference on oxygen isotopes.

3.3.3 Water vapor

Water vapor has the potential to cause interference through the protonation of other ions. Water has been shown to interfere with the measurement of CO_2 isotopes through the production of HCO_2^+ (Leckrone and Hayes, 1998). Similarly, water could interfere with the measurement of $\Delta^{17}O$ through the production of HO_2^+ at m/z 33. During sampling, most of the water vapor is removed from the equilibrated air using a trap in a -55^{o}C chiller. However, $^{17}O^{16}O$ has such a low abundance that even small amounts of HO_2^+ could have a measurable effect on m/z 33.

To quantify the effect of water vapor on $\Delta^{17}O$, we added water vapor to the sample in a range of amounts. A trap (16.5 cm long, 1/4" diameter stainless steel tube, filled with 3 mm glass beads) was placed in a -55^{o}C chiller and room air was run through the trap overnight at 3 mL/min to precondition it with water vapor. After this preconditioning, a cylinder of air was attached to the inlet of the trap, and the temperature of the chiller was set to 0, -1, -3, -5, -10, -15 or -55^{o}C. As the cylinder air flowed through the trap, water vapor would enter the air stream. The gas then went directly to the mass spectrometer inlet system. To measure the water content, the mass spectrometer was tuned to measure m/z 18 with the m/z 30 collector, and the sample was run until the time-averaged m/z 18 signal stabilized. The single-mass delta value of m/z 18 ($\delta(18)$, defined in Equation 3.4) was multiplied by the mean m/z 18 signal, in fA, to compute the difference in the amount of water vapor between the sample and reference gases. Then, the tuning was reverted to standard tuning to measure m/z 32, 33, and 34 in order to calculate $\Delta^{17}O$. Although we could not simultaneously measure $\Delta^{17}O$ and $\delta(18)$, we could measure both quantities with the same valve switching and the same water content.

The amplitude of the interference was modulated in the setup by changing the trap temperature, which influences the amount of water added to the sample. The results are shown Figure 3.4. For higher m/z 18 amplitudes (i.e. higher chiller

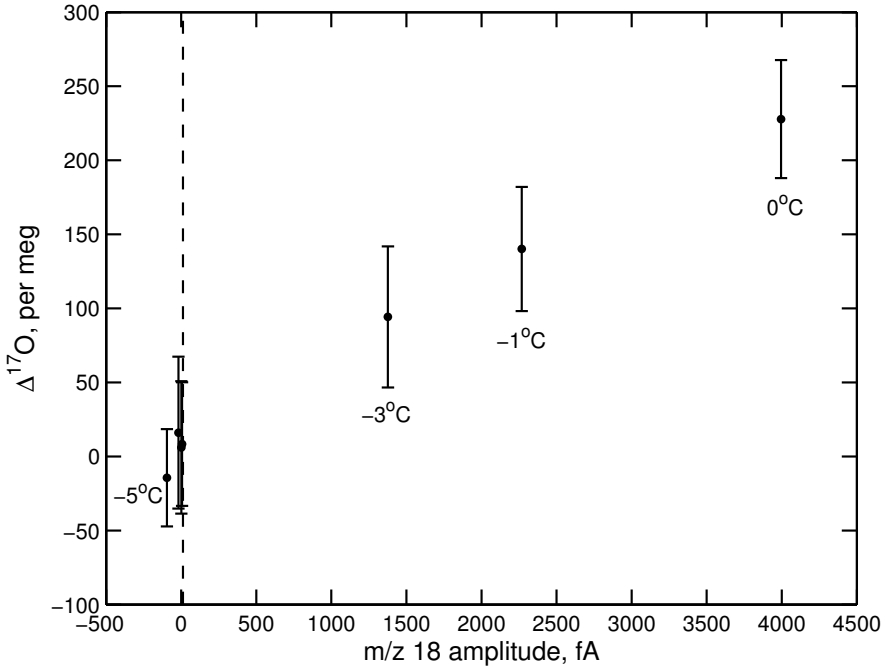

Figure 3.4: Interference in $\Delta^{17}O$ from water vapor. The error bars are the standard error of the mean $\Delta^{17}O$. The m/z 18 amplitude is calculated using $\delta(18)$, as described in the text. The dashed vertical line is the m/z 18 amplitude (12.2 fA) of equilibrated air run through a trap in a -55^{o}C chiller.

temperatures), there is a noticeable interference in $\Delta^{17}O$. Below -10^{o}C, the m/z 18 amplitude is near zero, and there is no significant change in $\Delta^{17}O$ with trap temperature. The equilibrator temperature used during sampling (-55^{o}C) is well below this -10^{o}C threshold. Furthermore, the m/z 18 amplitude of equilibrated air was measured to be 12.2 fA using the -55^{o}C chiller (dashed line on Figure 3.4). This amplitude falls within the range of points that are insensitive to temperature changes. From these tests, we can conclude that water vapor does not cause a measurable interference in $\Delta^{17}O$ at a chiller temperature of -55^{o}C.

In Figure 3.4, the water content measured by the m/z 18 amplitude drops off more quickly than would be expected from the change in temperature alone. This effect is consistent with a temperature-dependent lag in the arrival of the water vapor relative to the other molecules in the sample. This would cause water vapor to affect both the sample and standard gases, causing an underestimate in

the magnitude of the interference on $\Delta^{17}O$. The raw m/z 18 signal, in fA, showed a sine-wave-like variation as the changeover valve switched between the reference gas and the sample gas every 10 seconds, and a phase shift relative to the valve position, which varied with the temperature of the sample (Figure 3.5). Further analysis shows that the phase shift is directly related to the amount of water vapor in the sample. At high water concentrations (0^oC) there was no lag, and at lower concentrations, the lag increases non-linearly (Figure 3.6). A possible explanation for this is that water vapor is "sticky" and takes longer to move through the lines than the other molecules in the air. If there is only a small amount of water vapor in the sample, the water will be delayed entering the mass spectrometer. If there is a lot of water vapor, then the inside surfaces of the tubing would become coated with water, so the remaining water vapor would enter the mass spectrometer with the rest of the sample gas. This lag caused the water vapor to be out of phase with the rest of the sample. For tests at -5^{o}C and -10^{o}C, the shift is approaching half a cycle, so there would have been more water vapor in the mass spectrometer when the reference gas was measured than when the sample gas was measured. This accounts for the negative m/z 18 amplitudes shown in Figure 3.4.

3.3.4 Dimethyl Sulfide

Sulfur compounds also have the potential to interfere with the measurement of $\Delta^{17}O$, through isobaric interference at m/z 32 (S^+), 33 (HS^+) and 34 (H_2S^+). The biggest source of volatile sulfur in the ocean is dimethyl sulfide (DMS) (Cline and Bates, 1983). To test the interference of DMS on $\Delta^{17}O$, we made a 29.5 L cylinder spiked with DMS. This cylinder was prepared by injecting 4 μL DMS through a septum into air flowing from a cylinder of gas into an evacuated cylinder, and then bringing the pressure of the target cylinder up to around 600 psig (42 atm) with air, yielding a cylinder with 1.1 ppm DMS. The isotopic composition of oxygen in this cylinder was measured with and without first removing the DMS. We used a glass trap filled with gold wire to remove DMS from the cylinder air, which is a technique commonly used for measurements of DMS (e.g. Andreae et al., 1983). $\Delta^{17}O$ of the gas in the tank was -7.8 $\pm$ 10.7 per meg with DMS present,

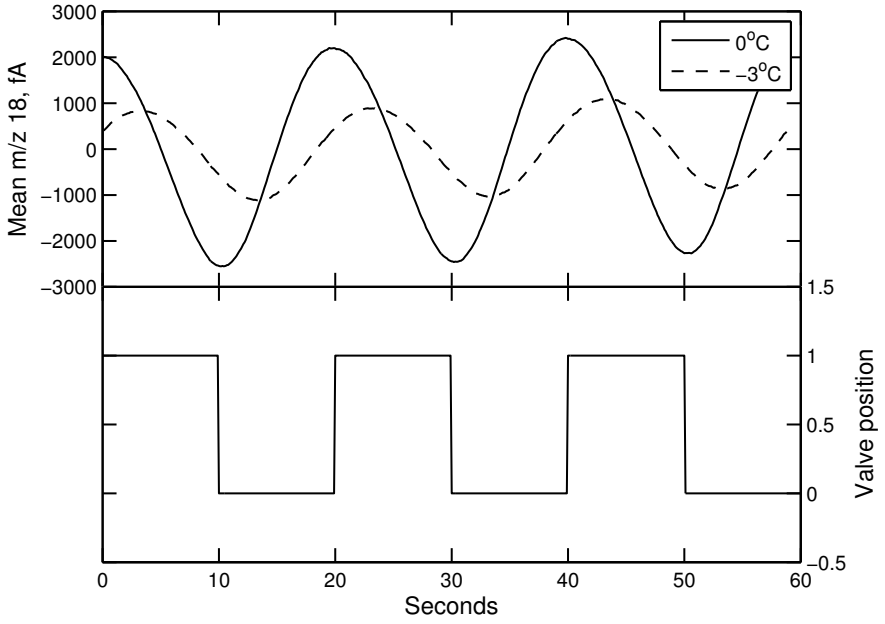

Figure 3.5: Top: 60 seconds of m/z 18 data, with the mean subtracted, at 0^{o}C and -3^{o}C. Bottom: Timing of switching between reference and sample gases.

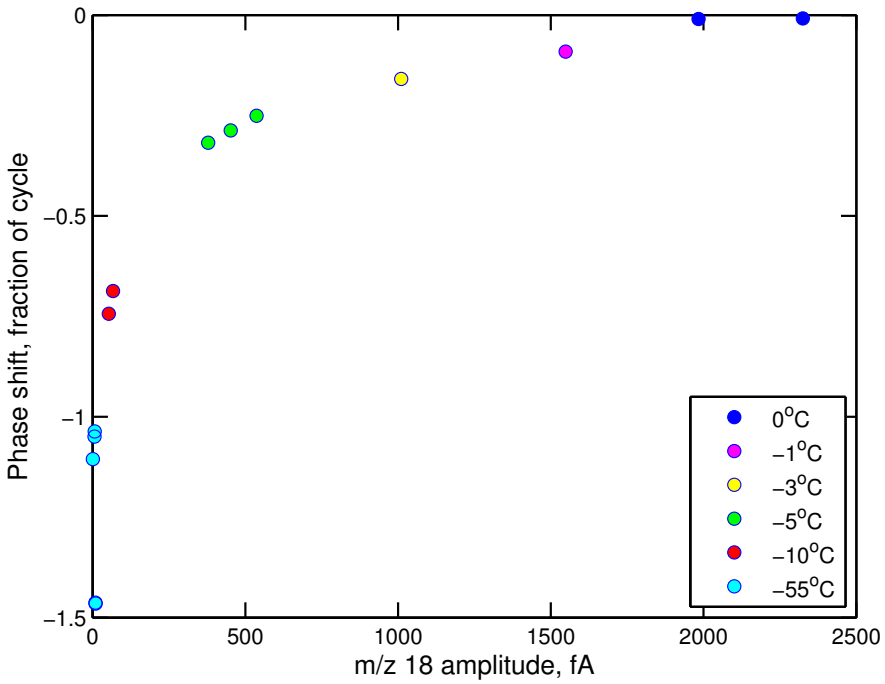

Figure 3.6: Phase shift of m/z 18 signal relative to the timing of the changeover valve switching, versus the amplitude of the m/z 18 signal.

and 19.3 ± 13.2 per meg with DMS removed. The lower $\Delta^{17}O$ value when the gas contained DMS could be due to interference at m/z 32, m/z 34, or both.

In the ocean at the SIO pier, the concentration of DMS is around 5 nM (Eric Saltzman, personal communication). The Henry's law coefficient for DMS at 18^{o}C is 0.069 (Wong and Wang, 1997). Using these values, the concentration of DMS in air equilibrated with the water is expected to be around 8 ppb. Since 1.1 ppm DMS causes a change in $\Delta^{17}O$ of 27.1 per meg, 8 ppb of DMS would only contribute an offset of around 0.2 per meg, which is far below the precision of the $\Delta^{17}O$ measurement. Therefore, we conclude that DMS does not cause a measurable interference in $\Delta^{17}O$.

3.4 Corrections to data

Several levels of calibration had to be applied to the oxygen and oxygen isotope measurements to account for interferences and the scale contraction of the mass spectrometer. The $\delta^{18}O$ signal was computed from the raw mass spectrometer signals via:

$$\delta^{18}O = d_{18} \times c_{18} \times (\delta(34/32) - a_{18} \times \delta(32/28) - b_{18} \times \delta(44/28)) \tag{3.8}$$

where a_{18} is the correction factor for nitrogen interference, b_{18} is the correction factor for CO_2 interference, c_{18} is the span correction, and d_{18} is the zero correction of the mass spectrometer. The same equation applies to $\delta^{17}O$, with different correction values (a_{17}, b_{17}, c_{17}, and d_{17}).

$\delta(O_2/N_2)$, $\delta(Ar/N_2)$, and $\delta(O_2/Ar)$ are similarly computed with expressions of the form:

$$\delta(X/Y) = d_{x/y} \times c_{x/y} \times \delta(X/Y) \tag{3.9}$$

where $d_{x/y}$ and $c_{x/y}$ are defined as in Equation 3.8.

Values of a and b are based on the experiments described in Section 3.3, and are shown in Table 3.1. For a, we use the correction determined from equilibrated air, rather than the correction based on the cylinder data.

The span correction (c) accounts for effects that lead to scale contraction, including incomplete switching at the changeover valve. We determined the span of the instrument using calibration tanks with a high concentration of oxygen or δ^{18}O. We measured the difference between the calibration tank and the surrounding working tank runs, as described in Section 3.2. The ratio between the actual composition of the tanks, measured as described in Section 3.2, and the composition measured on this mass spectrometer is the span correction, c. For $\delta(O_2/N_2)$, c_{O_2/N_2} is 1.20, and for δ^{18}O, c_{18} is 1.18. We also use c_{O_2/N_2} for $\delta(Ar/N_2)$ and $\delta(O_2/Ar)$, and c_{18} for δ^{17}O.

The zero correction, d, was made because when the mass spectrometer inlet is closed, and there is no gas in the mass spectrometer, the collectors do not read 0 fA. Therefore, a zero offset needs to be subtracted from the raw values of the signal for a given m/z. For a single mass delta value, defined in Equation 3.4, the correction is straightforward:

$$\delta(X)_{corr} = \frac{X_{ref}}{X_{ref} - X_0}\delta(X) \tag{3.10}$$

where X is m/z 28, 32, 33, 34, or 40, and X_0 is the signal with the mass spectrometer inlet closed.

The correction to delta values relating two m/z ratios (e.g. $\delta(O_2/N_2)$, δ^{18}O) is more complicated. The correction for small delta values would be:

$$\delta(X/Y)_{corr} = \frac{X_{ref}}{X_{ref} - X_0}\delta(X) - \frac{Y_{ref}}{Y_{ref} - Y_0}\delta(Y) \tag{3.11}$$

where X is m/z 32, 33, 34, or 40, and Y is m/z 32 for δ^{18}O or δ^{17}O, m/z 28 for $\delta(O_2/N_2)$ or $\delta(Ar/N_2)$, and m/z 40 for $\delta(O_2/Ar)$. It would be more useful to be able to apply a correction directly to $\delta(X/Y)$, rather than to the single mass delta values. Fortunately, there are approximations that make this possible.

For δ^{18}O and δ^{17}O, the nitrogen correction, explained above, gives values of δ^{18}O and δ^{17}O as if $\delta(32)$ were zero. Equation 3.11 becomes:

$$\delta^x O_{corr} = \frac{X_{ref}}{X_{ref} - X_0}(\delta(X) - \delta(32)) = \frac{X_{ref}}{X_{ref} - X_0}\delta^x O \tag{3.12}$$

where x is 17 or 18, and X is m/z 33 or 34.

For $\delta(O_2/N_2)$, $\delta(Ar/N_2)$, and $\delta(O_2/Ar)$ the single mass delta values corrections ($\frac{X_{ref}}{X_{ref}-X_0}$) are very similar for 28, 32, and 40: 1.0184 for 28, 1.0159 for 32, and 1.0195 for 40. Therefore, the corrected values can be approximated using a mean value:

$$\delta(X/Y)_{corr} = 1.0179 \times \delta(X/Y) \tag{3.13}$$

where X is m/z 32 or 40 and Y is m/z 28 or 40. Using this approximation instead of the exact form of the correction introduces an error of less than 1%.

The corrections presented here apply to any sample measured on this mass spectrometer. However, when measuring equilibrated air, the sample gas may also differ from true equilibration with dissolved gas due to the finite equilibration rate of the equilibrator. Corrections to account for incomplete equilibration are presented in Chapter 2.

3.5 Conclusions

We present a method of taking continuous mass spectrometer measurements of dissolved oxygen isotopes. Continuous measurements of dissolved gases introduce interferences that may not be present in bottle samples. However, these interferences can be quantified and corrected. We described a method of adding N_2 gas to keep the O_2/N_2 ratio constant, rather than removing N_2 gas from the sample. We also quantified interferences due to N_2, CO_2, water vapor, and DMS, finding that only N_2 and CO_2 had significant interferences. Finally, we described the corrections made to measurements of $\delta(O_2/N_2)$, $\delta(Ar/N_2)$, $\delta(O_2/Ar)$, $\delta^{18}O$, and $\delta^{17}O$ to account for N_2 and CO_2 interferences, the span of the mass spectrometer, and the zero offset of the mass spectrometer.

3.6 Acknowledgements

We thank Adam Cox for assistance with cylinder preparation, Daniel Baggenstos for measuring the δ^{18}O-enriched cylinder on the Finnegan mass spectrometer, and Eric Saltzman, for helpful discussions about DMS measurements.

This chapter, in part, is being prepared for publication. Lauren Elmegreen Rafelski, Bill Paplawsky, and Ralph F. Keeling. I am the primary investigator and author of this paper.

References

Abe, O., and Yoshida, N., 2003: Partial pressure dependency of $^{17}O/^{16}O$ and $^{18}O/^{16}O$ of molecular oxygen in the mass spectrometer. *Rapid Communications in Mass Spectrometry*, **17**, 395–400.

Andreae, M. O., Barnard, W. R., and Ammons, J. M., 1983: The biological production of dimethylsulfide in the ocean and its role in the global atmospheric sulfur budget. *Ecological Bulletins*, **35**, 167–177.

Blaine, T. W., 2005: *Continuous measurements of atmospheric Ar/N_2 as a tracer of air-sea heat flux: Models, methods, and data*. Ph.D. thesis, University of California, San Diego.

Blunier, T., Barnett, B., Bender, M. L., and Hendricks, M. B., 2002: Biological oxygen productivity during the last 60,000 years from triple oxygen isotope measurements. *Global Biogeochemical Cycles*, **16**(3), 1029, 10.1029/2001GB001460.

Cline, J. D., and Bates, T. S., 1983: Dimethyl sulfide in the equatorial Pacific Ocean: A natural source of sulfur to the atmosphere. *Geophysical Research Letters*, **10**(10), 949–952.

Hamme, R. C., Cassar, N., Lance, V. P., Vaillancourt, R. D., Bender, M. L., Strutton, P. G., Moore, T. S., DeGrandpre, M. D., Sabine, C. L., Ho, D. T., and Hargreaves, B. R., 2012: Dissolved O_2/Ar and other methods reveal rapid changes in productivity during a Lagrangian experiment in the Southern Ocean. *Journal of Geophysical Research*, **117**(C00F12), doi:10.1029/2011JC007046.

Hendricks, M. B., Bender, M. L., and Barnett, B. A., 2004: Net and gross O_2 production in the southern ocean from measurements of biological O_2 saturation and its triple isotope composition. *Deep-Sea Research I*, **51**, 1541–1561.

Juranek, L. W., and Quay, P. D., 2005: In vitro and in situ gross primary and net community production in the North Pacific Subtropical Gyre using labeled and natural abundance isotopes of dissolved O_2. *Global Biogeochemical Cycles*, **19**(GB3009), doi:10.1029/2004GB002384.

Keeling, R. F., Blaine, T., Paplawsky, B., Katz, L., Atwood, C., and Brockwell, T., 2004: Measurement of changes in atmospheric Ar/N_2 ratio using a rapid-switching, single-capillary mass spectrometer system. *Tellus*, **56B**, 322–338.

Leckrone, K. J., and Hayes, J. M., 1998: Water-induced errors in continuous-flow carbon isotope ratio mass spectrometry. *Analytical Chemistry*, **70**, 2737–2744.

Luz, B., Barkan, E., Bender, M. L., Thiemens, M. H., and Boering, K. A., 1999: Triple-isotope composition of atmospheric oxygen as a tracer of biosphere productivity. *Nature*, **400**, 547–550.

Reuer, M. K., Barnett, B. A., Bender, M. L., Falkowski, P. G., and Hendricks, M. B., 2007: New estimates of Southern Ocean biological production rates from O_2/Ar ratios and the triple isotope composition of O_2. *Deep-Sea Research I*, **54**, 951–974.

Sarma, V. V. S. S., Abe, O., Hashimoto, S., Hinuma, A., and Saino, T., 2005: Seasonal variations in triple oxygen isotopes and gross oxygen production in the Sagami Bay, central Japan. *Limnology and Oceanography*, **50**(2), 544–552.

Severinghaus, J. P., Grachev, A., Luz, B., and Caillon, N., 2003: A method for precise measurement of argon 40/36 and krypton/argon ratios in trapped air in polar ice with applications to past firn thickness and abrupt climate change in Greenland and Siple Dome, Antarctica. *Geochimica et Cosmochimica Acta*, **67**(3), 325–343.

Sowers, T., Bender, M., and Raynaud, D., 1989: Elemental and isotopic composition of occluded O_2 and N_2 in polar ice. *Journal of Geophysical Research*, **94**(D4), 5137–5150.

Stanley, R. H. R., Kirkpatrick, J. B., Cassar, N., Barnett, B. A., and Bender, M. L., 2010: Net community production and gross primary production rates in the western equatorial Pacific. *Global Biogeochemical Cycles*, **24**(GB4001), doi:10.1029/2009GB003651.

Wong, P. K., and Wang, Y. H., 1997: Determination of the Henry's Law constant for dimethyl sulfide in seawater. *Chemosphere*, **35**(3), 535–544.

Chapter 4

Measurements of O_2 and $\delta^{18}O$ in the Southern California coastal ocean

4.1 Introduction

Oceanic primary production is an important part of the global carbon cycle, with net primary production totaling around 50 GtC yr^{-1} (Westberry et al., 2008). Primary production can be measured using a variety of methods, including bottle incubations that measure ^{14}C uptake, which gives a measurement between gross and net primary production, and bottle incubations that measure ^{18}O production (Bender et al., 1999). In addition, satellite measurements of chlorophyll concentration in the surface ocean are used to measure global primary production (e.g. Antoine et al., 1996).

Measurements of dissolved gases, including O_2 and $\delta^{18}O$ of O_2, can also provide information about primary production. $\delta^{18}O$ is defined as:

$$\delta^{18}O = \frac{(^{18}O/^{16}O)_s}{(^{18}O/^{16}O)_r} - 1 \tag{4.1}$$

where the subscripts s and r stand for sample and reference values, and $\delta^{18}O$ is multiplied by 1000 to give units of per mil. Photosynthesis and respiration influence both dissolved O_2 and $\delta^{18}O$. Photosynthesis increases O_2 and decreases

$\delta^{18}O$, because photosynthesis produces O_2 with an isotopic composition similar to oxygen in water (Guy et al., 1993), which has more ^{16}O relative to ^{18}O than atmospheric O_2 (Kroopnick and Craig, 1972). Respiration decreases O_2 and increases $\delta^{18}O$, because respiration preferentially uses ^{16}O over ^{18}O, an effect known as fractionation (Lane and Dole, 1956).

Measurements of dissolved O_2 and $\delta^{18}O$ have been used to determine rates of photosynthesis and respiration. Bender and Grande (1987) showed that the relationship between $\delta^{18}O$ and O_2 saturation is determined by the ratio of photosynthesis to respiration. Since then, measurements of $\delta^{18}O$ and O_2 saturation have been used with models that include photosynthesis, respiration, and air-sea gas exchange (Venkiteswaran et al., 2007; Quiñones-Rivera et al., 2007, 2009), as well as more complex models that also include advection and diffusion (Quay et al., 1993; Levine et al., 2009). As most of these studies note, the ability to determine productivity from O_2 and $\delta^{18}O$ is limited by the uncertainty in the fractionation factor of respiration.

Previous studies have measured $\delta^{18}O$ of dissolved O_2 by taking bottle samples of water for later gas extraction and analysis on a mass spectrometer. Because of the amount of work involved in taking a single measurement, there are limitations in the timescales of the processes that can be measured. To allow for more frequent measurements over a longer period of time than previous work, we developed a system for continuous, real-time measurement of dissolved gases using an equilibrator designed for oxygen equilibration, and a mass spectrometer. To test this method, we collected data at the Scripps Institution of Oceanography (SIO) pier, in La Jolla, California. The SIO pier is located at 32^o 52.52'N, 117^o 15.30' W, and its proximity to CalCOFI (California Cooperative Oceanic Fisheries Investigations) stations allows our results to be put into the context of ongoing research in the Southern California Bight.

We measured dissolved O_2 and $\delta^{18}O$ at the SIO pier over a period of 5 weeks, and obtained observations at hourly resolution. We present this data, along with a model of O_2 and $\delta^{18}O$ that includes photosynthesis, respiration, air-sea gas exchange and mixing. We use this model to determine processes contributing to

the observed variability in O_2 and $\delta^{18}O$.

4.2 Methods

Measurements of dissolved gases were taken at the Scripps Institution of Oceanography (SIO) pier from June 22-August 1, 2011. Detailed descriptions of the instruments and sampling methods are presented in Chapters 2 and 3. Briefly, a counterflow-type equilibrator with fast equilibration of oxygen and oxygen isotopes was interfaced with an isotope ratio mass spectrometer. Water was pumped from a depth of 2 m below mean lower low water level (MLLW) into the equilibrator, where dissolved gas exchanged with headspace gas on the surfaces of bubbles, Raschig rings, and water droplets. The total gas tension of seawater was measured using a Liquicel MicroModule Membrane Contactor interfaced to a pressure transducer. Gas circulated through the equilibrator in a pressure-controlled loop, which set the equilibrator headspace pressure to match the observed but variable total gas tension. Gas was added to the loop from a "makeup" cylinder, or removed to a vacuum, to keep the pressure constant. Gas was sampled from the equilibrator loop at a flow rate of 3 mL min^{-1}.

Because variations in the O_2/N_2 ratio have been shown to interfere with $\delta^{18}O$ measurements (e.g. Abe and Yoshida, 2003), we added N_2 to the sample gas stream to maintain a constant O_2/N_2 ratio. We alternated between adding N_2 to the sample stream for 25 minutes to remove N_2 interference, and not adding N_2 for 20 minutes so that the O_2/N_2 ratio could be measured.

Periodically, the flow rate of the makeup gas to the loop would spike to very high values because of pressure fluctuations due to the water flow stopping and starting as a strainer cleaned out. Data within 30 minutes after a spike were removed, and remaining data were averaged into two points per hour - one for the data with N_2 added, and one for the data without N_2 added. The data were corrected for N_2 and CO_2 interferences, for mass spectrometer scale contraction due to incomplete switching between the sample and reference gases, for the collector background currents, and for incomplete equilibration, as described in Chapters 2

and 3.

On this mass spectrometer, when a cylinder of gas is sampled, the standard error of the mean of 20 minutes of data is 0.8 per meg for $\delta(O_2/N_2)$, 4.5 per meg for $\delta^{18}O$, and 1.1 per meg for $\delta(Ar/N_2)$. As will be shown in Section 4.4, we observed large variability in O_2 and $\delta^{18}O$. However, given the precision of the mass spectrometer, it would be possible to detect much smaller signals.

Dissolved oxygen concentration was measured using an Aanderaa optode, as explained in Chapter 2. The optode measures O_2 concentration and water temperature, and uses the solubility relationship of Garcia and Gordon (1992) to compute percent oxygen saturation. The optode has an internal calibration that defines 100% oxygen saturation and 0% oxygen saturation. In addition, Winkler titrations were taken periodically to independently measure dissolved oxygen concentration. The Winkler titration results were on average 2.9 $\pm$ 5.3 μM (1.2%) above the optode readings. We multiplied the optode data by 1.012 to match the optode data to the Winkler titrations.

Changes in dissolved oxygen saturation can be due to physical processes (such as water temperature changes), or biological processes (photosynthesis and respiration). Craig and Hayward (1987) showed that, because Ar and O_2 have similar responses to physical processes, but Ar is not affected by biological processes, the saturation of Ar can be used to remove the physical component of the O_2 saturation. We use the biological oxygen saturation, as defined by Hendricks et al. (2004) and Luz and Barkan (2009), which uses mass spectrometer measurements of O_2 and Ar to determine the biological component of O_2 saturation. We compute the biological oxygen saturation, $\%O_{2(bio)}$, using:

$$\%O_{2(bio)} = \frac{(O_2/Ar)_{sam}}{(O_2/Ar)_{eq}} = \frac{\delta(O_2/Ar)_{sam} + 1}{\delta(O_2/Ar)_{eq} + 1} \tag{4.2}$$

where $\delta(O_2/Ar)$ is defined similarly to $\delta^{18}O$:

$$\delta(O_2/Ar) = \frac{(O_2/Ar)_s}{(O_2/Ar)_r} - 1 \tag{4.3}$$

and is multiplied by 1000 to get units of per mil. $\delta(O_2/Ar)_{sam}$ is the sampled $\delta(O_2/Ar)$, and $\delta(O_2/Ar)_{eq}$ is the value in equilibrium with the atmosphere. Because

we measure gases in an equilibrated headspace, rather than while they are still dissolved, $\delta(O_2/Ar)_{eq}$ is equal to the atmospheric value of $\delta(O_2/Ar)$. Because our reference gas is very close to atmospheric concentration, $\delta(O_2/Ar)_{eq}$ is close to zero.

We then convert this biological saturation to concentration units:

$$\Delta[O_2]_{bio} = (\%O_{2(bio)} - 1)[O_2]_{sat} \tag{4.4}$$

where $[O_2]_{sat}$ is the saturation concentration of O_2 at the measured temperature and salinity, calculated using the equations in Weiss (1970). By this definition, a positive value of $\Delta[O_2]_{bio}$ means that biological processes have added O_2 to the water (i.e. net photosynthesis) and a negative value of $\Delta[O_2]_{bio}$ means that biological processes have removed O_2 from the water (i.e. net respiration).

We similarly express the optode measurements in terms of the deviation from saturation:

$$\Delta[O_2]_{opt} = (\%O_{2(opt)} - 1)\frac{[O_2]_{opt}}{\%O_{2(opt)}} \tag{4.5}$$

where $\%O_{2(opt)}$ and $[O_2]_{opt}$ are measured by the optode. Note that $\Delta[O_2]_{opt}$ is not just the biological contribution, because the percent saturation given by the optode includes physical and biological components.

Measurements of water temperature, salinity, chlorophyll, and water pressure at depth were obtained from the Southern California Coastal Ocean Observing System (SCCOOS), which has a station at the SIO pier at 5 m depth (MLLW). Chlorophyll data were corrected using surface chlorophyll concentration measurements from the SCCOOS Harmful Algal Bloom program, which measures chlorophyll concentration every few days by extracting chlorophyll from bottle samples. The 5 m depth chlorophyll data were multiplied by 2.15 to bring the values into agreement with the surface measurements. Measurements of photosynthetically active radiation (PAR) and wind speed at the pier were obtained from the SIO pier weather station. Temperature profiles were measured using 9 temperature sensors mounted to a pier piling (a "temperature chain"), with vertical resolution of approximately 1 m (provided by Eric Terrill, Coastal Observing R&D Center, Scripps Institution of Oceanography).

4.3 O_2 and $\delta^{18}O$ model

Simple models of biological O_2 saturation and $\delta^{18}O$ can be used to determine rates of primary productivity. Models used in previous research have ranged in complexity from box models that include only photosynthesis, respiration and air-sea gas exchange (Venkiteswaran et al., 2007; Quiñones-Rivera et al., 2007, 2009), to more complex models that also add advection and diffusion terms (Quay et al., 1993; Levine et al., 2009). We use a one-box model that includes photosynthesis, respiration, air-sea gas exchange, and mixing (Figure 4.1). The time rate of change of O_2 is:

$$h\frac{dC}{dt} = P - R + k(C_{sat} - C) + M(C_m - C) \tag{4.6}$$

where h is the box depth, C is the oxygen concentration, P is photosynthesis, R is respiration, k is the gas exchange coefficient, M is the mixing rate, C_{sat} is the oxygen concentration at saturation, and C_m is the oxygen concentration of water mixing into the box. C_{sat} is determined from the mean water temperature and salinity using the equations in Weiss (1970). P, R, M, and C_m are free parameters. We define k using the following wind-speed parameterization (Wanninkhof, 1992):

$$k = 0.31u^2 \left(\frac{Sc}{660}\right)^{-1/2} \tag{4.7}$$

where u is the mean wind speed measured at the pier (2.47 m s^{-1}), and Sc is the Schmidt number for oxygen, computed from (Wanninkhof, 1992):

$$Sc = 1953.4 - 128T + 3.9918T^2 - 0.050091T^3 \tag{4.8}$$

where T is water temperature.

Similarly, the equation describing the evolution of $\delta^{18}O$ is:

$$h\frac{d}{dt}(CX) = PX_w\alpha_p - RX\alpha_r + k\alpha_k(C_{sat}X_{sat} - CX) + M(C_mX_m - CX) \tag{4.9}$$

Equation 4.6 can be combined with Equation 4.9 to solve for dX/dt. X is the ratio of $^{18}O^{16}O$ to $^{16}O^{16}O$, and can be substituted with $(1+\delta^{18}O/1000)$, where $\delta^{18}O$ is in units of per mil. The subscripts w, sat, and m represent the isotopic composition of oxygen in H_2O, at saturation with air, and in the mixing endmember, respectively.

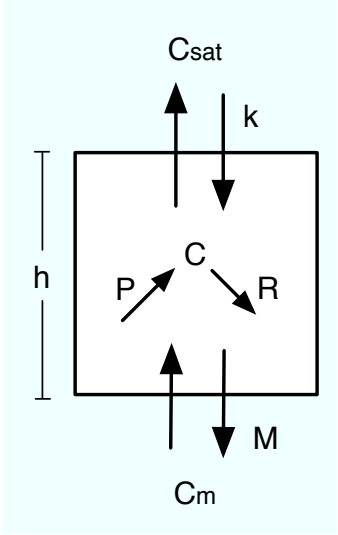

Figure 4.1: One-box model of biological O_2 concentration. This model includes photosynthesis (P), respiration (R), air-sea gas exchange (k), and mixing (M). The model for δ^{18}O has the same fluxes, but also includes fractionation terms.

We use atmospheric O_2 as the reference value for δ^{18}O. δ^{18}O of SMOW relative to atmospheric O_2 is -22.96 per mil (Hendricks et al., 2004), assuming that δ^{18}O of the atmosphere relative to SMOW is 23.5 per mil (Kroopnick and Craig, 1972). Measurements of the isotopic composition of oxygen in H_2O at the SIO pier give a mean value of -0.5 per mil on the SMOW scale (Chun-Ta Lai and Lisa Welp, personal communication). This makes $\delta^{18}O_w$ at our sampling site equal to -23.46 per mil. $\delta^{18}O_{sat}$ is 0.73039 per mil at the mean measured water temperature of 19.24^{o}C (Benson and Krause, 1980). $\delta^{18}O_m$, the δ^{18}O of the mixing endmember, is a free parameter and is fit using the δ^{18}O data. α_p, α_r, and α_k are the fractionation factors of photosynthesis, respiration and kinetic gas exchange, respectively. Because of uncertainties in α_p and α_r, these parameters are varied as explained in Section 4.5. α_k is 0.9972 (Knox et al., 1992).

These equations are used in a forward model with diurnally varying photosynthesis. Studies have shown that photosynthesis rates are a function of irradiance (e.g. Platt and Jassby, 1976; Marra et al., 1985). Photosynthesis will increase with irradiance until a saturation level is reached, then will either stabilize or decrease (photoinhibition) with increasing irradiance. We use the measured

photosynthetically active radiation (PAR) to model the photosynthesis. In the absence of measurements of the photosynthesis-to-irradiance relationship at the pier during sampling, we choose a saturation level of 500 μmol photons $m^{-2}s^{-1}$, which is within the range of observed values (e.g. Gilstad et al., 1993; Meyercordt et al., 1999; Yoshie et al., 2010), and we assume that there is no photoinhibition. Therefore, P is modeled as:

$$P = \begin{cases} xPAR & \text{if PAR } <500 \ \mu\text{mol photons } m^{-2}s^{-1} \\ 500x = P_{500} & \text{if PAR } >=500 \ \mu\text{mol photons } m^{-2}s^{-1}. \end{cases} \tag{4.10}$$

From the model results, $\delta^{18}O$ is computed from X. $\delta^{18}O_{sat}$ is subtracted from the computed $\delta^{18}O$ because our measured O_2 is in equilibrium with dissolved O_2, and therefore offset from dissolved $\delta^{18}O$ by the equilibrium fractionation.

4.4 Experimental results

4.4.1 Timeseries of O_2 and $\delta^{18}O$

The timeseries of dissolved gases at the SIO pier, from June 22-August 1, 2011, are shown in Figure 4.2. All times are in Pacific Standard Time (PST). Gaps in the timeseries are due to removal of data after spikes in the makeup gas flow (shorter gaps), or instrument maintenance (longer gaps). Biological O_2 was supersaturated for most of the record, with concentrations as high as 55 mmol m^{-3} (125% saturation), but during the first week of data, there are days when biological O_2 drops as low as -18 mmol m^{-3} (92% saturation). $\delta^{18}O$ values are nearly all negative relative to atmospheric values, which is consistent with enhanced O_2 due to photosynthesis.

There is strong variation in biological O_2 concentration and $\delta^{18}O$ on daily and longer timescales (Figure 4.3). Biological O_2 concentration is generally highest between 15:00 and 21:00 hr, and lowest between 6:00 and 9:00 hr. $\delta^{18}O$ variability shows similar timing, with the lowest values in the evening and highest values in the morning. Like biological O_2, chlorophyll concentration shows a maximum in late afternoon. These daily variations in biological properties do not show strong

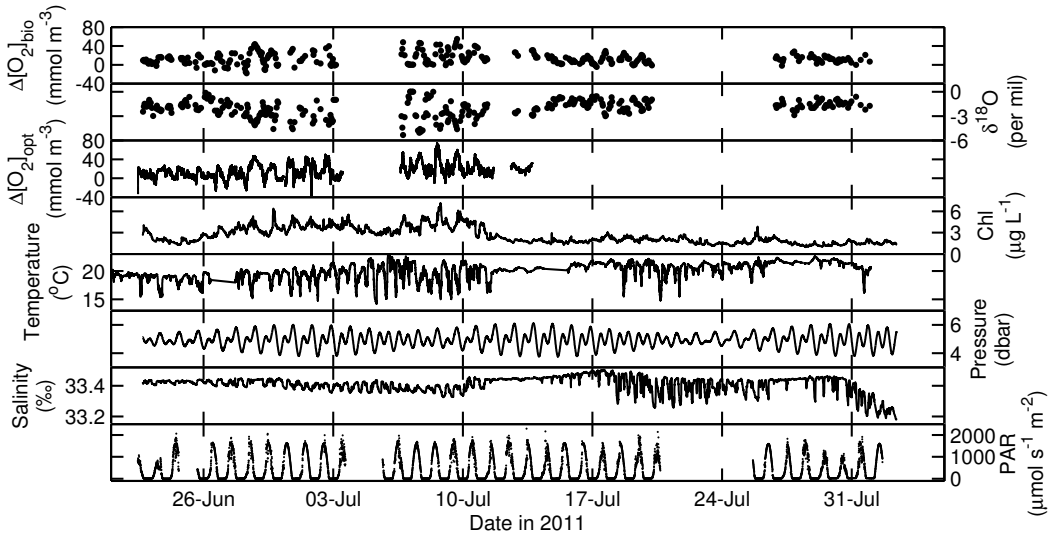

Figure 4.2: Data from the SIO pier. Biological O_2 concentration ($\Delta[O_2]_{bio}$) and $\delta^{18}O$ were measured using the mass spectrometer. $\Delta[O_2]_{opt}$ was measured using the optode. Chlorophyll, pressure, and salinity are from the SIO pier SCCOOS station, at 5 m depth. Chlorophyll concentration is corrected using surface bottle measurements, as described in the text. Temperature was interpolated to 2 m depth from the temperature chain data. Photosynthetically active radiation (PAR) is from the SIO pier weather station.

relationships with variations in physical properties, such as pressure (a measure of the tidal cycle), salinity, or water temperature. The late afternoon temperature minimum seen in the first part of the record does coincide with the timing of the O_2 and chlorophyll maxima, but the early morning temperature minimum does not have a corresponding maximum in O_2 or chlorophyll.

In addition to daily variations, there is a "regime change" that can be seen in the biological O_2 concentration, $\delta^{18}O$, chlorophyll concentration, salinity and water temperature, starting July 12. Before July 12, biological O_2 concentration and $\delta^{18}O$ show higher variability than after, and chlorophyll concentrations were higher. Salinity and temperature (including the temperature profile, Figure 4.4) also show higher variability before July 12, with a stable period for several days afterwards. The daily variations in temperature and salinity are consistent with internal tides bringing in sub-thermocline water.

The regime change can be understood by considering the nutrient input. Although we did not measure nutrients at the pier, water temperature can be used to estimate nitrate content. Water temperatures below 14.5^{o}C have been shown to have measurable nitrate concentrations in the Southern California Bight (Lucas et al., 2011). Recent work has suggested that internal tides bring nitrate into the nearshore region (Lucas et al., 2011). From June 22-July 12, temperatures below 14.5^{o}C are seen at depth, so we can conclude that nitrate was added to the water column during this time. The stability of the water temperature after July 12 could have been caused by a deepening of the thermocline. During this period, internal tides were not advecting colder water, and as a consequence, nitrate would not have been added to the water column. Therefore, it seems that before July 12, internal tides brought in cold water with nutrients, which promoted production and enhanced biological O_2 concentration and chlorophyll concentration. When the thermocline deepened, fewer nutrients were available, production decreased, and biological O_2 concentration and chlorophyll concentration decreased.

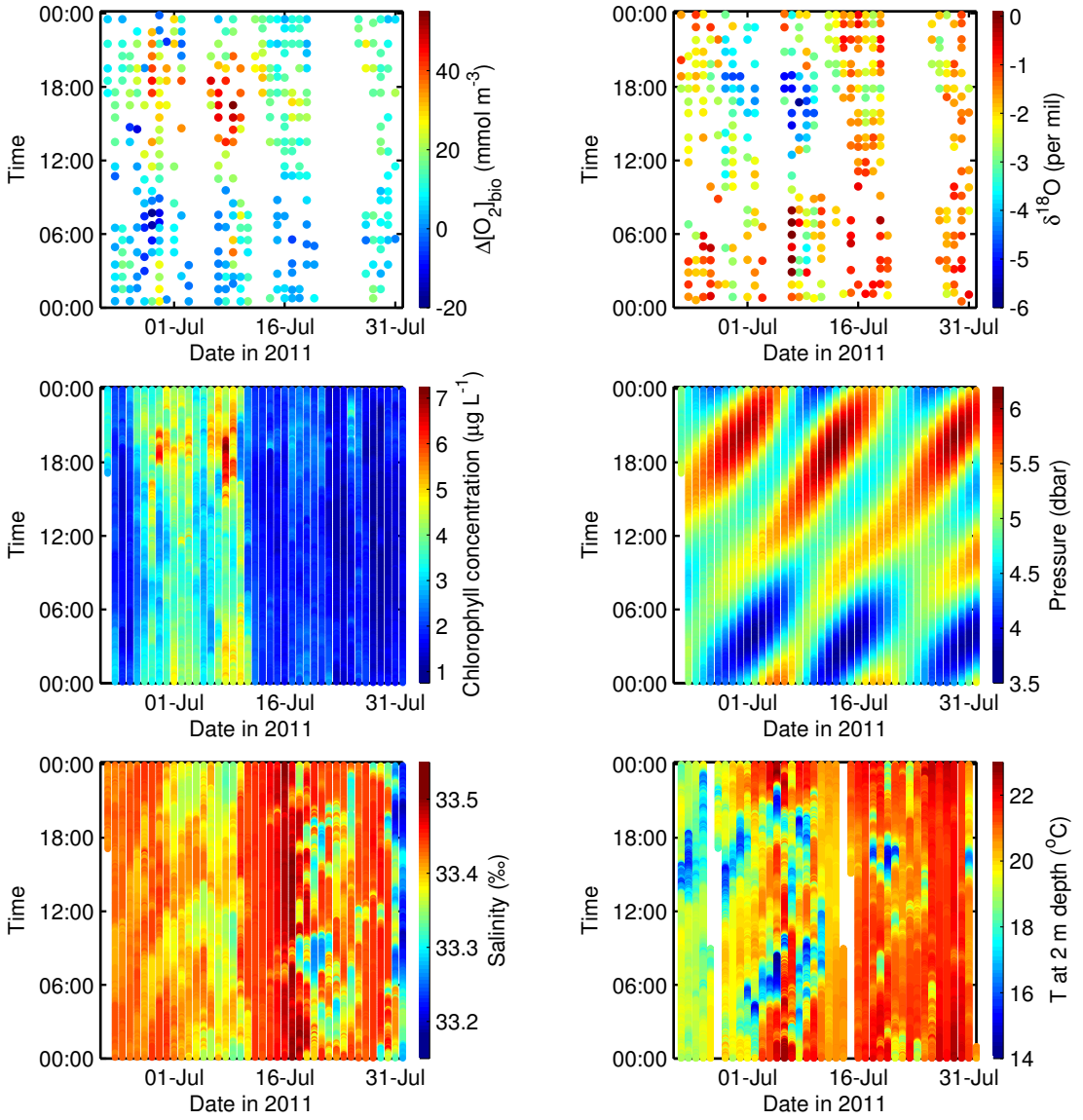

Figure 4.3: Data from Figure 4.2, shown as a function of time and date. Biological O_2 concentration and $\delta^{18}O$ were measured using the mass spectrometer. Chlorophyll concentration, pressure, and salinity are from the SIO pier SCCOOS station, at 5 m depth, and water temperature was interpolated to 2 m depth from temperature chain profile data.

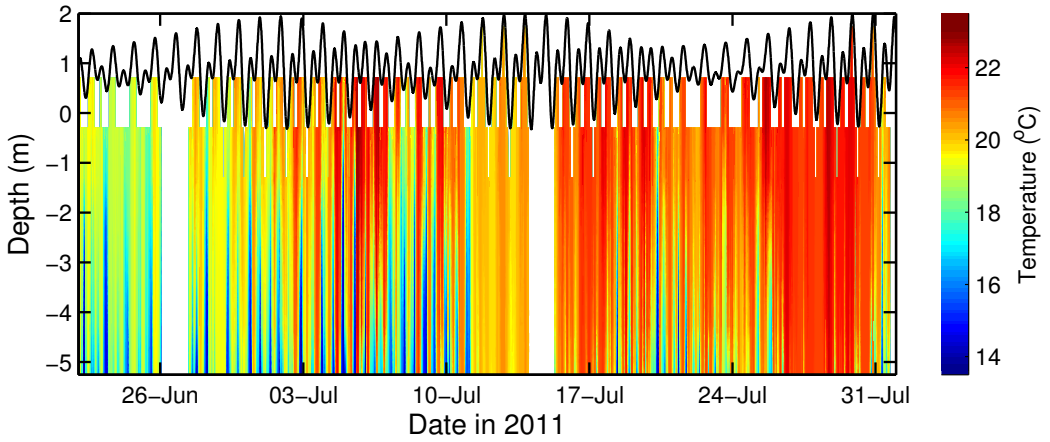

Figure 4.4: Temperature profile, with depth relative to MLLW. The water level (from the NOAA La Jolla, CA station) is shown in black. When the water height was lower than a sensor on the temperature chain, the temperature at that sensor is not shown.

4.4.2 Observed diurnal cycle

The timeseries data show diurnal variability in biological O_2 concentration and $\delta^{18}O$. To assess whether there were other significant frequencies of variability, we used the Lomb-Scargle periodogram technique, a frequency analysis method for unevenly spaced data (Lomb, 1976; Scargle, 1982). The results, shown in Figure 4.5, show a strong peak at a frequency of 1/day, supporting the presence of a regular diurnal cycle, and no peaks at higher frequencies, which suggests that advective processes, such as tidal variations, contribute little to O_2 variability. To better visualize the diurnal variability, the data were bin-averaged by hour of the day to compute a mean diurnal cycle. The resulting mean diurnal cycles are shown in Figure 4.6, along with the standard error in the mean. Biological O_2 concentration, $\delta^{18}O$, and chlorophyll concentration show strong diurnal cycles, with amplitudes that are much larger than the standard error of the mean. The amplitude of the biological O_2 concentration cycle, calculated using the mean values from 4:30-7:30 and 16:30-19:30, is 19 mmol m^{-3}, which agrees well with the amplitude of the O_2 concentration measured by the optode, 22 mmol m^{-3}. The amplitude of the $\delta^{18}O$ cycle, calculated using the mean values from 4:30-7:30 and

16:30-19:30, is 1.1 per mil. As noted above, the cycle in $\delta^{18}O$ is inverted relative to the cycle in O_2. Both cycles show rapid changes in the early morning and late afternoon, and a more stable period during the night.

The amplitude of the O_2 cycle can be used to estimate a lower bound on the photosynthesis rate. A rise in biological O_2 concentration of 19 mmol m^{-3} over 12 hours suggests a minimum mean photosynthesis rate of 1.6 mmol O_2 m^{-3} hr^{-1} during the day, in the limiting case where there are no processes causing a draw-down of oxygen during the day. The presence of processes that decrease biological O_2 concentration during the day, such as respiration, mixing, and air-sea gas exchange, would mean that the photosynthesis rate must be greater than this lower bound to account for the amplitude of the cycle. For example, if the processes that decrease biological oxygen concentration are constant over 24 hours, this would offset 50% of the rise, and the mean photosynthesis rate during the day would be doubled to 3.2 mmol O_2 m^{-3} hr^{-1}.

The peak in biological O_2 concentration is shifted from the peak in PAR by around 6 hours. This is consistent with observations of dissolved O_2 in the Chesapeake Bay (Sanford et al., 1990), where a 6 hour lag between PAR and dissolved oxygen maxima was also observed. Because PAR is correlated with instantaneous production, and biological O_2 concentration gives a measure of production integrated over time, this lag is consistent with photosynthesis causing the observed cycle in O_2. The mean salinity does not show daily variability that matches the timing of the O_2 variability.

4.4.3 Observed relationship between biological O_2 concentration and $\delta^{18}O$

As shown in the timeseries and mean diurnal cycles, variations in oxygen and $\delta^{18}O$ are inversely related. Studies of oxygen concentration and $\delta^{18}O$ with depth have shown that as oxygen concentration decreases, $\delta^{18}O$ increases, due to fractionation during respiration (Kroopnick and Craig, 1976; Bender and Grande, 1987; Quay et al., 1993). Similarly, as O_2 increases due to photosynthesis, $\delta^{18}O$ is expected to decrease. In Figure 4.7, data from the SIO pier is shown along with

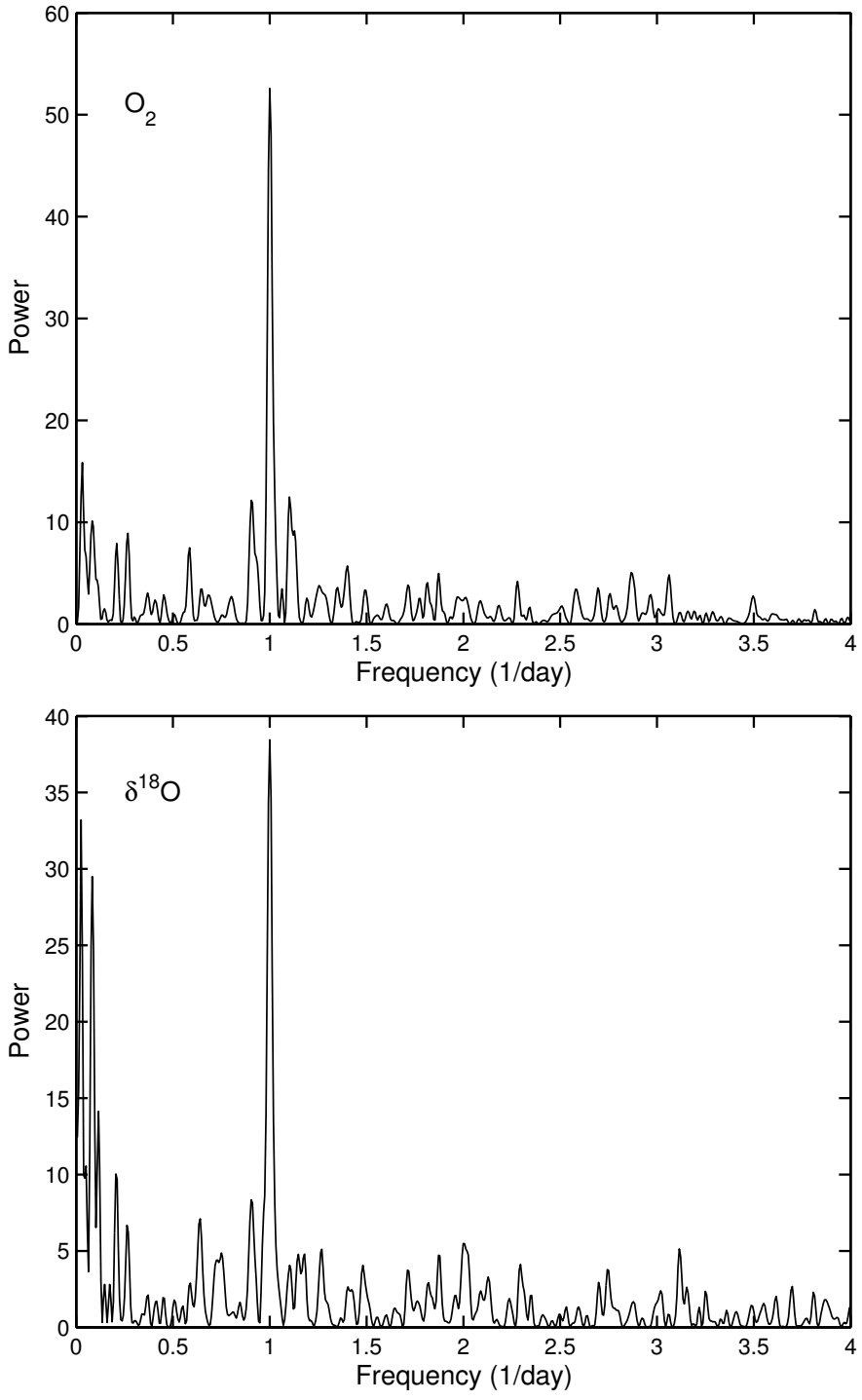

Figure 4.5: Periodogram of O_2 (top) and $\delta^{18}O$ (bottom), calculated using the Lomb-Scargle method.

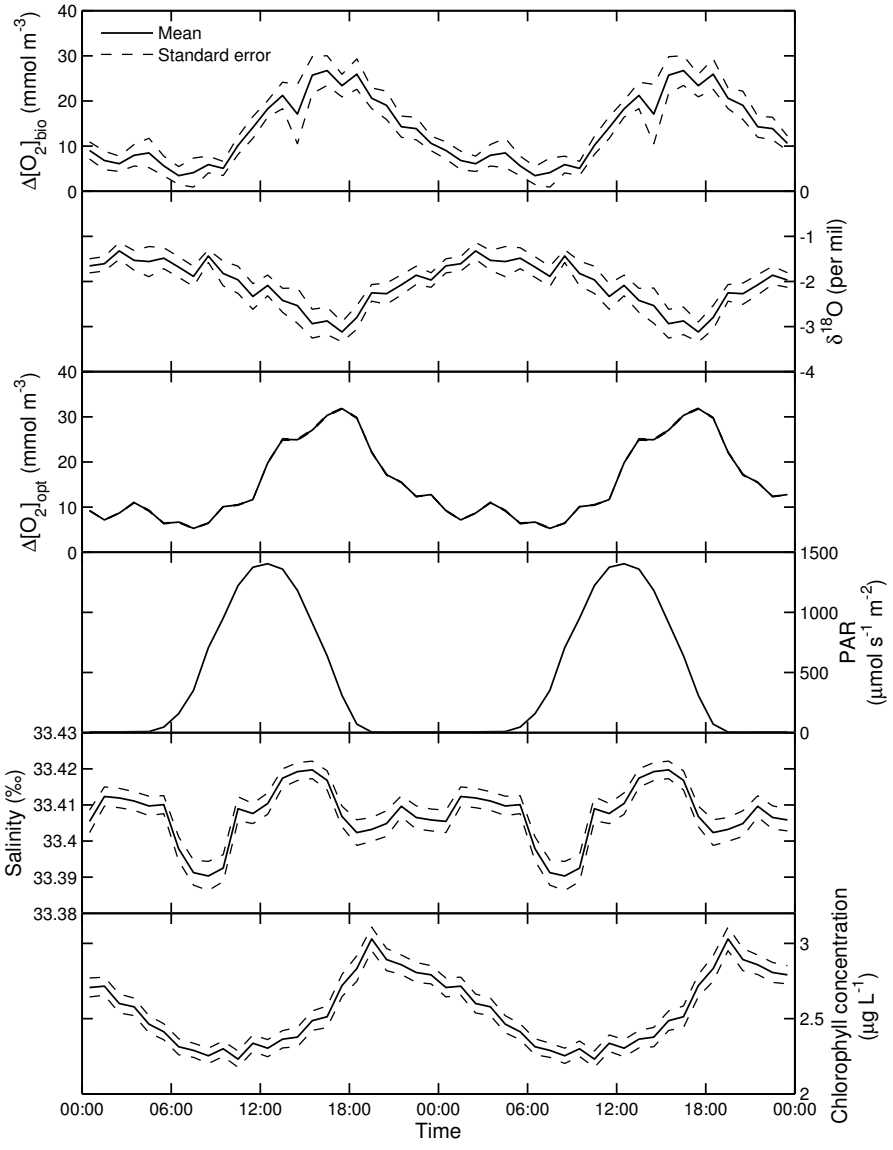

Figure 4.6: Mean diurnal cycle in biological O_2 concentration, $\delta^{18}O$, O_2 concentration measured by the optode, PAR, salinity, and chlorophyll concentration. The same 24-hour period is shown twice.

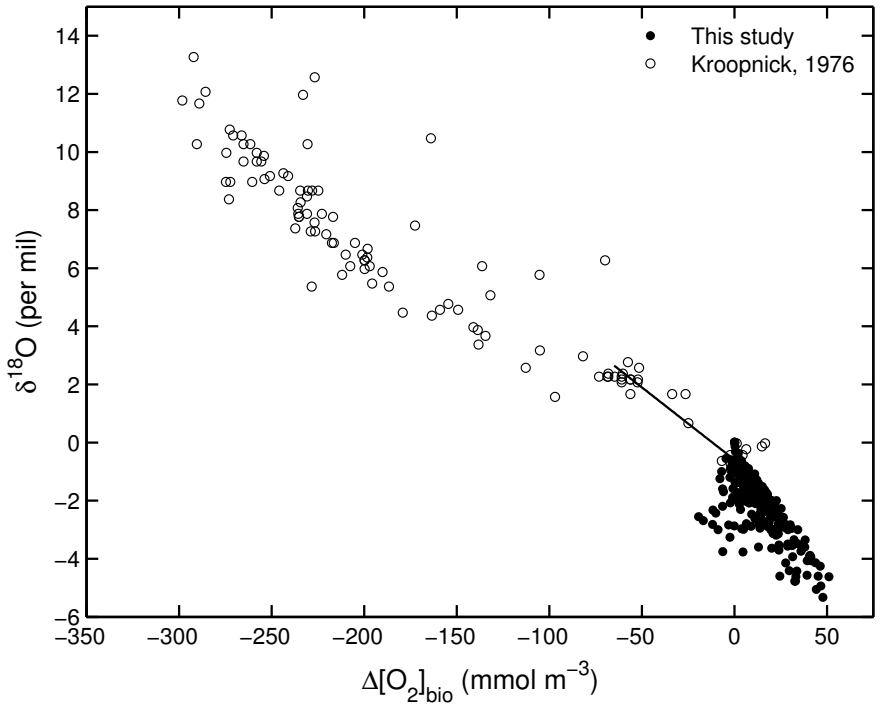

Figure 4.7: Data from this study shown with data from Kroopnick and Craig (1976). Kroopnick and Craig values were converted to mmol m^{-3} using their reported values of percent saturation and oxygen concentration, using Equation 4.5. The isotopic composition of dissolved oxygen in equilibrium with the atmosphere (0.73039 per mil) was subtracted from the Kroopnick and Craig data to put it on the same scale as our data. The line is a fit to the Kroopnick and Craig data that fall between -65 and 0 mmol m^{-3}.

data from Kroopnick and Craig (1976), which includes samples from the Southern Ocean, South Pacific, Equatorial Pacific, North Pacific, and North Atlantic. The data from Kroopnick and Craig (1976) fall along a relatively tight line, whereas our data have a sharp upper limit, but fan out below the line.

The features of our data are shown more clearly in Figure 4.8, where the water temperature is shown in color. Colder water has lower $\delta^{18}O$ values for a given biological O_2 concentration, and warmer water tends to fall along the upper line. The coldest water shows negative biological O_2 concentrations without the corresponding increase in $\delta^{18}O$ that might be expected from the Kroopnick and Craig data. For comparison, the 24 points corresponding to the hourly values of

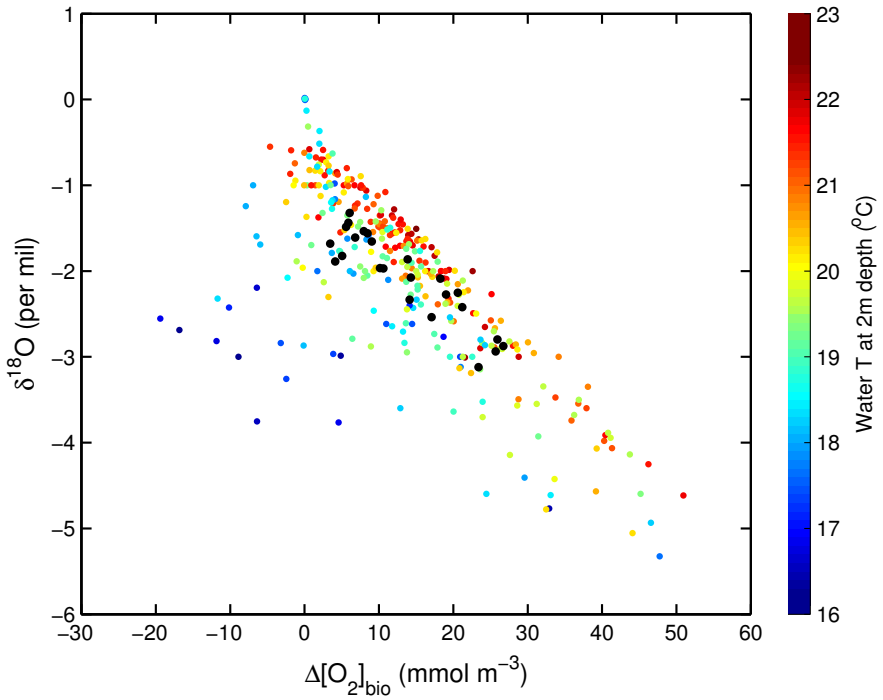

Figure 4.8: Relationship between biological O_2 concentration and $\delta^{18}O$. The color of the point corresponds to the water temperature when that data point was taken. The mean diurnal cycle is shown in black.

the mean diurnal cycle are shown in black.

The timeseries shown in Figure 4.2 can be split into three general regimes: Regime I: June 22 to July 3, where the variability is high and there are periods of negative biological O_2 concentration; Regime II: July 6 to July 11, where the variability is high and biological O_2 concentration is always positive; and Regime III: July 13 to August 1, where the variability is lower, chlorophyll concentrations are lower, and nutrient supply was likely lower. The mean diurnal cycle was computed for each of these subsets of data to see the variations in the diurnal cycle. Although the cycles are noisier because there is less data in each subset, each period has unique features that help describe variations in $\delta^{18}O$ and biological O_2 concentration (Figure 4.9). Regime I has a lower slope than the overall mean diurnal cycle, with values going into "colder water" points. There is also some curvature to the data. Regime II falls along the main line of the data, with values

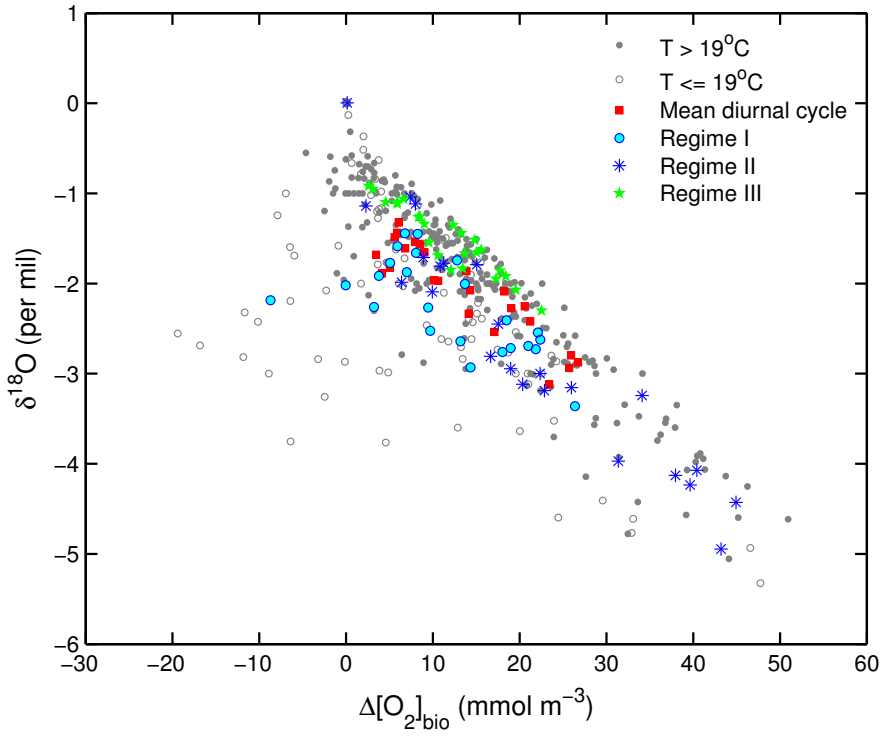

Figure 4.9: Relationship between biological O_2 concentration and $\delta^{18}O$. The data have been sorted based on water temperature, with 19^oC as the cutoff. The mean diurnal cycle for each regime, as explained in the text, is shown, along with the overall mean diurnal cycle.

approaching the maximum observed biological O_2 concentration. Regime III has lower biological O_2 concentrations, with higher $\delta^{18}O$ values than the overall mean diurnal cycle.

4.5 Model results

4.5.1 Modeled diurnal cycle

We used a diurnal cycle model, described in Section 4.3, to determine the forcings on biological O_2 concentration and $\delta^{18}O$ that contribute to the observed mean diurnal cycles. The model has several free parameters, as outlined in Table 4.1. The modeled photosynthesis rate varies over a 24-hour period, because of

its dependence on PAR. As shown in Equation 4.10, P at any time during the day can be determined if PAR and P_{500}, the maximum daily photosynthesis rate, are known. Therefore, we use P_{500} as a free parameter. In the model, the respiration rate is replaced with the photosynthesis to respiration ratio, $\bar{P}/R$, where $\bar{P}$ is the mean photosynthesis rate over 24 hours. We assume that the respiration rate is constant (except for a special case, discussed below) and that the mixing rate is constant. We used a Levenberg-Marquardt algorithm to find the combination of parameters that best fit the observed mean diurnal cycle in biological O_2 concentration. Because there are so many free parameters, there are many combinations of parameters that describe the data. Table 4.1 gives results from several cases. In some cases (1-4, 9, and 10), most parameters were fit to O_2 and then, using these parameters, $\delta^{18}O_m$ was found through a fit to $\delta^{18}O$. In other cases (5-8), we used the opposite strategy, where most parameters were fit to $\delta^{18}O$, and then C_m was fit using O_2.

To reduce the number of free parameters, we defined a few parameters in each case. Wind speed was set to the mean observed value, 2.47 m s^{-1}. Because the box depth itself is a less-important parameter for us to constrain, we chose to set the box depth at 2.5 m, just below our pump intake. For cases where O_2 was fit first, we set C_m to a low, medium, or high concentration. CalCOFI data from August 2011 (Figure 4.10) show that water is supersaturated down to around 25 m depth, with supersaturations ranging from 101-112%. Here we report results using C_m (in units of deviation from saturation) of 0 mmol m^{-3} (100%), 7.1 mmol m^{-3} (103%) and 14.2 mmol m^{-3} (106%) (Cases 1-3). Using a C_m higher than 106% resulted in a P/R of less than 1, which is inconsistent with the observed supersaturation in O_2.

With these model constraints, the box can be thought of as a diurnal surface layer, which mixes with the water above the thermocline. Diurnal surface layers form from solar heating, which causes daily stratification of the upper few meters of water, followed by mixing with the water below as the surface cools at night (e.g. Lynn and Svejkovsky, 1984). Although the mean diurnal cycle in the temperature profile at the pier is complicated by advective processes, which do not influence the

Table 4.1: Best-fit parameters for various cases. Bolded numbers were set for that run, and non-bolded numbers were fit.

Variable	Case 1	Case 2	Case 3	Case 4	Case 5	Case 6	Case 7	Case 8	Case 9[a]	Case 10[b]
h (m)	**2.5**	**2.5**	**2.5**	**2.5**	**2.5**	**2.5**	**2.5**	**2.5**	**2.5**	**2.5**
M (m day^{-1})	6.92	6.86	6.84	6.86	9.83	10.50	10.30	10.64	6.92	4.77
P_{500} (mmol O_2 m^{-3} hr^{-1})	4.73	4.73	4.72	4.73	4.68	4.54	4.45	3.74	4.13	**2.98**
P/R	4.44	1.64	1.01	1.64	19.53	2.10	1.01	1.94	1.82	1.84
C_m[c](mmol m^{-3})	**0**	**7.1**	**14.2**	**7.1**	1.9	8.0	13.9	9.4	**7.1**	**7.1**
$\delta^{18}O_m$ (per mil)	-0.42	-1.02	-1.58	-0.83	**-0.5**	**-1.0**	**-1.5**	**-1.0**	-1.00	-1.03
α_r	**0.9803**	**0.9803**	**0.9803**	**0.978**	**0.9803**	**0.9803**	**0.9803**	**0.978**	**0.9803**	**0.9803**
α_p	**1.004**	**1.004**	**1.004**	**1**	**1.004**	**1.004**	**1.004**	**1**	**1.004**	**1.004**
u (m s^{-1})	**2.47**	**2.47**	**2.47**	**2.47**	**2.47**	**2.47**	**2.47**	**2.47**	**2.47**	**2.47**
Data used for fit	O_2	O_2	O_2	O_2	$\delta^{18}O$	$\delta^{18}O$	$\delta^{18}O$	$\delta^{18}O$	O_2	O_2

[a] Respiration rates were twice as high at night as during the day.

[b] P_{500} was set to the photosynthesis rate based on the assimilation number.

[c] Expressed as the deviation from saturation, $\Delta[O_2]$.

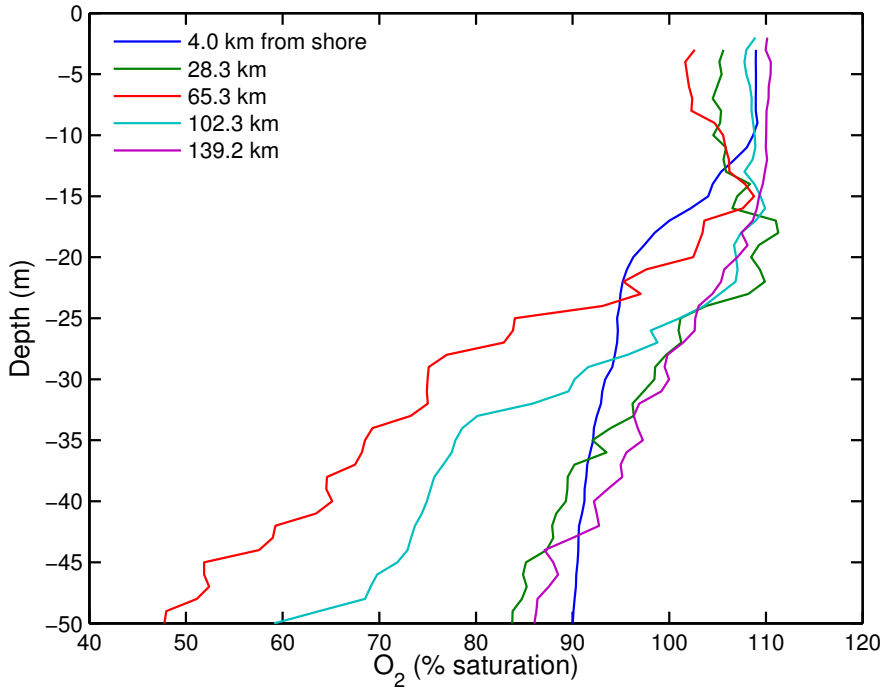

Figure 4.10: O_2 profiles from the August 2011 CalCOFI cruise, along Line 93.3. Stations 93.3 26.7 (4 km from shore) through 93.3 45 (139.2 km from shore) are shown.

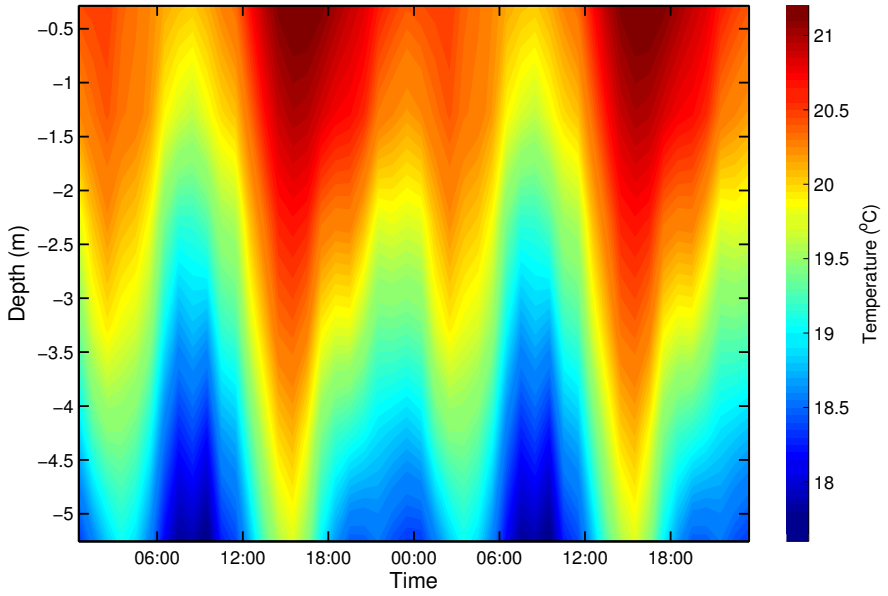

Figure 4.11: Mean diurnal cycle in water temperature, with depth. The same 24-hour period is shown twice.

measured O_2, there is also evidence of daily warming and cooling near the surface (Figure 4.11).

We set the fractionation factors to two sets of values (Cases 2 and 4). It has long been thought that photosynthesis does not fractionate oxygen (Guy et al., 1993). Based on this assumption, the fractionation factor of respiration was found to be 0.978 in the Southern Ocean and North Pacific (Quay et al., 1993; Hendricks et al., 2004), and 0.979 in the Equatorial Pacific (Hendricks et al., 2005). However, recent work suggests that photosynthesis does fractionate oxygen (Eisenstadt et al., 2010). Based on this finding, Luz and Barkan (2011) suggest a global average α_r of 0.9803, and α_p of 1.004 for the surface ocean. Therefore, we ran our model using the fractionation factors based on Luz and Barkan (2011) ($\alpha_r = 0.9803$, $\alpha_p = 1.004$) or Hendricks et al. (2004) ($\alpha_r = 0.978$, $\alpha_p = 1$).

As shown in Table 4.1, when the model was fit to O_2 first (Cases 1-4), P_{500} was consistently found to be 4.7 mmol O_2 m^{-3} hr^{-1}, and the mixing rate was consistently found to be 6.8-6.9 m day^{-1}. These results (red line, Figure 4.12) reproduce the timing of the cycle, as well as the average value, the amplitude, and

the fast decrease in O_2 at night. The best fitting $\bar{P}/R$ was less well constrained, and varied with C_m. $\bar{P}/R$ varied from 4.44 (for a C_m of 0 mmol m^{-3}) to 1.01 (for a C_m of 14.2 mmol m^{-3}). A survey of measurements from around the world found that P/R ratios in the coastal ocean are 1.17 on average, with a range of 0.03 to 34.3 (Duarte and Agustí, 1998), suggesting that our values are reasonable. We assume that $\bar{P}/R$ should be above 1 for our data, because a value below 1 would mean that there is more respiration than photosynthesis, which is inconsistent with the observed supersaturation in O_2. Changes in C_m also changed the best-fit $\delta^{18}O_m$, from -0.42 per mil for the low C_m, to -1.58 per mil for the high C_m. Previous observations of $\delta^{18}O$ in the Southern California Bight show values in this range (David Munro, personal communication). The amplitude of the modeled $\delta^{18}O$ cycle, and the best fitting $\delta^{18}O_m$, varied slightly for different values of α_r and α_p (Figure 4.12).

Using $\delta^{18}O$ rather than O_2 to find the best-fit parameters resulted in slightly different best-fit parameter values (Cases 5-8). The best fitting P_{500} was more variable than the fit using O_2, at 3.7-4.7 mmol O_2 m^{-3} hr^{-1}. $\bar{P}/R$ was again found to vary with the mixing endmember. M was 9.8-10.6 m day^{-1}, which is higher than when the model is fit to biological O_2 concentration.

We also tested two "special cases" (Cases 9 and 10, Table 4.1). In the first special case, we allowed respiration to be twice as high at night as during the day. This resulted in a slight decrease in the best fitting P_{500}, from 4.7 to 4.1 mmol O_2 m^{-3} hr^{-1}. The shape and quality of the fit was unchanged (not shown). For the second special case (Case 10), P_{500} was forced to be consistent with the assimilation number. The assimilation number is the photosynthesis rate per unit chlorophyll at optimal light intensity, and is around 8-10 mg C (mg Chl a)$^{-1}$ hr^{-1} in the summer (Harrison and Platt, 1980). The observed mean chlorophyll concentration at the pier was 2.55 μg L^{-1}, suggesting that the maximum photosynthesis rate should be 20.4-25.5 mg C m^{-3} hr^{-1}. Using a photosynthetic quotient of 1.4 (Laws, 1991), 25.5 mg C m^{-3} hr^{-1} is 2.98 mmol O_2 m^{-3} hr^{-1}. When the best fit to the data is found using this photosynthesis rate, the amplitude of the diurnal cycle is slightly underestimated (Figure 4.12, green line).

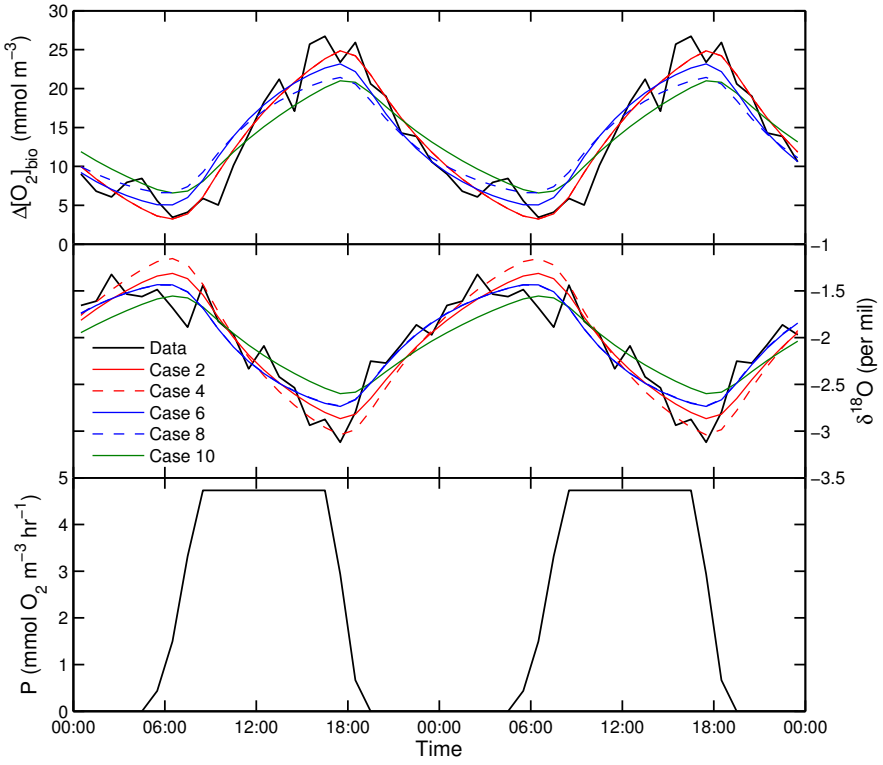

Figure 4.12: Mean measured diurnal cycle and modeled diurnal cycle, using 5 of the cases described in Table 4.1. The bottom panel shows how the photosynthesis rate varies over 24 hours, for Cases 1-4.

In this model, the cycle in O_2 and $\delta^{18}O$ is primarily a balance between photosynthesis, respiration, and mixing; air-sea gas exchange is a very small contribution (less than 5% of the sum of respiration and mixing fluxes). We find that mixing is necessary to reproduce the shape of the diurnal cycle. If mixing is excluded, and the remaining parameters are varied to find a new best fit, the maximum in the model is offset in time from the maximum in the data, and the biological O_2 concentration does not decrease fast enough at night (not shown).

4.5.2 Modeled relationship between O_2 and $\delta^{18}O$

The previous section shows that the diurnal cycles in biological O_2 concentration and $\delta^{18}O$ can be modeled using photosynthesis, respiration, mixing, and air-sea gas exchange. However, as shown in Section 4.4, the diurnal cycle represents only a small range of the variability in the measured O_2 and $\delta^{18}O$. We now use the model to understand other features in the data.

As shown in Figure 4.9, the biological O_2 concentration can be much higher than the biological O_2 concentration of the mean diurnal cycle. During Regime II, the mean diurnal cycle approaches these higher values of biological O_2 concentration. During this time, the chlorophyll data suggest that production was higher. Therefore, leaving the other model parameters unchanged, we increased P_{500} in the model to determine its effect on the diurnal cycle. Using a C_m of 7.1 mmol m^{-3} and a $\bar{P}/R$ of 1.64 (Cases 2 and 4) with a doubling of P_{500} (to 9.4 mmol O_2 m^{-3} hr^{-1}) allows the diurnal cycle to reach the highest O_2 and lowest $\delta^{18}O$ values, which describes the data in Regime II, as shown in Figure 4.13. Using $\alpha_r = 0.978$ with $\alpha_p = 1$ fits the slope of the data better than using $\alpha_r = 0.9803$ with $\alpha_p = 1.004$.

The low biological O_2 concentration values during the cold water intrusions (Regime I) cannot be explained with the existing parameters of the diurnal cycle model. However, using the deep water O_2 and $\delta^{18}O$ values from Kroopnick and Craig (1976), these cold water values can be understood. The model is initialized with C_i = -23.6 mmol m^{-3} and $\delta^{18}O_i$ = 1.31 per mil, which falls along a line fit to the Kroopnick and Craig data, shown in Figure 4.7. Then, we run the

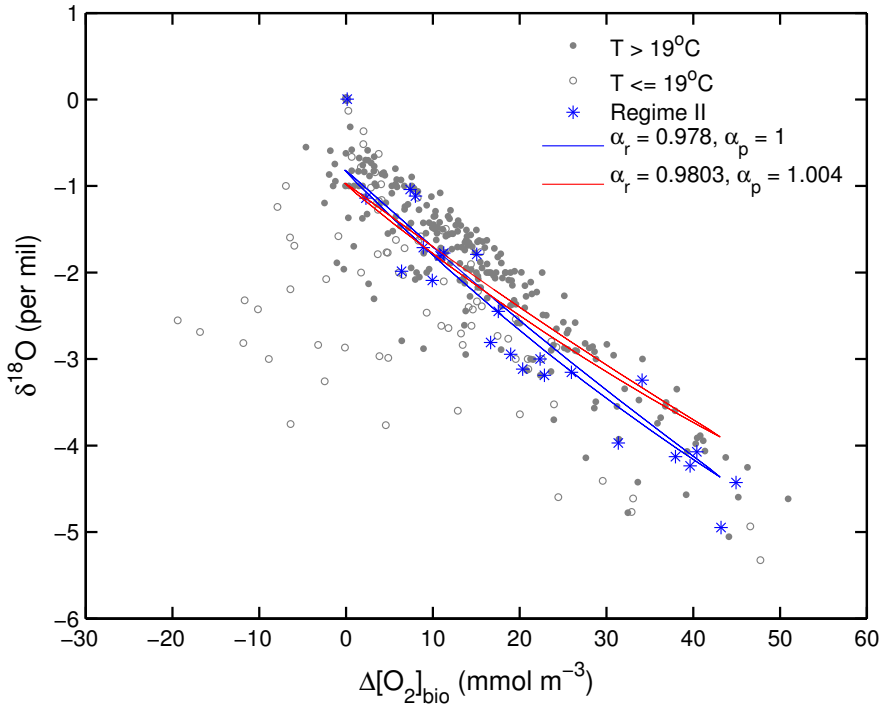

Figure 4.13: Modeled diurnal cycle for a doubling of the photosynthesis rate. The increase in P_{500} allows the high biological O_2 concentration/low $\delta^{18}O$ points to be reached. Results are shown using Cases 2 and 4 (Table 4.1), with P_{500} increased to 9.4 mmol O_2 m^{-3} hr^{-1}.

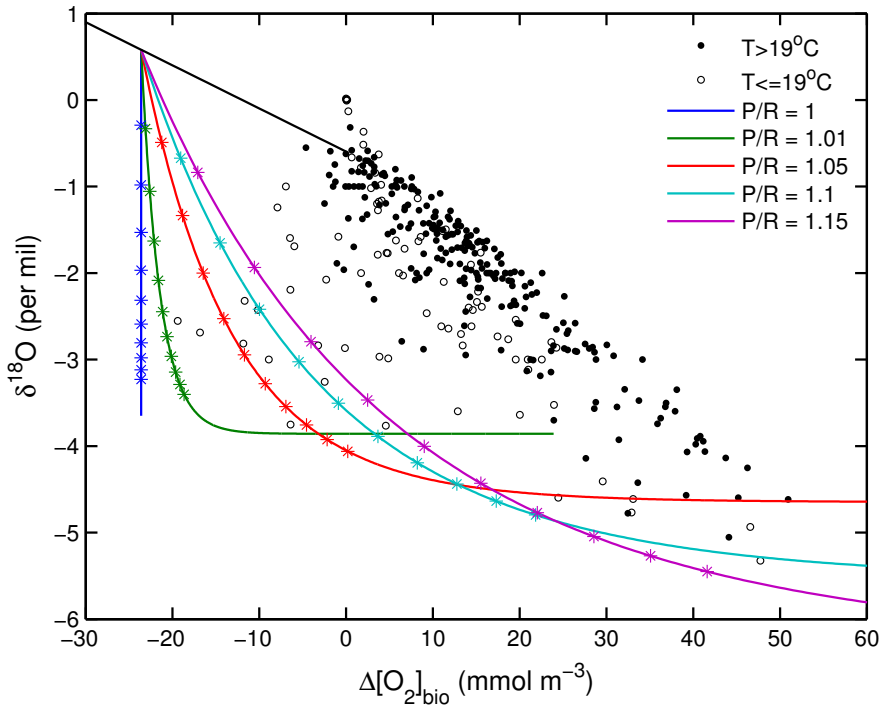

Figure 4.14: Time evolution of a water parcel starting at 90% oxygen saturation ($\Delta[O_2]_{bio}$ = -23.6 mmol m^{-3}), with different P/R ratios, for $\alpha_r = 0.9794$ and $\alpha_p = 1$. Stars show the gross O_2 production, from 50-500 mmol O_2 m^{-3}, in increments of 50 mmol O_2 m^{-3}. The black line shows the fit to the Kroopnick and Craig (1976) data with $\delta^{18}O_{sat}$ subtracted out, as shown in Figure 4.7.

model forward in time to "age" the parcel of water, using photosynthesis (without diurnal variability) and respiration, but not air-sea gas exchange or mixing. We find that, for a range of P/R close to 1, the model can describe the cold water data (Figure 4.14). However, these points can only be reached if the fractionation factor from respiration is lower than suggested by Quay et al. (1993), Hendricks et al. (2004), or Luz and Barkan (2011). We require $\alpha_r = 0.9834$ using $\alpha_p = 1.004$, or $\alpha_r = 0.9794$ using $\alpha_p = 1$, compared with values of $\alpha_r = 0.9803$ using $\alpha_p = 1.004$ (Luz and Barkan, 2011) and $\alpha_r = 0.978$ using $\alpha_p = 1$ (Hendricks et al., 2004).

4.6 Discussion

We observed a strong diurnal cycle in biological O_2 concentration and $\delta^{18}O$ at the SIO pier over 5 weeks during June and July, 2011. Previous studies have also observed diurnal variability in O_2 over long periods of time (e.g. Sanford et al., 1990; McNeil and Farmer, 1995; DeGrandpre et al., 1998; Jiang et al., 2011; Frieder et al., 2012). Diurnal variability in $\delta^{18}O$ has been observed over short time periods, but not over the length of time observed here (Sarma et al., 2005, 2006; Venkiteswaran et al., 2007). Measuring over a few weeks allowed us to compute a mean diurnal cycle, as well as observe longer-term changes in the data.

The amplitude of the mean diurnal cycle in oxygen is 19 mmol m^{-3}. Daily variations in oxygen of this magnitude and higher have also been observed in the nearby La Jolla Kelp Forest (63 μmol O_2 kg^{-1}; Frieder et al., 2012), as well as in coastal Taiwan (37-239 μmol O_2 kg^{-1}; Jiang et al., 2011). Our data suggest that the observed daily rise in O_2 is due to photosynthesis because: 1) the magnitude of the variation is supported by the variation in $\delta^{18}O$; 2) the biological O_2 concentration and $\delta^{18}O$ signals do not show semidiurnal variability, which would be present if advection were an important forcing; and 3) the timing of the diurnal cycle can be reproduced using diurnally varying photosynthesis based on PAR.

The measurements of dissolved O_2 and $\delta^{18}O$, along with a diurnal cycle model, can provide insights into the physical and biological processes in the coastal ocean. The mean observed diurnal cycle was fit using a model that includes photosynthesis, respiration, air-sea gas exchange, and mixing. The model shows that mixing plays an important role in the observed cycle in oxygen. This is consistent with results from Omand (2011) that show that in the nearshore region in Southern California, over longer timescales, mixing is necessary to explain nitrate fluxes that precede phytoplankton blooms. Our model could not constrain the P/R ratio, or the oxygen content of the mixing endmember. For values of C_m within the range of the observed O_2 saturation from CalCOFI data (0-14.2 mmol m^{-3}), P/R is 1.01-4.44. Endmembers of $\delta^{18}O$ fall between -0.42 and -1.58 per mil.

One well-constrained parameter in the model is the photosynthesis rate. The model gives a best-fit daily maximum photosynthesis rate (P_{500}) of 4.7 mmol

Table 4.2: Estimates of production rates using chlorophyll concentration, the diurnal cycle model, and the amplitude of the observed oxygen cycle. Production units are converted from mmol O_2 to mg C using a photosynthetic quotient of 1.4.

Production measure	Chlorophyll-based (^{14}C equivalent)	Modeled (GPP)	Lower bound (GPP)
mmol O_2 m^{-3} day^{-1}	25.9-32.3[a]	51.1	19.0
mg C m^{-3} day^{-1}	221.8-277.2	438.0[a]	162.9[a]

[a] Calculated using a photosynthetic quotient of 1.4.

O_2 m^{-3} hr^{-1} (fit to biological O_2 concentration, Cases 1-4) or 3.7-4.7 mmol O_2 m^{-3} hr^{-1} (fit to $\delta^{18}O$, Cases 5-8). The amplitude of the cycle was also used to determine a lower bound on the photosynthesis rate of 1.6 mmol O_2 m^{-3} hr^{-1}, for the extreme case where no loss processes (e.g. respiration, air-sea gas exchange, or mixing) occur during the day.

To understand the photosynthesis rate in terms of carbon production, we convert from gross oxygen production to gross carbon production using a photosynthetic quotient of 1.4 (Laws, 1991). This gives a gross carbon production rate of 40.3 mg C m^{-3} hr^{-1} based on the modeled photosynthesis rate (4.7 mmol O_2 m^{-3} hr^{-1}). Using the diurnal cycle in the photosynthesis rate (Figure 4.12), the daily production is computed to be 438.0 mg C m^{-3} day^{-1} (Table 4.2). The lower bound of the daily production, based on the amplitude of the O_2 cycle, is 162.9 mg C m^{-3} day^{-1}. These values can be compared to the photosynthesis rate expected from the assimilation number. Based on an assimilation number of 8-10 mg C (mg Chl a)$^{-1}$ hr^{-1} (Harrison and Platt, 1980) and a mean chlorophyll concentration of 2.55 μg L^{-1}, the photosynthesis rate should be 20.4-25.5 mg C m^{-3} hr^{-1}, or 221.8-277.2 mg C m^{-3} day^{-1}, under optimum conditions.

The chlorophyll-based production is lower than the value calculated by the model. However, the assimilation numbers reported by Harrison and Platt (1980) are based on ^{14}C incubations, which have been found to measure a value that is between gross and net primary production (e.g. Bender et al., 1999; Laws et al., 2000; Marra, 2009). Comparisons of production measurements using ^{18}O incubations to measure gross primary production with measurements using ^{14}C incubations have found a ratio of ^{18}O-based production to ^{14}C-based production of 2.7, which in-

cludes the photosynthetic quotient (Bender et al., 1999; Laws et al., 2000). This is due to the Mehler reaction and photorespiration (which produce a labeled ^{18}O molecule without carbon fixation), as well as respiration of labeled carbon, excretion of ^{14}C into dissolved organic carbon, and assimilation of unlabeled carbon (Bender et al., 1999). Although this discrepancy is based on ^{18}O incubations, recent work that measured gross primary production using the daily cycle in O_2/Ar (where GPP is calculated using the change in O_2/Ar during the daytime, minus the change at night) found a similar ratio of O_2 production to ^{14}C production: 3.5 $\pm$ 1.7 (Hamme et al., 2012). Using a ratio of 2.7 to convert our oxygen production estimates to ^{14}C-based production, we get a rate of 227.1 mg C m^{-3} day^{-1} for our modeled value (4.7 mmol O_2 m^{-3} hr^{-1}) and 84.4 mg C m^{-3} day^{-1} for the lower limit based on the amplitude of the cycle (1.6 mmol O_2 m^{-3} hr^{-1}). These values are consistent with the maximum production expected from the chlorophyll concentration (221.8-277.2 mg C m^{-3} day^{-1}).

It is possible that there are contributions to photosynthesis from benthic organisms, which would be in addition to production from the observed chlorophyll concentration. La Jolla Cove, directly south of the pier, is home to eelgrass and several types of macroalgae (Cottam and Munro, 1954; Gunnill, 1980). In addition, a large kelp forest is located further south, around Point La Jolla (North et al., 1993). These organisms would increase production without increasing the measured chlorophyll concentration. However, the contribution to total primary production from benthic organisms can vary greatly depending on the optical properties of the water (Meyercordt et al., 1999), and the contribution of benthic organisms in La Jolla Cove in unknown. In addition, the most productive region in La Jolla Cove is located 2-3 km south of the pier. The travel time of the water from this area to the pier would cause a delay in the measured production of at least 1-2 hours. This would offset the phase of the O_2 cycle, suggesting that benthic production is not a dominant contributor to the observed production.

The model that we used assumed constant respiration and mixing over 24 hours. Any enhancement of respiration or mixing at night would decrease the modeled production rate. For example, as the water surface cools at night,

convective mixing is expected to increase (Lynn and Svejkovsky, 1984). Also, studies have shown that the respiration rate of certain organisms can vary over the course of a day, with respiration rates highest in the early morning and the evening, or higher at night than during the day (Duval and Geen, 1976; Pavlova, 1994). If respiration rates are doubled at night in the model, this results in a small decrease in the photosynthesis rate needed to explain the diurnal cycle (4.7 mmol O_2 m^{-3} hr^{-1} vs 4.1 mmol O_2 m^{-3} hr^{-1}, Table 4.1). A strong diurnal cycle in mixing or respiration could cause the estimated production to be as low as the lower bound (1.6 mmol O_2 m^{-3} hr^{-1}).

We have also used the model to explain variations in the data over longer periods of time. From June 26-July 3, the water had short periods of low biological O_2 concentration, which were likely due to internal tides (Regime I). These low O_2, low $\delta^{18}O$ measurements can be explained by photosynthesis and respiration occurring in a deep water parcel, causing only small changes in O_2, but lowering $\delta^{18}O$. After July 3, negative biological O_2 concentrations were no longer observed, and instead, the measured values fall along the line of $\delta^{18}O$ versus O_2 formed by the warm water data (Regime II). As shown by Bender and Grande (1987), it is not possible for any combination of photosynthesis and respiration alone to increase both O_2 and $\delta^{18}O$. Air-sea gas exchange is the only process that could increase both values. Therefore, although our model shows that the contribution from air-sea gas exchange is small relative to other processes on a diurnal timescale, air-sea gas exchange is likely more important over longer timescales. A possible explanation of the transition from Regime I to Regime II is that different water masses were being measured, and that during Regime II, the water was more influenced by air-sea gas exchange. The transition from Regime II to Regime III can be explained by a reduced input of nutrients. This would have reduced the rate of photosynthesis, which would reduce the magnitude of the diurnal cycle in O_2.

4.7 Conclusions

Using an equilibrator interfaced to a mass spectrometer, we observed O_2, Ar, and $\delta^{18}O$ in the coastal ocean over 5 weeks. Such a large dataset allowed observations of features that are not seen with traditional bottle samples. We observed a diurnal cycle in biological O_2 and $\delta^{18}O$, and showed that this cycle can be explained primarily by photosynthesis, respiration and mixing, but not by photosynthesis and respiration alone. We also observed longer-term variations in the relationship between O_2 and $\delta^{18}O$, which can be explained by different water sources and changes in the nutrient supply. We found a rate of photosynthesis that is in agreement with what is expected from the measured chlorophyll concentration, using a ratio of O_2-based production to ^{14}C-based production of 2.7. Although we could not constrain the P/R ratio, future studies that include measurements of $\delta^{18}O$ and O_2 at different depths could allow for a better calculation of P/R.

4.8 Acknowledgements

We thank Todd Martz and Yui Takeshita for help with the optode, David Munro for sharing his data of $\delta^{18}O$ in the Southern California Bight, and Lisa Welp and Chun-Ta Lai for providing measurements of $\delta^{18}O$ of H_2O at the SIO pier. SIO pier temperature chain profile data was provided by Eric Terrill, Coastal Observing R&D Center, Scripps Institution of Oceanography. We thank Drew Lucas, Ralf Goericke, John McGowan, Christina Frieder, and Melissa Carter for helpful discussions.

This chapter, in part, is being prepared for publication. Lauren Elmegreen Rafelski, Bill Paplawsky, and Ralph F. Keeling. I am the primary investigator and author of this paper.

References

Abe, O., and Yoshida, N., 2003: Partial pressure dependency of $^{17}O/^{16}O$ and $^{18}O/^{16}O$ of molecular oxygen in the mass spectrometer. *Rapid Communications in Mass Spectrometry*, **17**, 395–400.

Antoine, D., Andre, J.-M., and Morel, A., 1996: Oceanic primary production 2. Estimation at global scale from satellite (coastal zone color scanner) chlorophyll. *Global Biogeochemical Cycles*, **10**(1), 57–69.

Bender, M., Orchardo, J., Dickson, M.-L., Barber, R., and Lindley, S., 1999: In vitro O_2 fluxes compared with ^{14}C production and other rate terms during the JGOFS Equatorial Pacific experiment. *Deep Sea Research I*, **46**, 637–654.

Bender, M. L., and Grande, K. D., 1987: Production, respiration, and the isotope geochemistry of O_2 in the upper water column. *Global Biogeochemical Cycles*, **1**(1), 49–59.

Benson, B. B., and Krause, D., Jr., 1980: The concentration and isotopic fractionation of gases dissolved in freshwater in equilibrium with the atmosphere. 1. Oxygen. *Limnology and Oceanography*, **25**(4), 662–671.

Cottam, C., and Munro, D. A., 1954: Eelgrass status and environmental relations. *Journal of Wildlife Management*, **18**(4), 449–460.

Craig, H., and Hayward, T., 1987: Oxygen supersaturation in the ocean: biological versus physical contributions. *Science*, **235**(4785), 199–202.

DeGrandpre, M. D., Hammar, T. R., and Wirick, C. D., 1998: Short-term pCO_2 and O_2 dynamics in California coastal waters. *Deep-Sea Research II*, **45**, 1557–1575.

Duarte, C. M., and Agustí, S., 1998: The CO_2 balance of unproductive aquatic ecosystems. *Science*, **281**, 234–236.

Duval, W. S., and Geen, G. H., 1976: Diel feeding and respiration rhythms in zooplankton. *Limnology and Oceanography*, **21**(6), 823–829.

Eisenstadt, D., Barkan, E., Luz, B., and Kaplan, A., 2010: Enrichment of oxygen heavy isotopes during photosynthesis in phytoplankton. *Photosynthesis Research*, **103**, 97–103.

Frieder, C. A., Nam, S. H., Martz, T. R., and Levin, L. A., 2012: High temporal and spatial variability of dissolved oxygen and pH in a nearshore California kelp forest. *Biogeosciences Discussions*, **9**, 4099–4132.

Garcia, H. E., and Gordon, L. I., 1992: Oxygen solubility in seawater: Better fitting equations. *Limnology and Oceanography*, **37**(6), 1307–1312.

Gilstad, M., Johnsen, G., and Sakshaug, E., 1993: Photosynthetic parameters, pigment composition and respiration rates of the marine diatom *Skeletonema costatum* grown in continuous light and a 12:12 h light-dark cycle. *Journal of Plankton Research*, **15**(8), 939–951.

Gunnill, F. C., 1980: Recruitment and standing stocks in populations of one green alga and five brown algae in the intertidal zone near La Jolla, California during 1973-1977. *Marine Ecology Progress Series*, **3**, 231–243.

Guy, R. D., Fogel, M. L., and Berry, J. A., 1993: Photosynthetic fractionation of the stable isotopes of oxygen and carbon. *Plant Physiology*, **101**, 37–47.

Hamme, R. C., Cassar, N., Lance, V. P., Vaillancourt, R. D., Bender, M. L., Strutton, P. G., Moore, T. S., DeGrandpre, M. D., Sabine, C. L., Ho, D. T., and Hargreaves, B. R., 2012: Dissolved O_2/Ar and other methods reveal rapid changes in productivity during a Lagrangian experiment in the Southern Ocean. *Journal of Geophysical Research*, **117**(C00F12), doi:10.1029/2011JC007046.

Harrison, W. G., and Platt, T., 1980: Variations in assimilation number of coastal marine phytoplankton: Effects of environmental co-variates. *Journal of Plankton Research*, **2**(4), 249–260.

Hendricks, M. B., Bender, M. L., and Barnett, B. A., 2004: Net and gross O_2 production in the Southern Ocean from measurements of biological O_2 saturation and its triple isotope composition. *Deep-Sea Research I*, **51**, 1541–1561.

Hendricks, M. B., Bender, M. L., Barnett, B. A., Strutton, P., and Chavez, F. P., 2005: Triple oxygen isotope composition of dissolved O_2 in the equatorial Pacific: A tracer of mixing, production, and respiration. *Journal of Geophysical Research*, **110**(C12021), doi:10.1029/2004JC002735.

Jiang, Z.-P., Huang, J.-C., Dai, M., Kao, S. J., Hydes, D. J., Chou, W.-C., and Jan, S., 2011: Short-term dynamics of oxygen and carbon in productive nearshore shallow seawater systems off Taiwan: Observations and modeling. *Limnology and Oceanography*, **56**(5), 1832–1849.

Knox, M., Quay, P. D., and Wilbur, D., 1992: Kinetic isotopic fractionation during air-water gas transfer of O_2, N_2, CH_4, and H_2. *Journal of Geophysical Research*, **97**(C12), 20335–20343.

Kroopnick, P., and Craig, H., 1972: Atmospheric oxygen: Isotopic composition and solubility fractionation. *Science*, **175**(4017), 54–55.

Kroopnick, P., and Craig, H., 1976: Oxygen isotope fractionation in dissolved oxygen in the deep sea. *Earth and Planetary Science Letters*, **32**, 375–388.

Lane, G. A., and Dole, M., 1956: Fractionation of oxygen isotopes during respiration. *Science*, **123**(3197), 574–576.

Laws, E. A., 1991: Photosynthetic quotients, new production and net community production in the open ocean. *Deep-Sea Research*, **38**(1), 143–167.

Laws, E. A., Landry, M. R., Barber, R. T., Campbell, L., Dickson, M.-L., and Marra, J., 2000: Carbon cycling in primary production bottle incubations: Inferences from grazing experiments and photosynthetic studies using ^{14}C and ^{18}O in the Arabian Sea. *Deep-Sea Research II*, **47**, 1339–1352.

Levine, N. M., Bender, M. L., and Doney, S. C., 2009: The $\delta^{18}O$ of dissolved O_2 as a tracer of mixing and respiration in the mesopelagic ocean. *Global Biogeochemical Cycles*, **23**(GB1006), doi:10.1029/2007GB003162.

Lomb, N. R., 1976: Least-squares frequency analysis of unequally spaced data. *Astrophysics and Space Science*, **39**, 447–462.

Lucas, A. J., Franks, P. J. S., and Dupont, C. L., 2011: Horizontal internal-tide fluxes support elevated phytoplankton productivity over the inner continental shelf. *Limnology and Oceanography: Fluids and Environments*, **1**, 56–74.

Luz, B., and Barkan, E., 2009: Net and gross oxygen production from O_2/Ar, $^{17}O/^{16}O$ and $^{18}O/^{16}O$ ratios. *Aquatic Microbial Ecology*, **56**, 133–145.

Luz, B., and Barkan, E., 2011: The isotopic composition of atmospheric oxygen. *Global Biogeochemical Cycles*, **25**(GB3001), doi:10.1029/2010GB003883.

Lynn, R. J., and Svejkovsky, J., 1984: Remotely sensed sea surface temperature variability off California during a "Santa Ana" clearing. *Journal of Geophysical Research*, **89**(C5), 8151–8162.

Marra, J., 2009: Net and gross productivity: Weighing in with ^{14}C. *Aquatic Microbial Ecology*, **56**, 123–131.

Marra, J., Heinemann, K., and Landriau, J., Gene, 1985: Observed and predicted measurements of photosynthesis in a phytoplankton culture exposed to natural irradiance. *Marine Ecology Progress Series*, **24**, 43–50.

McNeil, C. L., and Farmer, D. M., 1995: Observations of the influence of diurnal convection on upper ocean dissolved gas measurements. *Journal of Marine Research*, **53**, 151–169.

Meyercordt, J., Gerbersdorf, S., and Meyer-Reil, L.-A., 1999: Significance of pelagic and benthic primary production in two shallow coastal lagoons of different degrees of eutrophication in the southern Baltic Sea. *Aquatic Microbial Ecology*, **20**, 273–284.

North, W. J., James, D. E., and Jones, L. G., 1993: History of kelp beds (*Macrocystis*) in Orange and San Diego Counties, California. *Hydrobiologia*, **260/261**, 277–283.

Omand, M. M., 2011: *Physical controls on episodic nearshore phytoplankton blooms in Southern California*. Ph.D. thesis, University of California, San Diego.

Pavlova, E. V., 1994: Diel changes in copepod respiration rates. *Hydrobiologia*, **292/293**, 333–339.

Platt, T., and Jassby, A. D., 1976: The relationship between photosynthesis and light for natural assemblages of coastal marine phytoplankton. *Journal of Phycology*, **12**, 421–430.

Quay, P. D., Emerson, S., Wilbur, D. O., and Stump, C., 1993: The δ^{18}O of dissolved O_2 in the surface waters of the Subarctic Pacific: A tracer of biological productivity. *Journal of Geophysical Research*, **98**(C5), 8447–8458.

Quiñones-Rivera, Z. J., Wissel, B., and Justić, D., 2009: Development of productivity models for the northern Gulf of Mexico based on oxygen concentrations and stable isotopes. *Estuaries and Coasts*, **32**, 436–446.

Quiñones-Rivera, Z. J., Wissel, B., Justić, D., and Fry, B., 2007: Partitioning oxygen sources and sinks in a stratified, eutrophic coastal ecosystem using stable oxygen isotopes. *Marine Ecology Progress Series*, **342**, 69–83.

Sanford, L. P., Sellner, K. G., and Breitburg, D. L., 1990: Covariability of dissolved oxygen with physical processes in the summertime Chesapeake Bay. *Journal of Marine Research*, **48**, 567–590.

Sarma, V. V. S. S., Abe, O., Hashimoto, S., Hinuma, A., and Saino, T., 2005: Seasonal variations in triple oxygen isotopes and gross oxygen production in the Sagami Bay, central Japan. *Limnology and Oceanography*, **50**(2), 544–552.

Sarma, V. V. S. S., Abe, O., Hinuma, A., and Saino, T., 2006: Short-term variation of triple oxygen isotopes and gross oxygen production in the Sagami Bay, central Japan. *Limnology and Oceanography*, **51**(3), 1432–1442.

Scargle, J. D., 1982: Studies in astronomical time series analysis. II. Statistical aspects of spectral analysis of unevenly spaced data. *Astrophysical Journal*, **263**, 835–853.

Venkiteswaran, J. J., Wassenaar, L. I., and Schiff, S. L., 2007: Dynamics of dissolved oxygen isotopic ratios: A transient model to quantify primary production, community respiration, and air-water exchange in aquatic ecosystems. *Oecologia*, **153**, 385–398.

Wanninkhof, R., 1992: Relationship between wind speed and gas exchange over the ocean. *Journal of Geophysical Research*, **97**(C5), 7373–7382.

Weiss, R. F., 1970: The solubility of nitrogen, oxygen, and argon in water and seawater. *Deep-Sea Research*, **17**, 721–735.

Westberry, T., Behrenfeld, M. J., Siegel, D. A., and Boss, E., 2008: Carbon-based primary productivity modeling with vertically resolved photoacclimation. *Global Biogeochemical Cycles*, **22**(GB2024), doi:10.1029/2007GB003078.

Yoshie, N., Suzuki, K., Kuwata, A., Nishioka, J., and Saito, H., 2010: Temporal and spatial variations in photosynthetic physiology of diatoms during the spring bloom in the western subarctic pacific. *Marine Ecology Progress Series*, **399**, 39–52.

Chapter 5

Measurements of $^{17}\Delta$ in the coastal surface ocean

5.1 Introduction

Measurements of oceanic primary production are an important part of understanding the global carbon cycle, as well as the ocean's food web. As explained in Chapter 4, measurements of δ^{18}O of dissolved O_2 can be used to determine production rates. Gross primary production (GPP) can also be determined using the relative amounts of ^{16}O, ^{17}O, and ^{18}O in dissolved O_2 (the triple isotopic composition). This technique has been used around the world to calculate GPP (e.g. Hendricks et al., 2004; Juranek and Quay, 2005; Sarma et al., 2005; Reuer et al., 2007; Luz and Barkan, 2009; Stanley et al., 2010; Hamme et al., 2012; Quay et al., 2012).

The triple isotopic composition can be expressed as Δ^{17}O:

$$\Delta^{17}O = \delta^{17}O - \lambda\delta^{18}O \tag{5.1}$$

where λ, the mass-dependent fractionation factor, is 0.518 (Luz and Barkan, 2005). δ^{18}O and δ^{17}O are defined as:

$$\delta^{x}O = \frac{(^{x}O/^{16}O)_s}{(^{x}O/^{16}O)_r} - 1 \tag{5.2}$$

where x is 17 or 18, the subscripts s and r stand for sample and reference values, and δ^xO is multiplied by 10^3 to give units of per mil or 10^6 to give units of per meg.

Equation 5.1 is an approximation of:

$$^{17}\Delta = ln\left(\frac{^{17}R}{^{17}R_{ref}}\right) - \lambda ln\left(\frac{^{18}R}{^{18}R_{ref}}\right) \tag{5.3}$$

where ^{17}R or ^{18}R is the ratio of the oxygen isotope to $^{16}O_2$ (e.g. $^{17}O^{16}O/^{16}O_2$) and R_{ref} is the reference ratio (Angert et al., 2003). Processes that cause mass-dependent fractionation conserve $^{17}\Delta$ because the change in δ^{17}O due to mass-dependent fractionation is around half the change in δ^{18}O.

O_2 in the ocean has two sources: dissolution of atmospheric O_2, and photosynthetic production. Ozone reactions in the stratosphere cause O_2 to be depleted in ^{17}O and ^{18}O in a mass-independent way (Thiemens et al., 1995; Luz et al., 1999). However, dissolved O_2 produced by photosynthesis is not affected by stratospheric chemistry. Atmospheric O_2 is defined to have a $^{17}\Delta$ of zero per meg, and O_2 produced by photosynthesis has a $^{17}\Delta$ of 249 per meg relative to atmospheric O_2 (Luz and Barkan, 2000). This difference in $^{17}\Delta$ between atmospheric O_2 and photosynthetically produced O_2 allows GPP to be determined based on the measured $^{17}\Delta$. Respiration does not affect $^{17}\Delta$ because the respiration fractionation is mass-dependent (i.e. the change in δ^{17}O is 0.518 times the change in δ^{18}O). Therefore, calculating production from $^{17}\Delta$ does not depend on the fractionation factor of respiration, giving this technique an advantage over using δ^{18}O of dissolved O_2.

Measurements of $^{17}\Delta$ taken with discrete water samples have shown that $^{17}\Delta$ can vary over daily (e.g. Sarma et al., 2005; Luz and Barkan, 2009) and seasonal (e.g. Juranek and Quay, 2005; Luz and Barkan, 2009; Quay et al., 2010, 2012) timescales. Also, Juranek and Quay (2010) showed that $^{17}\Delta$ and GPP can have strong variations over spatial scales. Continuous measurements of O_2/Ar have shown variability in net community production (NCP) on small temporal and spatial scales (e.g. Stanley et al., 2010; Hamme et al., 2012). Similarly, continuous measurements of $^{17}\Delta$ would better allow for measurement of the variability in GPP. In Chapters 2-4 in this thesis, we described techniques for continuous measurements

of dissolved gases, and highlighted measurements of $\delta^{18}O$. These techniques have the potential to work for continuous $^{17}\Delta$ measurements as well.

In Chapter 4, we discussed measurements of $\delta^{18}O$ taken at the Scripps Institution of Oceanography (SIO) pier. While these measurements were taken, m/z 33 was simultaneously measured on the mass spectrometer, allowing for the calculation of $^{17}\Delta$. Unfortunately, the noise in the measurement of $\delta^{17}O$ was too high for the same level of analysis to be applied to $^{17}\Delta$ as was applied to $\delta^{18}O$. In this chapter we discuss sources of noise to the measured $^{17}\Delta$, determine the mean measured value of $^{17}\Delta$, and expand the model from Chapter 4 to include $^{17}\Delta$.

5.2 Methods

Sampling methods are explained in detail in Chapters 2-3, and will not be repeated here. However, the measurement of $^{17}\Delta$ requires additional corrections, which are described in this section.

5.2.1 Nonlinear correction

The mass spectrometer signal is a function of how many ions are present at a given m/z ratio. Although the signal will increase when there are more ions, nonlinearities in the amplifier or the collection efficiency can cause the signal response to be nonlinear. $^{17}\Delta$ is essentially a measurement of the deviation from the expected, mass-dependent relationship between $\delta^{17}O$ and $\delta^{18}O$. Therefore, it is sensitive to any nonlinearities in the measurements of m/z 33 and m/z 34. Because gas compositions measured by a mass spectrometer are quantified by looking at the ratio between two m/z signals, we can determine the nonlinearity in m/z 33 or m/z 34 by looking at the relationship between m/z 33 or m/z 34 and m/z 32 as the pressure of gas in the mass spectrometer is varied.

The nonlinearity can be thought of as the slope of m/z 33 or m/z 34 versus m/z 32 near the typical operating conditions (the "local slope," m_i) relative to the slope from the typical operating conditions to zero signal (the "overall slope," m_0). The local and overall slopes were measured by varying the amount of gas

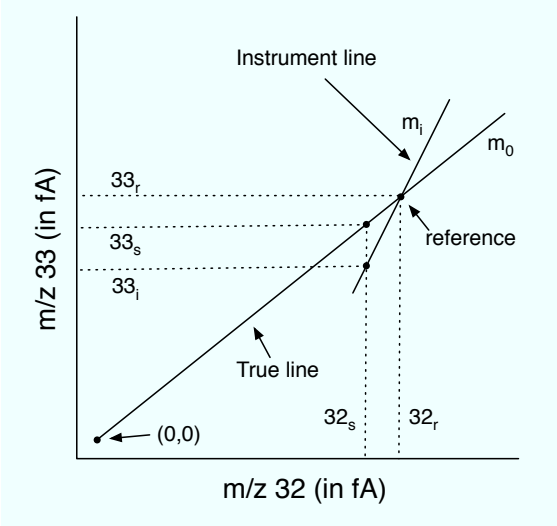

Figure 5.1: Schematic of the values needed to compute the nonlinear correction. The "instrument line" is relationship between m/z 33 and m/z 32 measured by the instrument. The "true line" is the relationship that would be measured without nonlinearities. Not to scale.

that was added to the mass spectrometer, and recording the raw output in fA. We measured the signals with no gas added (i.e. mass spectrometer inlet closed), and at pressures up to the normal operating pressure of the mass spectrometer. Based on these tests, m_0/m_i is 0.99 for m/z 34, and 0.97 for m/z 33. The m_0/m_i ratio can be used to correct the measured δ^{17}O and δ^{18}O.

We can represent the measured m/z 33 signal (33_i) as a function of the local slope (m_i) and the deviation of m/z 32 from the reference value, as shown in Figure 5.1:

$$33_i - 33_r = m_i(32_s - 32_r) \tag{5.4}$$

where the subscript r is the reference value, 32_s is the sample value of m/z 32, and 33_i is the measured value of m/z 33.

The m/z 33 signal that would be measured (33_s) if the mass spectrometer were perfectly linear, is:

$$33_s - 33_r = m_0(32_s - 32_r) \tag{5.5}$$

where m_0 is the overall slope.

These equations can be combined to obtain the corrected m/z 33 signal from the measured signal:

$$33_s - 33_r = \frac{m_0}{m_i}(33_i - 33_r) \tag{5.6}$$

It is more convenient to apply a correction directly to δ^{17}O or δ^{18}O than to the raw m/z value. To achieve this, we first divide Equation 5.6 by 32_r:

$$\frac{33_s}{32_r} - \frac{33_r}{32_r} = \frac{m_0}{m_i}\left(\frac{33_i}{32_r} - \frac{33_r}{32_r}\right) \tag{5.7}$$

To measure δ^{17}O and δ^{18}O, we added N_2 gas to the sample to keep O_2/N_2 near the reference value (Chapter 3). Therefore, the m/z 32 reference signal is approximately equal to the m/z 32 sample signal, and Equation 5.7 can be approximated as:

$$\frac{33_s}{32_s} - \frac{33_r}{32_r} = \frac{m_0}{m_i}\left(\frac{33_i}{32_s} - \frac{33_r}{32_r}\right) \tag{5.8}$$

Using the definition of a delta value (Equation 5.2), we can divide Equation 5.8 by $33_r/32_r$ to obtain the corrected δ^{17}O:

$$\delta^{17}O_{corr} = \frac{\left(\frac{m_0}{m_i}\right)\delta^{17}O_i\left(\frac{33_r}{32_r}\right)}{33_r/32_r} = \frac{m_0}{m_i}\delta^{17}O_i \tag{5.9}$$

This provides a simple way to correct measured delta values ($\delta^{17}O_i$) to the values that would have been measured without the nonlinearity. The same equations, with different values of m_0 and m_i, also apply to δ^{18}O.

5.2.2 Filtering of δ^{17}O

As explained in Chapter 3, delta values are calculated from raw fA signals of the mass spectrometer, which switches between a sample and reference gas every 10 seconds. The δ^{17}O signal, processed as described in Chapter 3, was found to be very noisy. Figure 5.2 shows δ^{17}O measured from a cylinder of gas. When 20-minute means were calculated from these data, the standard deviation of the resulting means was 67.5 per meg. In comparison, when a cylinder of gas was measured on an identical mass spectrometer in our lab, the standard deviation of 20-minute means was 11.7 per meg. To determine the cause of the higher noise on

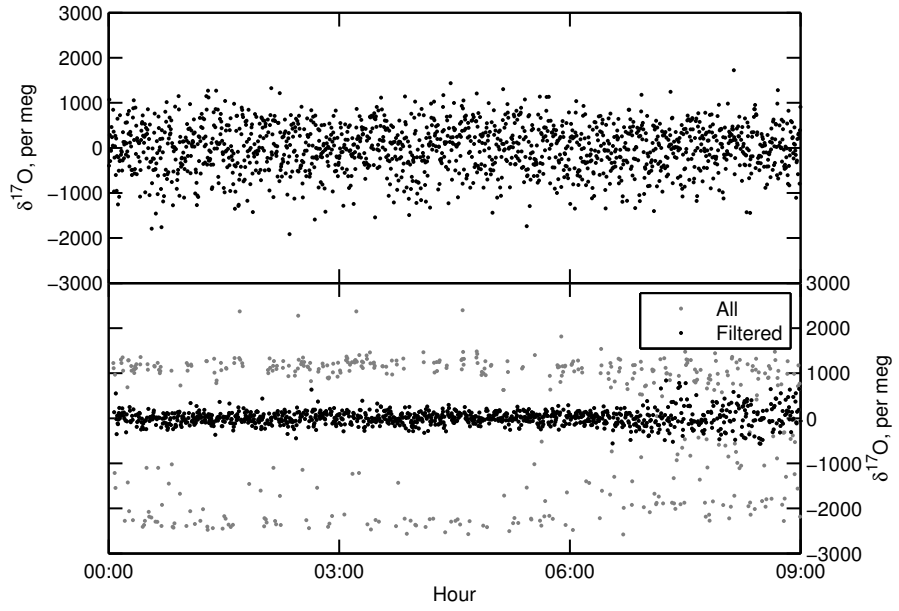

Figure 5.2: Top: δ^{17}O of a cylinder of gas, without any filtering. Bottom: δ^{17}O from the cylinder with filtering. The "mode filtered" data includes all the points in the bottom figure. Data remaining after the outlier filter was applied (as explained in the text) are shown in black.

the mass spectrometer used for measuring equilibrated air, we looked at the raw fA data of m/z 33, which has 100 ms resolution. Inspection of the raw data revealed that there were spikes at irregular intervals, possibly due to electrical issues at the m/z 33 collector. In an effort to reduce the noise of the signal, these spikes were filtered using the following procedure.

First, the m/z 33 signal was divided by the m/z 32 signal. Then, for each window of a 10-second sample or reference jog (i.e. the period of time that is averaged over to get the sample or reference value for the calculation of delta values), the mode of the data was found, and data within a small range of this mode were retained, while data outside of this range were excluded. We will refer to this step as "mode filtering." The sample or reference mean was then calculated from the remaining data, and $\delta(33/32)$ was calculated using Equation 5.2.

The mode filtering was successful in removing most of the spikes in m/z 33. However, in some instances, the 10 second sample or reference jog contained more

"spike" data than "good" data, and as a result the mode filtering retained the spike and removed the "good" data. As shown in Figure 5.2, when this procedure is performed on data from a cylinder of gas, most of the data fall in a narrow range, but there are many outliers. The outliers are due to intervals in which the spike data were kept instead of the good data. When the mode filtering was applied to equilibrator data (not shown), the results similarly show a narrow range of points with occasional outliers.

To remove the outliers, the delta values were further processed. For each jog (e.g. N_2-addition jog or no-N2-addition jog for the equilibrator data, described in Chapter 3, or 20 minutes of the cylinder data shown in Figure 5.2), a line was fit to the $\delta(33/32)$ vs. $\delta(32/28)$ data from that jog. This trendline was then subtracted from the $\delta(33/32)$ data, and points outside of 1 standard deviation of the detrended data were removed. Then, this process was repeated with the remaining data, and points farther than 500 per meg from the detrended data were removed. As shown in Figure 5.2, when this procedure is applied to the cylinder data, the result is that the data in the central band are retained, and the outliers due to spikes in the m/z 33 data are removed. This resulted in a standard deviation in the 20-minute means of 27.1 per meg, which is a significant improvement over the 67.5 per meg standard deviation of the unfiltered data, but still does not match the precision of the other instrument.

5.3 Model

In Chapter 4, we found that there was a diurnal cycle in dissolved O_2 and $\delta^{18}O$ measured at the SIO pier, which we modeled using photosynthesis, respiration, air-sea gas exchange, and mixing. Here we add $\delta^{17}O$ to the model, and use these results with the model output of $\delta^{18}O$ to compute $^{17}\Delta$. The time rate of change in $\delta^{17}O$ can be expressed using the same equation as the time rate of change in $\delta^{18}O$ (presented in Chapter 4), but with different values for the constants:

$$h\frac{d}{dt}(CX^{17}) = PX_w^{17}\alpha_p^{17} - RX^{17}\alpha_r^{17} + k\alpha_k^{17}(C_{sat}X_{sat}^{17} - CX^{17}) + M(C_mX_m^{17} - CX^{17}) \tag{5.10}$$

Table 5.1: Constants used to model δ^{18}O and δ^{17}O. Values used for δ^{18}O are explained in Chapter 4.

Model parameter	δ^{18}O	δ^{17}O
$\delta^x O_w$, per mil	-23.46	-11.90
$\delta^x O_{sat}$, per mil	0.73039	0.39168
α_p	1.004	1.002
α_r	0.9803	0.9897
α_k	0.9972	0.9985

where h is the box depth, C is the oxygen concentration, P is photosynthesis, R is respiration, k is the gas exchange coefficient, M is the mixing rate, C_{sat} is the oxygen concentration at saturation, and C_m is the oxygen concentration of water mixing into the box. k is determined using a wind-speed parameterization (Wanninkhof, 1992) and a mean wind speed of 2.47 m s^{-1}. X^{17} is the ratio of $^{17}O^{16}O$ to $^{16}O^{16}O$, and can be substituted with (1+δ^{17}O/1000), where δ^{17}O is in units of per mil. The subscripts w, sat, and m represent the isotopic composition of oxygen in H_2O, at saturation with air, and in the mixing endmember, respectively. α_p^{17}, α_r^{17}, and α_k^{17} are the fractionation factors of photosynthesis, respiration and kinetic gas exchange, respectively.

Values of $\delta^{17}O_w$, $\delta^{17}O_{sat}$, α_p^{17}, α_r^{17}, and α_k^{17} are shown in Table 5.1. $\delta^{17}O_w$ is computed by assuming that $^{17}\Delta_w$ is 249 per meg (Luz and Barkan, 2000). Since $\delta^{18}O_w$ is -23.46 per meg (Chapter 4), this results in a $\delta^{17}O_w$ of -11.90 per meg using a λ of 0.518.

For $\delta^{17}O_{sat}$, we first compute $^{17}\Delta_{sat}$ (Luz and Barkan, 2009):

$$^{17}\Delta_{sat} = 0.6T + 1.8 \tag{5.11}$$

where T is in degrees C and $^{17}\Delta_{sat}$ is in per meg. This results in a $^{17}\Delta_{sat}$ of 13.34 per meg for our mean measured temperature of 19.24^{o}C. Using a $\delta^{18}O_{sat}$ of 0.73039 (Benson and Krause, 1980), $\delta^{17}O_{sat}$ is calculated to be 0.39168. α_p^{17}, α_r^{17}, and α_k^{17} are all calculated by assuming that $\alpha^{17} = (\alpha^{18})^{0.518}$.

After δ^{17}O was computed using a forward run of the model, $\delta^{17}O_{sat}$ was subtracted from the result. As explained in Chapter 4, this is because we measure equilibrated air, so the measured δ^{17}O is offset from dissolved gas by the equilibrium fractionation. Then, $^{17}\Delta$ was calculated using Equation 5.3.

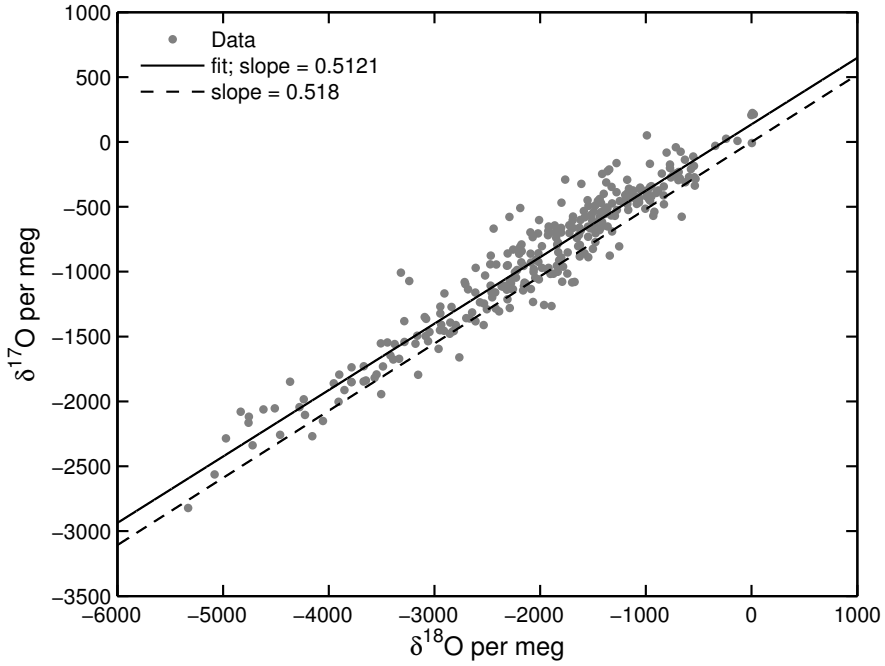

Figure 5.3: δ^{17}O versus δ^{18}O from the equilibrator data. A fit to the data (solid line) has a slope of 0.5121. The respiration slope (dashed line) is 0.518.

5.4 Results

5.4.1 Observed $^{17}\Delta$

The δ^{17}O and δ^{18}O of dissolved O_2 were measured at the SIO pier from June 22-August 1, 2011, at 2 m depth. The relationship between the measured δ^{17}O and δ^{18}O is shown in Figure 5.3. Also shown are a linear fit to the data, and the slope expected from respiration (0.518). The slope of the data (0.5121) is less than the respiration slope. The respiration slope would apply if only respiration were occurring. However, photosynthesis is also taking place. Lower values of δ^{18}O are consistent with more photosynthetic production of O_2, which should increase $^{17}\Delta$. An increase in $^{17}\Delta$ means that at a given δ^{18}O, δ^{17}O should be higher than expected from the respiration slope, which would lead to a lower slope in the data. Therefore, our observed slope is consistent with photosynthetic production of O_2.

The data shown in Figure 5.3 were used to calculate $^{17}\Delta$ using Equation 5.3.

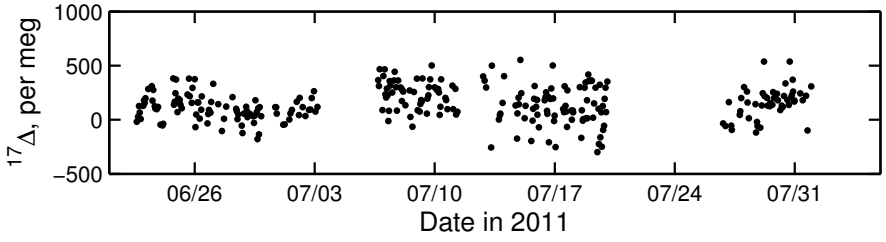

Figure 5.4: Timeseries of $^{17}\Delta$ measurements at the Scripps Institution of Oceanography pier.

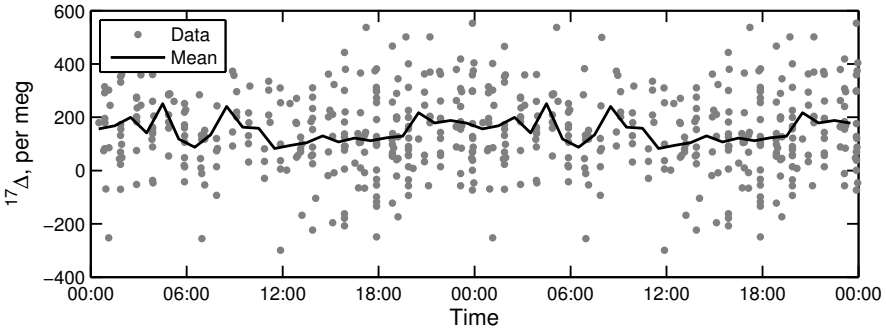

Figure 5.5: $^{17}\Delta$ data plotted onto one day. The black line shows the mean of the data at every hour. The same 24-hour period is shown twice. There is no clear diurnal trend.

The resulting timeseries is shown in Figure 5.4. The data are very noisy, and there are no obvious trends over time. To determine whether a diurnal cycle was resolvable, the data were bin-averaged by hour of the day, as shown in Figure 5.5. A daily cycle is not clearly resolvable in the data.

From the data, we calculate the mean $^{17}\Delta$: 145.7 $\pm$ 9.0 per meg. The data were also split into different subsets for comparison, as shown in Table 5.2. In Chapter 4, we showed that O_2 had a daily maximum around 18:00, and a minimum around 6:00. Therefore, we split the $^{17}\Delta$ data into daytime and nighttime values using windows of noon-midnight and midnight-noon. We also looked at the mean before and after July 12, because in Chapter 4, we showed that this date marked a transition from higher to lower production. An ANOVA comparison of these means revealed that the means are not significantly different from each other at

Table 5.2: Mean $^{17}\Delta$ for all the data and for subsets of the data, described in the text. An ANOVA comparison revealed that the differences in the means of the subsets are not statistically significant at the 95% confidence level.

Data subset	Mean $^{17}\Delta$ ± standard error (per meg)
All	145.7 ± 9.0
Midnight-noon	156.2 ± 14.6
Noon-midnight	139.0 ± 11.6
Before July 12	151.9 ± 11.4
After July 12	134.7 ± 15.0

the 95% confidence level.

5.4.2 Modeled $^{17}\Delta$

The parameters in the diurnal cycle model were fit to the observed mean diurnal cycle of O_2 and $\delta^{18}O$, as explained in Chapter 4. These fits constrained most of the parameters in Equation 5.10, with the best-fit values shown in Table 5.3. The remaining parameter that could be used to fit the observed $^{17}\Delta$ is the $^{17}\Delta$ of the mixing endmember ($^{17}\Delta_m$). Because we could not resolve a diurnal cycle in the $^{17}\Delta$ data, we found the $^{17}\Delta_m$ that best fit the mean of the data (Figure 5.6). If we define $^{17}\Delta_{eq}$ as the value that would be measured using the equilibrator (where the equilibrium fractionation is removed), and $^{17}\Delta_{dis}$ as the dissolved value, the value of $^{17}\Delta_{m,dis}$ was found to be 152.4-155.6 per meg ($^{17}\Delta_{m,eq}$ = 139.0-142.3 per meg). The modeled diurnal cycle in $^{17}\Delta$ has an amplitude of 11 per meg, with a phase that matches that of O_2 and $\delta^{18}O$. A cycle of this amplitude would have been too small to be resolved from our data, given the standard error of 9-15 per meg (Table 5.2).

The relationship between the modeled $\delta^{18}O$ and $\delta^{17}O$ is nearly perfectly linear, and the slope of this model output was found to be 0.5116 ± 0.0002. Like the slope of the data (Figure 5.3), this slope is less than the respiration slope because of the effect of photosynthesis.

Table 5.3: Best-fit parameters for various cases. Numbers in bold were set using model runs in Chapter 4, and $^{17}\Delta_m$ was fit using the mean observed $^{17}\Delta$.

Variable	Case 1	Case 2	Case 3
h (m)	**2.5**	**2.5**	**2.5**
M (m day^{-1})	**6.86**	**6.86**	**6.86**
P_{500} (mmol O_2 m^{-3} hr^{-1})	**4.73**	**4.73**	**4.73**
P/R	**4.44**	**1.64**	**1.01**
C_m (%)	**100**	**103**	**106**
$\delta^{18}O_m$ (per mil)	**-0.42**	**-1.02**	**-1.58**
α_r	**0.9803**	**0.9803**	**0.9803**
α_p	**1.004**	**1.004**	**1.004**
u (m s^{-1})	**2.47**	**2.47**	**2.47**
$^{17}\Delta_m$ (per meg)	155.6	154.0	152.4

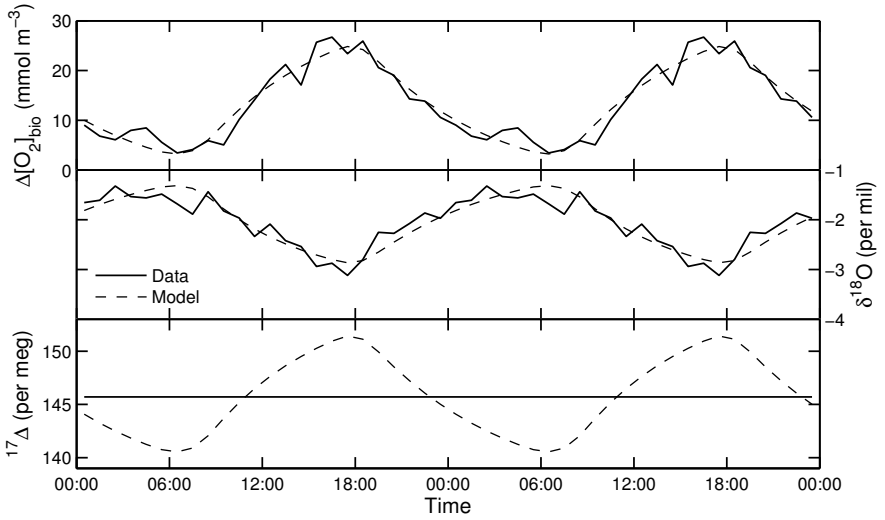

Figure 5.6: Data (solid line) and model results (dashed line) for biological O_2, $\delta^{18}O$, and $^{17}\Delta$. Because the $^{17}\Delta$ data did not show a diurnal cycle, the overall mean value (145.7 per meg) is plotted instead.

5.4.3 Production calculations

The $^{17}\Delta$ of dissolved O_2 can be used to determine gross primary production. Standard methods for calculating GPP from $^{17}\Delta$ assume a steady state, with no upwelling or advection. Although we have shown that mixing plays an important role in the oxygen dynamics at the SIO pier on daily timescales (Chapter 4), we use our measurements to calculate GPP using the steady state method, for comparison with previous studies.

The ratio between GPP and air-sea gas exchange can be expressed as (Luz and Barkan, 2000; Hendricks et al., 2004):

$$\frac{G}{kC_{sat}} = \frac{^{17}\Delta_{sat} - ^{17}\Delta_{dis}}{^{17}\Delta_{dis} - ^{17}\Delta_{w}} \tag{5.12}$$

where G is GPP, C_{sat} is the oxygen concentration at saturation, and $^{17}\Delta_{sat}$ and $^{17}\Delta_{w}$ are defined in Section 5.3, and have values of 13.34 per meg and 249 per meg, respectively. $^{17}\Delta_{dis}$ is the value of dissolved $^{17}\Delta$. For k, we use the wind speed parameterization used in the model, with a mean wind speed of 2.47 m s^{-1}.

The net community production (N) can be determined using measurements of O_2/Ar (Hendricks et al., 2004). O_2/Ar can be used to compute biological oxygen saturation, as explained in Chapter 4, which is used for C/C_{sat}:

$$N = kC_{sat}\left(\frac{C}{C_{sat}} - 1\right) \tag{5.13}$$

The ratio of net to gross production is then:

$$\frac{N}{G} = \left(\frac{C}{C_{sat}} - 1\right)\frac{^{17}\Delta_{dis} - ^{17}\Delta_{w}}{^{17}\Delta_{sat} - ^{17}\Delta_{dis}} \tag{5.14}$$

Recent studies (Prokopenko et al., 2011; Luz and Barkan, 2011) have shown that even in the context of steady-state and no upwelling or mixing, Equations 5.12 and 5.14 are approximations, and the exact equation can be written in terms of $\delta^{17}O$ and $\delta^{18}O$, rather than $^{17}\Delta$. The exact equation for GPP is:

$$\frac{G}{kC_{sat}} = \frac{\left(1 - \frac{\delta^{17}O_{sat}+1}{\delta^{17}O_{dis}+1}\right) - 0.518\left(1 - \frac{\delta^{18}O_{sat}+1}{\delta^{18}O_{dis}+1}\right)}{\left(\frac{\delta^{17}O_{p}+1}{\delta^{17}O_{dis}+1} - 1\right) - 0.518\left(\frac{\delta^{18}O_{p}+1}{\delta^{18}O_{dis}+1} - 1\right)} \tag{5.15}$$

Values of $\delta^x O_{sat}$ are given in Table 5.1. For $\delta^{17}O_p$ and $\delta^{18}O_p$, the values of photosynthetically produced O_2, we use the mean values determined in Luz and Barkan (2011): -10.126 per mil and -20.014 per mil, respectively. This equation can be used with Equation 5.13 to obtain N/G.

We compute G/kC_{sat}, G, N, and N/G using the best fitting "mixing endmember" values from our model ($\delta^{18}O_m$, $\delta^{17}O_m$, and $^{17}\Delta_m$). We take these values to be representative of the mixed layer. Therefore, the resulting values of G and N give production integrated over the mixed layer.

Table 5.4 shows the calculated production using the approximation and the exact equation, for the three model cases in Table 5.3. As explained in Chapter 4, the endmember concentrations were not well constrained, so we use a range of values presented in Chapter 4. As shown in Table 5.4, the approximate and exact equations yield very similar results. The results suggest that gross production in the mixed layer is around 6.7-7.4 mmol O_2 m^{-2} hr^{-1}, and net production is 0-0.28 mmol O_2 m^{-2} hr^{-1}.

5.5 Discussion

Data from the surface ocean near the SIO pier reveal a mean $^{17}\Delta_{eq}$ of 145.7 $\pm$ 9.0 per meg ($^{17}\Delta_{dis}$ = 159.0 per meg). Other studies have shown that the $^{17}\Delta$ of surface water tends to be close to the equilibrium value, due to air-sea gas exchange. For example, $^{17}\Delta$ in the surface ocean of the North Pacific Subtropical Gyre is around 20-40 per meg (Juranek and Quay, 2005), $^{17}\Delta$ in the Southern Ocean is around 20-60 per meg (Hendricks et al., 2004; Reuer et al., 2007), and $^{17}\Delta$ in the subtropical and tropical Pacific Ocean is around 20-80 per meg (Juranek and Quay, 2010). Our measurements tend to have better agreement with measurements of $^{17}\Delta$ below the mixed layer (e.g. Hendricks et al., 2005; Juranek and Quay, 2005; Quay et al., 2010), where the water is not influenced by air-sea gas exchange, but there is still enough light for photosynthesis. However, these studies show data from the open ocean. Other studies of surface water close to shore (Sagami Bay, Japan) show values up to 155 per meg, with the highest values closest to shore

Table 5.4: Gross and net production in the mixed layer, calculated using Equations 5.12-5.15, for a range of mixing endmember gas compositions.

Model case	C_m (%)	$\delta^{18}O_{m,dis}$ (per mil)	$\delta^{17}O_{m,dis}$ (per mil)	$^{17}\Delta_{m,dis}$ (per meg)	G/kC_{sat} (approx.)	G/kC_{sat} (exact)	G^a (approx.)	G^a (exact)	N^a	N/G (approx.)	N/G (exact)
1	100%	-0.42	-0.06	155.64	1.52	1.60	7.07	7.41	0	0	0
2	103%	-1.02	-0.37	153.98	1.48	1.51	6.87	7.00	0.14	0.02	0.02
3	106%	-1.58	-0.67	152.42	1.44	1.44	6.68	6.67	0.28	0.04	0.04

[a] Units in mmol O_2 m^{-2} hr^{-1}.

(Sarma et al., 2005, 2008). Therefore, our high values of $^{17}\Delta$ in the surface ocean could be a reflection of our distance from shore.

Some studies have made observations at high enough frequency to detect changes in $^{17}\Delta$ on diurnal timescales. In Sagami Bay, the measured $^{17}\Delta$ varied by 25 per meg over the course of a day (Sarma et al., 2005). Measurements near a coral reef near Eilat, Israel, show daytime values that are 80 per meg higher than nighttime values (Luz and Barkan, 2009). Our model of O_2 and oxygen isotopes suggests, based on our measurements of dissolved O_2 and $\delta^{18}O$, that $^{17}\Delta$ at the SIO pier should have had a diurnal cycle with an amplitude of 11 per meg. However, we could not resolve a diurnal cycle from our $^{17}\Delta$ data, possibly due to the high noise in the mass spectrometer.

Using the diurnal cycle model, we find that the mixing endmember of $^{17}\Delta$ is 152-156 per meg. We take this to be the mixed layer value, and calculate GPP based on this value. Using the modeled mixing endmember values of $^{17}\Delta$ and biological O_2 saturation, we find a GPP of 6.7-7.4 mmol O_2 m^{-2} hr^{-1} (160.8-177.6 mmol O_2 m^{-2} day^{-1}) and an NCP of 0-0.3 mmol O_2 m^{-2} hr^{-1} (0-7.2 mmol O_2 m^{-2} day^{-1}). These results are similar to summertime $^{17}\Delta$-based measurements of GPP in Sagami Bay, Japan (188-354 mmol O_2 m^{-2} day^{-1}, Sarma et al., 2005), as well as summertime measurements near Hawaii (70-185 mmol O_2 m^{-2} day^{-1}, Juranek and Quay, 2005).

The standard calculations of GPP from $^{17}\Delta$ assume that the water is isolated from deeper water, and do not take vertical mixing into account. Previous studies have often limited their calculations to areas that are believed to be isolated from deeper water (e.g. away from upwelling regions, Hendricks et al., 2005). However, recent studies have used models to account for the effect of mixing or entrainment on the calculation of GPP from $^{17}\Delta$ (Juranek and Quay, 2010; Nicholson et al., 2012). Profiles of $^{17}\Delta$ show that $^{17}\Delta$ can be higher at depth than at the surface (e.g. Hendricks et al., 2005; Juranek and Quay, 2005; Quay et al., 2010). Therefore, upwelling or vertical mixing would enhance surface $^{17}\Delta$, causing an overestimate of GPP. Juranek and Quay (2010) showed that in the upwelling region at the equator, not accounting for mixing overestimated the production by

less than 15%. However, Nicholson et al. (2012) showed that not accounting for vertical mixing at the Hawaii Ocean Time-series and Bermuda Atlantic Time-series sites overestimated GPP by 60-80%. Because we do not have measurements of $^{17}\Delta$ at depth, it is unknown how much mixing would affect our results, but, based on these studies, it is likely that our calculated GPP is an overestimate.

Vertical mixing could also affect the calculation of net production in the mixed layer based on the biological oxygen saturation. Equation 5.13 assumes that water with a biological oxygen saturation of 100% has zero net production. This is true of water that has been influenced only by air-sea gas exchange, and is isolated from deeper water. Air-sea gas exchange forces biological oxygen saturation to 100%, so deviations from 100% biological oxygen saturation are due to net production. However, water upwelling into the euphoric zone from depth would start with a biological oxygen saturation below 100%. As photosynthesis occurs in this water, the biological oxygen saturation will increase. However, the biological oxygen saturation could remain below 100%, even though there was net production, because air-sea gas exchange would not yet have forced the saturation to 100%. Therefore, upwelling or vertical mixing could cause an underestimate in the net production, which could explain the low values that we calculate here.

In Chapter 4, we estimated production rates using the observed diurnal cycle in O_2 and $\delta^{18}O$. If this production, averaged over 24 hours, is integrated to a mixed layer depth of 50 m, the production is 107.13 mmol O_2 m^{-2} hr^{-1}. For the production derived from the O_2 cycle to match the production derived from $^{17}\Delta$, the mixed layer would have to be only 3.5 m deep. The higher production calculated from the diurnal cycle in O_2 suggests that production in the nearshore surface ocean is not representative of the entire mixed layer.

5.6 Conclusions

In this chapter, we explain corrections needed to measure $^{17}\Delta$. Measurements of $^{17}\Delta$ require a correction for nonlinearity of the mass spectrometer. In addition, our particular mass spectrometer required filtering of the data to remove

noise from the m/z 33 collector. Measurements in the surface ocean at the SIO pier give a mean $^{17}\Delta_{eq}$ of 145.7 per meg ($^{17}\Delta_{dis}$ = 159.0 per meg). A diurnal cycle in $^{17}\Delta$ was not observed, possibly due to high noise in the mass spectrometer. However, a model of dissolved O_2 and oxygen isotopes suggests that the diurnal cycle in $^{17}\Delta$ would have been 11 per meg. Using our model-derived value of $^{17}\Delta$ in the mixed layer, we find a GPP of 6.7-7.4 mmol O_2 m^{-2} hr^{-1}.

5.7 Acknowledgements

We thank Michael Bender for helpful discussions about measuring $^{17}\Delta$.

This chapter, in part, is being prepared for publication. Lauren Elmegreen Rafelski, Bill Paplawsky, and Ralph F. Keeling. I am the primary investigator and author of this paper.

References

Angert, A., Rachmilevitch, S., Barkan, E., and Luz, B., 2003: Effects of photorespiration, the cytochrome pathway, and the alternative pathway on the triple isotopic composition of atmospheric O_2. *Global Biogeochemical Cycles*, **17**(1), 1030, doi:10.1029/2002GB001933.

Benson, B. B., and Krause, D., Jr., 1980: The concentration and isotopic fractionation of gases dissolved in freshwater in equilibrium with the atmosphere. 1. Oxygen. *Limnology and Oceanography*, **25**(4), 662–671.

Hamme, R. C., Cassar, N., Lance, V. P., Vaillancourt, R. D., Bender, M. L., Strutton, P. G., Moore, T. S., DeGrandpre, M. D., Sabine, C. L., Ho, D. T., and Hargreaves, B. R., 2012: Dissolved O_2/Ar and other methods reveal rapid changes in productivity during a Lagrangian experiment in the Southern Ocean. *Journal of Geophysical Research*, **117**(C00F12), doi:10.1029/2011JC007046.

Hendricks, M. B., Bender, M. L., and Barnett, B. A., 2004: Net and gross O_2 production in the Southern Ocean from measurements of biological O_2 saturation and its triple isotope composition. *Deep-Sea Research I*, **51**, 1541–1561.

Hendricks, M. B., Bender, M. L., Barnett, B. A., Strutton, P., and Chavez, F. P., 2005: Triple oxygen isotope composition of dissolved O_2 in the equatorial Pacific: A tracer of mixing, production, and respiration. *Journal of Geophysical Research*, **110**(C12021), doi:10.1029/2004JC002735.

Juranek, L. W., and Quay, P. D., 2005: In vitro and in situ gross primary and net community production in the North Pacific Subtropical Gyre using labeled and natural abundance isotopes of dissolved O_2. *Global Biogeochemical Cycles*, **19**(GB3009), doi:10.1029/2004GB002384.

Juranek, L. W., and Quay, P. D., 2010: Basin-wide photosynthetic production rates in the subtropical and tropical pacific ocean determined from dissolved oxygen isotope ratio measurements. *Global Biogeochemical Cycles*, **24**(GB2006), doi:10.1029/2009GB003492.

Luz, B., and Barkan, E., 2000: Assessment of oceanic productivity with the triple-isotope composition of dissolved oxygen. *Science*, **288**, 2028–2031.

Luz, B., and Barkan, E., 2005: The isotope ratios $^{17}O/^{16}O$ and $^{18}O/^{16}O$ in molecular oxygen and their significance in biogeochemistry. *Geochimca et Cosmochimica Acta*, **69**(5), 1099–1110.

Luz, B., and Barkan, E., 2009: Net and gross oxygen production from O_2/Ar, $^{17}O/^{16}O$ and $^{18}O/^{16}O$ ratios. *Aquatic Microbial Ecology*, **56**, 133–145.

Luz, B., and Barkan, E., 2011: Proper estimation of marine gross O_2 production with $^{17}O/^{16}O$ and $^{18}O/^{16}O$ ratios of dissolved O_2. *Geophysical Research Letters*, **38**(L19606), doi:10.1029/2011GL049138.

Luz, B., Barkan, E., Bender, M. L., Thiemens, M. H., and Boering, K. A., 1999: Triple-isotope composition of atmospheric oxygen as a tracer of biosphere productivity. *Nature*, **400**, 547–550.

Nicholson, D. P., Stanley, R. H. R., Barkan, E., Karl, D. M., Luz, B., Quay, P. D., and Doney, S. C., 2012: Evaluating triple oxygen isotope estimates of gross primary production at the Hawaii Ocean Time-series and Bermuda Atlantic Time-series Study sites. *Journal of Geophysical Research*, **117**(C05012), doi:10.1029/2010JC006856.

Prokopenko, M. G., Pauluis, O. M., Granger, J., and Yeung, L. Y., 2011: Exact evaluation of gross photosynthetic production from the oxygen triple-isotope composition of O_2: Implications for the net-to-gross primary production ratios. *Geophysical Research Letters*, **38**(L14603), doi:10.1029/2011GL047652.

Quay, P., Stutsman, J., and Steinhoff, T., 2012: Primary production and carbon export rates across the subpolar N. Atlantic Ocean basin based on triple oxygen isotope and dissolved O_2 and Ar gas measurements. *Global Biogeochemical Cycles*, **26**(GB2003), doi:10.1029/2010GB004003.

Quay, P. D., Peacock, C., Björkman, K., and Karl, D. M., 2010: Measuring primary production rates in the ocean: Enigmatic results between incubation and non-incubation methods at station ALOHA. *Global Biogeochemical Cycles*, **24**(GB3014), doi:10.1029/2009GB003665.

Reuer, M. K., Barnett, B. A., Bender, M. L., Falkowski, P. G., and Hendricks, M. B., 2007: New estimates of Southern Ocean biological production rates from O_2/Ar ratios and the triple isotope composition of O_2. *Deep-Sea Research I*, **54**, 951–974.

Sarma, V. V. S. S., Abe, O., Hashimoto, S., Hinuma, A., and Saino, T., 2005: Seasonal variations in triple oxygen isotopes and gross oxygen production in the Sagami Bay, central Japan. *Limnology and Oceanography*, **50**(2), 544–552.

Sarma, V. V. S. S., Abe, O., and Saino, T., 2008: Spatial variations in time-integrated plankton metabolic rates in Sagami Bay using triple oxygen isotopes and O_2:Ar ratios. *Limnology and Oceanography*, **53**(5), 1776–1783.

Stanley, R. H. R., Kirkpatrick, J. B., Cassar, N., Barnett, B. A., and Bender, M. L., 2010: Net community production and gross primary production rates in the western equatorial Pacific. *Global Biogeochemical Cycles*, **24**(GB4001), doi:10.1029/2009GB003651.

Thiemens, M. H., Jackson, T., Zipf, E. C., Erdman, P. W., and van Egmond, C., 1995: Carbon dioxide and oxygen isotope anomalies in the mesosphere and stratosphere. *Science*, **270**(5238), 969–972.

Wanninkhof, R., 1992: Relationship between wind speed and gas exchange over the ocean. *Journal of Geophysical Research*, **97**(C5), 7373–7382.

Chapter 6

Climate effects on atmospheric carbon dioxide over the last century

6.1 Introduction

Records from the Scripps Institution of Oceanography indicate that the global average CO_2 concentration (based on an average of Mauna Loa and the South Pole) increased from 315 ppm in 1958 to 383 ppm in 2008. Over this period, the airborne fraction computed as a ratio of CO_2 buildup to industrial emissions (fossil fuel plus cement, which we will refer to as fossil fuel emissions) amounts to 57%. In Figure 6.1, we show the atmospheric CO_2 record against the cumulative fossil fuel emissions scaled to 57%, following Keeling et al. (1995). Also following Keeling et al. (1995), we detrend the record using this constant airborne fraction (Figure 6.1B) to produce an anomaly that we refer to as the constant airborne fraction (CAF) anomaly. From 1958 to the present, the CAF anomaly remains very small, never exceeding 2 ppm, although larger anomalies were present earlier. Similarly, the 2007 IPCC report (Denman et al., 2007) shows that since 1958, the airborne fraction has remained highly constant when averaged for periods of 5 years or more.

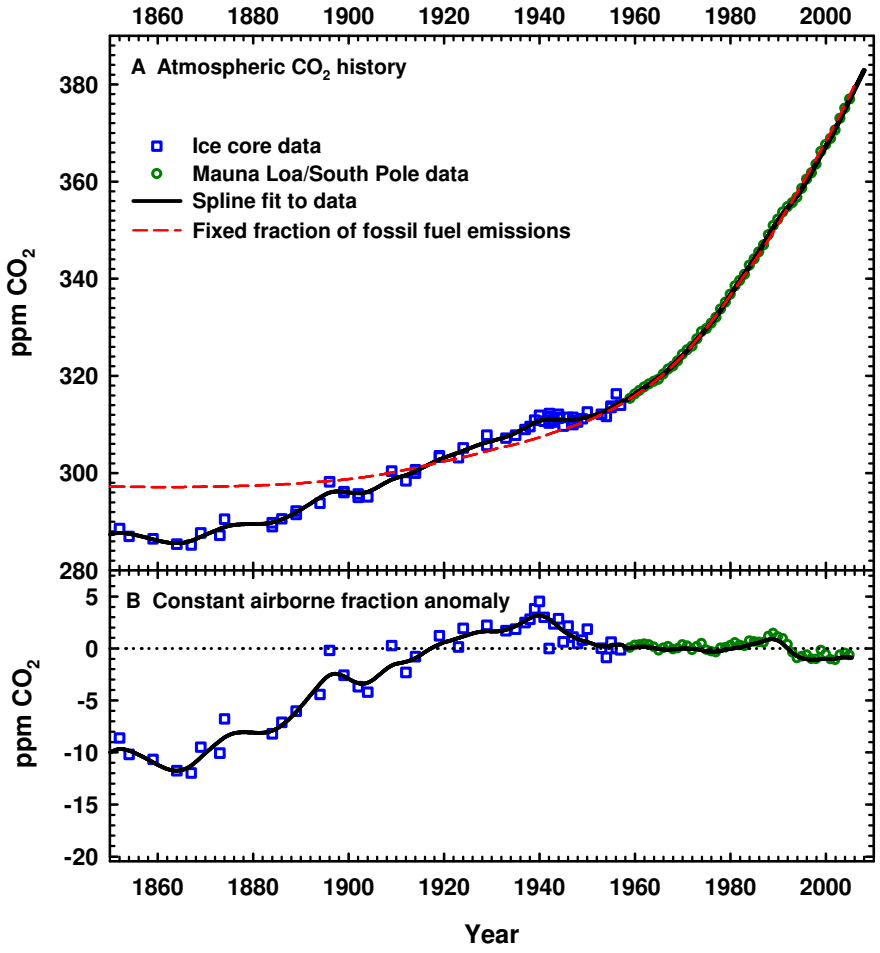

Figure 6.1: A. Atmospheric CO_2 record based on ice core data before 1958, (Etheridge et al., 1996; MacFarling Meure et al., 2006) and yearly averages of direct observations from Mauna Loa and the South Pole after 1958 (from the Scripps CO_2 program). Also shown is a spline fit to the record and a curve depicting 57% of cumulative industrial (fossil fuel and cement) emissions (Marland et al., 2006). B. Constant airborne fraction anomaly, computed by taking the difference between the atmospheric record and 57% of fossil fuel emissions.

The virtual constancy of the airborne fraction since 1958 requires that the sum of the global carbon sinks and any additional sources (such as CO_2 release from land use) has increased in proportion to fossil fuel emissions. Two major sink processes are expected to respond directly to rising CO_2: ocean CO_2 uptake and CO_2 fertilization of plant growth (DeLucia et al., 1999). However, even if these were the only sink processes, one would expect a constant airborne fraction only if fossil fuel emissions grow at a constant rate per year (Bacastow and Keeling, 1979; Oeschger and Heimann, 1983). In 1980, the growth rate of fossil fuel emissions decreased from ∼4.3% per year to ∼1.5% per year, as shown in Figure 6.2. This decrease should have caused the airborne fraction to decrease, because carbon sinks are less limited by kinetic barriers when atmospheric CO_2 is rising more slowly. Keeling et al. (1995) suggested that the constancy of the airborne fraction before and after 1980 might result from carbon exchanges driven by climate changes, noting similarities between decadal variations in carbon dioxide and decadal anomalies in global temperature. Carbon sink modeling studies (Dai and Fung, 1993; Houghton, 1995; Cramer et al., 2001) also suggest a link between climate change and carbon exchange, showing that CO_2 releases are associated with periods of warming.

On short timescales, the growth rate of atmospheric CO_2 is far more variable than fossil fuel emissions, reflecting large exchanges of carbon from the land biosphere associated with El Niño events and other short term climate forcing (Keeling et al., 1995). Recent work implicates biomass burning as a potentially large source of this variability (Langenfelds et al., 2002; van der Werf et al., 2004; Randerson et al., 2005). It is unclear if the climate processes involved in this shorter-term variability are also relevant on longer time scales.

Prior to 1958, the growth rate of CO_2 was less closely tied to fossil fuel emissions. Figure 6.1 shows the most detailed available ice core CO_2 record, from Law Dome, Antarctica (Etheridge et al., 1996; MacFarling Meure et al., 2006), which we use to extend the atmospheric record back to 1850. As is well known, atmospheric CO_2 rose from 1850 to 1900 at a faster rate than expected from fossil fuel emissions (Figure 6.1A). During this time period, CO_2 was rising in response

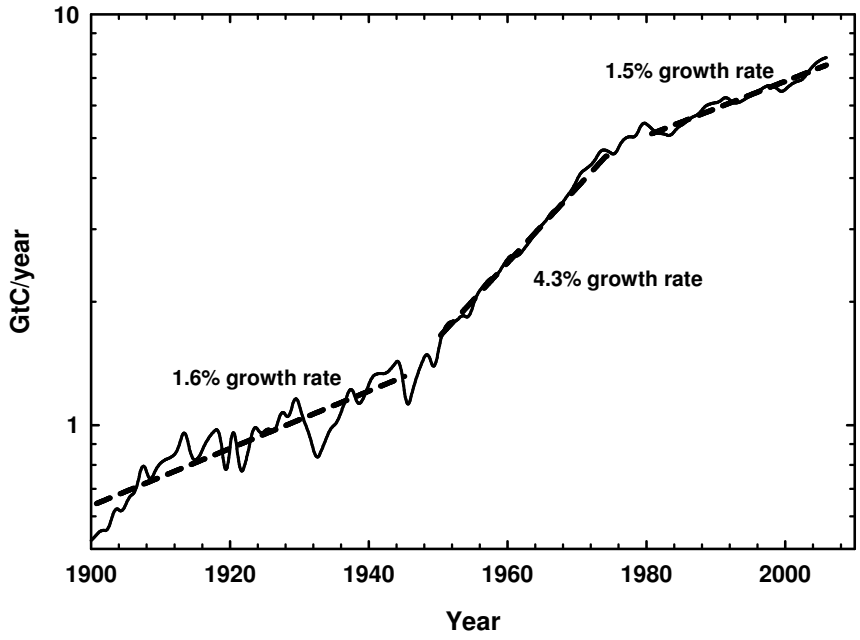

Figure 6.2: Fossil fuel emissions per year, plotted on a log scale. The approximate growth rates in fossil fuel emissions from 1900-1950, 1950-1980, and 1980-present are also plotted.

to another CO_2 source, most likely emissions from land use changes (Pearman et al., 1986; Siegenthaler and Oeschger, 1987). During the 1940s, the CO_2 buildup stalled in spite of fossil fuel emissions that were at least as high as in previous years.

The near constancy of the airborne fraction since 1958 is all the more striking when compared to these large earlier fluctuations. Until these contrasting behaviors can be understood, it may be difficult to develop reliable forecasts of future variations in the airborne fraction, and hence future atmospheric CO_2 loading. A particular concern is that warming may trigger additional carbon releases, which may amplify global warming in a positive feedback loop (Cox et al., 2000).

Here we explore the carbon sinks since 1850 using the atmospheric mass balance:

$$\Delta CO_2 = F + LU - O - B \tag{6.1}$$

where F is fossil fuel emissions, LU is land use CO_2 emissions, O is the ocean sink, and B is the residual land flux. We solve Equation 6.1 for the time-varying term B, using specified time variations in the other terms, in a calculation known as a "single deconvolution." The residual land exchange calculated this way includes the contributions from all land processes other than land use, and from errors in the F, LU, and O terms. We compare estimates of this residual land exchange with calculations from a two-box biospheric model, to assess the potential for any unexpected trends. Following Keeling et al. (1995) this approach emphasizes the need for the inclusion of processes that are tied to changes in global climate on decadal timescales.

6.2 Methods

6.2.1 Description of data

We use the fossil fuel emissions record from Marland et al. (2006), which includes yearly values from 1751 until 2003. CO_2 emissions from cement manufacturing are included in these values. Emissions are extrapolated to 2006 using

data from the BP Statistical Review of World Energy (BP, 2008), and are linearly interpolated to monthly resolution.

We use estimates of land use CO_2 emissions from 1850 to 2000 from Houghton (2003). The emissions are extrapolated to 2006 by assuming that yearly emissions stayed constant after the year 2000. Land use emission estimates are uncertain to the 50% level (Houghton, 2003), with the highest uncertainties in tropical regions (House et al., 2003; Jain and Yang, 2005). Satellite studies suggest that the Food and Agriculture Organizations (FAO) records of land use change, used by Houghton, may have overestimated the amount of deforestation in the tropics, thereby overestimating tropical emissions (Achard et al., 2002; DeFries et al., 2002). We therefore regard the estimates of Houghton as an upper bound on land use emissions ("high land use emissions" case). To allow for uncertainty in land use, we also consider a low land use emissions case in which, for simplicity, we set the tropical emissions to zero while adopting the extratropical emissions from Houghton. We regard this low land use case as an extreme lower bound. This low land use case is also more similar in shape to land use fluxes modeled by terrestrial biosphere models (McGuire et al., 2001). For the low land use case, emissions were nearly zero at the year 2000. In this case, the global land use flux was assumed to be zero after the year 2000. Fluxes for both cases were linearly interpolated to monthly resolution.

We use a global CO_2 record based on a combination of the ice core record from Law Dome before 1958 (Etheridge et al., 1996; MacFarling Meure et al., 2006) and a seasonally detrended arithmetic average of monthly air measurements from Mauna Loa and the South Pole from the Scripps CO_2 program after 1958 (Figure 6.1). The records were combined without adjustment. The ice core data are approximated to monthly resolution using a spline with a standard error, σ, of 0.6 ppm CO_2.

6.2.2 Ocean model

To represent the oceanic uptake of CO_2, we use a rescaled version of the mixed-layer pulse response function based on the HILDA model, from Joos et al.

(1996). We ran the pulse response function model starting at the year 1800 using a one-month time step, and integrated the yearly uptake values to determine the net uptake since 1800. We rescaled the results by multiplying by a constant to achieve 118 PgC for the integrated uptake from 1800 to 1994, consistent with Sabine et al. (2004). Sabine's results are in good agreement with uptake estimates based on the observed trends in atmospheric O_2 concentration (Manning and Keeling, 2006).

In fact, Joos et al. (1996). developed pulse response functions not just for the HILDA model, but also for three additional models: a box diffusion model, a 2-D ocean general circulation model (OGCM), and the Princeton 3-D OGCM. We found, however, that the differences between these models were very small once they were rescaled to achieve the same integrated uptake from 1800 to 1994: the yearly oceanic uptakes differed by at most 0.07 PgC yr^{-1}, and the integrated ocean uptake through 2005 differed by at most 0.5 PgC, with the biggest difference occurring between the 3-D model and the other models around 1960.

To allow for uncertainty in oceanic uptake of CO_2, we consider several alternate cases. First, we allow for uncertainty in the Sabine constraint by scaling the ocean uptake uniformly by 30% (high ocean uptake or low ocean uptake). Second, we allow for possible climate effects on ocean uptake by allowing for changes in sea surface temperature (SST) on equilibrium carbon chemistry. We modify the pulse response formulation of Joos et al. so that pCO_2 is computed from the full DIC concentration, not just the perturbation since preindustrial times. This is necessary because changes in SST affect all of the carbon in the mixed layer, not just the perturbation. We use a global SST record since 1850 (Brohan et al., 2006) to drive the ocean model.

This model does not consider the effects of climate change on ocean biology or circulation. However, more complex ocean models suggest that their effects are small globally (Le Quéré et al., 2007) or would lead to uptake intermediate to the cases we consider (Plattner et al., 2001).

6.2.3 Land model

As a simple depiction of the land biosphere, we use a two-box model. The model uses a 1477 PgC box with a 60 year turnover time and a 110 PgC box with a 2.5 year turnover time, as shown in Figure 6.3. The turnover times are consistent with the turnover times of a two-box model used by Bacastow and Keeling (1973). The large box size is from the one-box model used by Keeling et al. (1989), and the small box size is from the short lived biota box of a more complex model presented by Bolin (1986). The total size of our land box differs from that presented in the 2007 IPCC report (Denman et al., 2007). However, as explained below, although the turnover times are important in determining the magnitude of the fluxes, the box sizes are less important, as they are redundant with other parameters once the model is fit to observations.

Prior studies using box models have typically used CO_2 fertilization to drive the land uptake (Keeling et al., 1989). However, recent work suggests that nitrogen fertilization could be equally or more important (Magnani et al., 2007). Here, we allow for both CO_2 and N fertilization as well as the effects of temperature-dependent respiration. These processes are represented according to:

$$F_{ai} = K_{ai} \times C^o_{atm} \times (1 + \varepsilon \Delta C_{atm}/C^o_{atm} + \gamma ff) \tag{6.2}$$

$$F_{ia} = K_{ia} \times (Q_{10})_i^{(T-T_0)/10} \times (C^o_i + \Delta C_i) \tag{6.3}$$

where F_{ai} (PgC yr^{-1}) is the allocation from net primary production (NPP) to box i (where $i = 1$ or 2) and F_{ia} is the carbon released by heterotrophic respiration or fire from box i to the atmosphere. K_{ai} and K_{ia} (yr^{-1}) are exchange constants (1/turnover time), ΔC_i (PgC) is the change in box i size since 1850, ε is the fertilization factor from increased CO_2 in the atmosphere, γ ((PgC yr^{-1})$^{-1}$) is the fertilization factor from increased nitrogen, ff (PgC yr^{-1}) is fossil fuel emissions, C^o is the initial box size (PgC), and Q_{10} is the factor that the fluxes change for a 10^{o}C temperature change. A global land air temperature record (Brohan et al., 2006) is used to drive the model. The parameterization of N fertilization in Equation 6.2 is based on Townsend et al. (1996), which allows for excess N from fossil

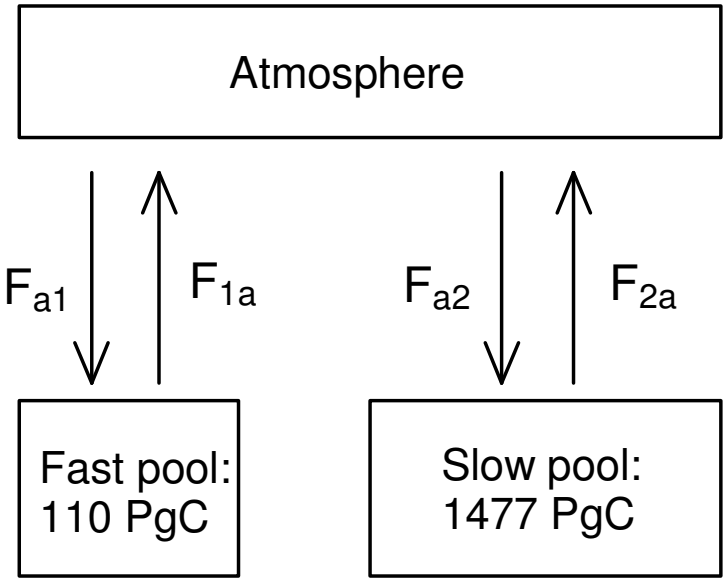

Figure 6.3: Terrestrial two-box model.

fuel combustion. The parameterization implicitly accounts for N fertilization from other anthropogenic sources that have grown over time in proportion to fossil fuel burning. As in Townsend et al., we ignore the potentially large contribution of industrial nitrogen (Galloway and Cowling, 2002) because this nitrogen is mostly applied to agricultural areas, which do not have long-term carbon storage. Equations 6.2 and 6.3 are generalized expressions for the fluxes. We also consider simpler cases in which one or more processes are neglected, for example by setting $\varepsilon = 0$, $\gamma = 0$ or $Q_{10} = 1$.

Previous studies, such as Jones and Cox (2005), have used statistical regressions with timeseries such as the Niño3 index to explore variability in atmospheric CO_2. The two-box model that we use is a more mechanistic approach to understanding variability, allowing for time constants in the response of CO_2 fluxes to forcings. The parameters ε, γ, and Q_{10} are fitted empirically using observed atmospheric CO_2 and carbon emissions records. We find that if we change the box sizes while keeping the time constants the same (not shown), the values of the fitted parameters ε, γ, or Q_{10} change, but the carbon flux over time does not change. For this reason, the chosen box sizes are less important than the turnover times, and the magnitude of fitted parameters do not necessarily have simple physiological significance.

6.3 Results

6.3.1 Residual flux from deconvolution

A standard case for the residual land exchange from the deconvolution (B in Equation 6.1) is shown in Figure 6.4A (green curve), along with associated land use emissions. This standard case uses constant sea surface temperature (SST), high land use emissions, and a central estimate of oceanic CO_2 uptake (CHM - see Table 6.1). The residual flux has been smoothed using a 10-year running mean, to reduce the El Niño scale variability. The residual flux estimate in Figure 6.4A is similar to previous estimates from 1900 on (Houghton, 2007), with differences in the magnitude of the variability before 1900. Our residual flux oscillates around

Table 6.1: Parameters used for calculations of the residual land flux

Case		Description	
	SST	Land Use	Ocean Uptake
CHM	Constant	High	Medium
CLM	Constant	Low	Medium
CHL	Constant	High	Low
CHH	Constant	High	High
CLL	Constant	Low	Low
CLH	Constant	Low	High
VHM	Variable	Low	Medium

Table 6.2: Model Parameters

Parameters		Description
	Fertilization method	Q_{10}
-C	CO_2 only	Defined as 1
-V	CO_2 only	Fit to land air temperature record
-CN	Nitrogen only	Fit to land air temperature record

zero until 1920, after which it increases over time with some notable multidecadal variability. The magnitude of the residual flux is directly tied to the land use emissions. The low land use emissions case (CLM), as shown in Figure 6.4B, yields a residual flux which stays much closer to zero than the high land use emissions case, but the pattern of multidecadal variability is largely unchanged.

6.3.2 Temperature-independent model

We now compare estimates of the residual flux to results from a simple land biosphere model, which consists of the biospheric model driven only by CO_2 fertilization ($\gamma = 0$ and $Q_{10} = 1$). Although here we show results where both boxes respond to fertilization (with the same ε for both boxes), we find that the quality of our fit does not change if only the large box responds to fertilization (results not shown). Both the model output and the residual flux are filtered using a 10-year running mean. A nonlinear least-squares regression analysis is used to find the value of ε that best fits the filtered residual flux over the period from 1900 to 2005. Although the model (Figures 6.4A and 6.4B, black curves) reproduces the long-term uptake of the residual, it does not match the decadal variability. The

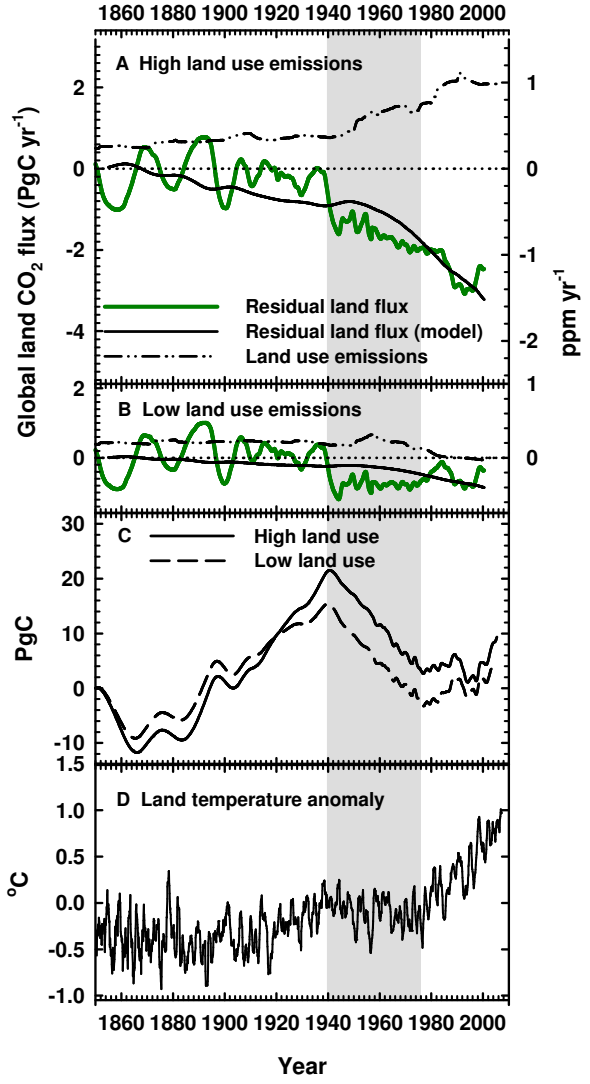

Figure 6.4: Residual land carbon fluxes based on a deconvolution and based on the temperature-independent model. Sources to the atmosphere are plotted as positive, and sinks are plotted as negative. A. The high land use emissions case (CHM-C) and B. the low land use emissions case (CLM-C). C. The integrated difference between the model and residual land fluxes. D. Global land air temperature anomaly relative to the 1961-1990 mean (Brohan et al., 2006). Grey area highlights the period of relatively constant or decreasing global land air temperature from 1940-1976.

model and deconvolution-based residual curves cross each other around 1940 and 1980, with the modeled sink too large before 1940 and after 1980, and too small between 1940 and 1980.

The decadal pattern is also revealed in the time integrated difference between the deconvolution and model shown in Figure 6.4C, which can be expressed as a carbon anomaly in PgC (not to be confused with the CAF anomaly). Because time integration is already a form of low-pass filtering, we compute these anomalies with the 10-year smoothing of the land model output and residual flux removed. For both the high and low land use cases, the anomaly curves have a similar overall shape, with the anomaly rising until 1940, falling until 1976, and then remaining relatively constant (CHM-C) or rising slightly (CLM-C).

The shape of the CO_2 anomaly curves in Figure 6.4C have an obvious similarity to the shape of the global land air temperature record (Brohan et al., 2006) shown in Figure 6.4D, which also has breaks in slope around 1940 and 1976. This similarity supports the findings (Dai and Fung, 1993; Houghton, 1995; Keeling et al., 1995; Cramer et al., 2001) that processes tied to temperature may be responsible for the pattern of multidecadal CO_2 fluxes not accounted for in the model.

As a third way of looking at the CO_2 anomaly of our model, we add the fluxes from fossil fuel emissions, land use change emissions, and ocean uptake to our modeled land uptake (as in Equation 6.1), and integrate the net flux over time, adding an integration constant to achieve the best agreement with the CO_2 record from 1959-1979 (shown for CHM-C in Figure 6.5). We again use a modeled land uptake with the 10-year smoothing removed. To better display small trend differences, we detrend the modeled CO_2 concentration using 57% of fossil fuel emissions, as in Figure 6.1B. Looking at the slopes of the lines in Figure 6.5, the modeled CO_2 is seen to rise too slowly from 1880 to 1940, too rapidly from 1940 to 1980, and too slowly from 1980 to the present compared to observations. The difficulty in matching the constancy in the airborne fraction before and after 1980 in this class of model was noted previously by Keeling et al. (1995).

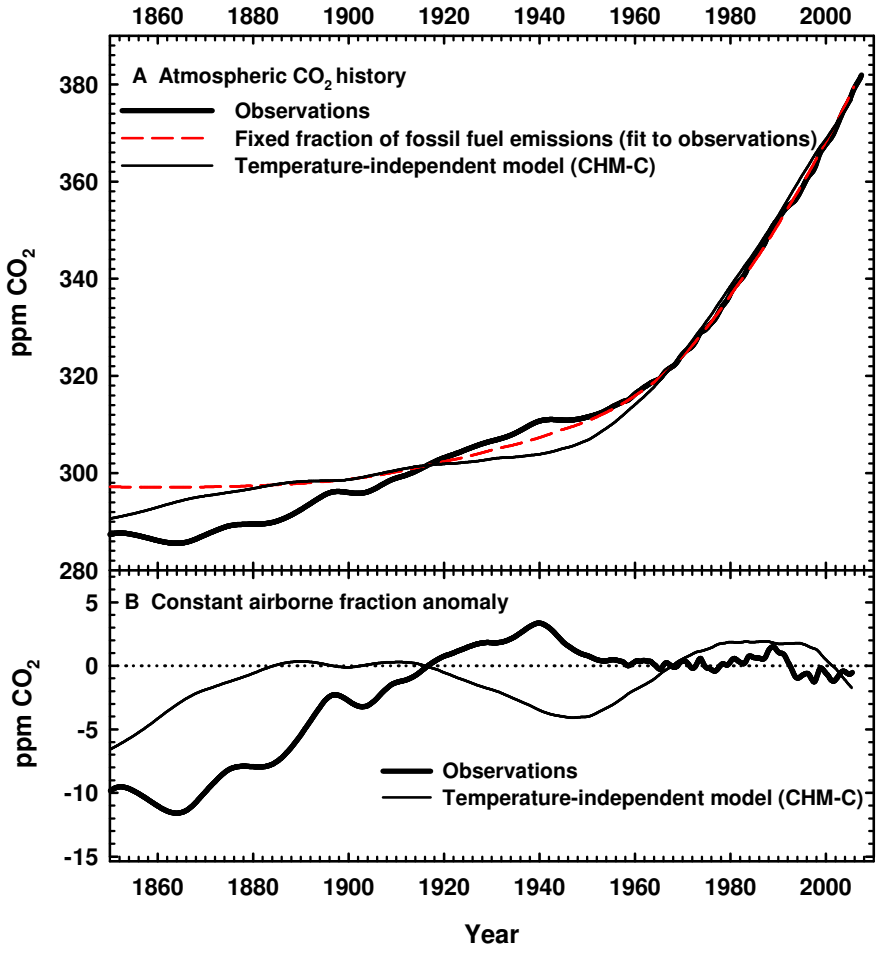

Figure 6.5: A. Atmospheric CO_2 record, atmospheric CO_2 modeled using the temperature-independent model, and a curve depicting 57% of cumulative industrial (fossil fuel and cement) emissions. An integration constant has been added to the modeled atmospheric CO_2 to match observations from 1959-1979. B. Constant airborne fraction anomaly of the atmospheric record and model results, computed by taking the difference between the atmospheric record and 57% of fossil fuel emissions.

6.3.3 Temperature-dependent model

We now repeat the same analysis, allowing for temperature-dependent respiration (relaxing the requirement that $Q_{10} = 1$) driven by changes in the global land air temperature record. We thus now fit both ε and Q_{10}. We find (results not shown) that allowing temperature-dependent respiration in the large land box does not affect the fit. Because of the 60-year time constant of this box, the Q_{10} parameter only influences the long-term flux, which is already optimized by fitting ε. To avoid such redundancy in the fit, we therefore only allow temperature-dependence in the small box, thus setting Q_{10} =1 for the large box, and optimally fitting Q_{10} for the small box. The parameter ε is again fit for both boxes. This two-parameter fit tracks the multidecadal variability more closely (Figure 6.6). When the fossil fuel, land use, and ocean carbon fluxes are added to the modeled residual land flux and integrated over time, we find that the temperature-dependent model does a better job than the temperature-independent model of reproducing the atmospheric CO_2 record from 1920-present (shown for CHM-V in Figure 6.7). In particular, the model now does a better job of reproducing the low growth from 1940 to 1950, and matching the accelerating growth from 1960 to 1980 and from 1980 to the present. In other words, the model does a better job of reproducing the 1940s plateau and the overall constancy of the airborne fraction since 1960. Even with the improved fit, however, the model does not perfectly track the multidecadal variability: the model underestimates the overall CO_2 rise before 1940, predicts a rise that is too rapid in the late 1950s, and over-predicts atmospheric CO_2 concentrations from around 1991 to 2002. These features are discussed further below.

6.3.4 Sensitivity analyses

The analysis in the previous section is subject to uncertainties in the residual land flux that remain to be addressed. The analysis explored uncertainty in land use emissions, but not in ocean uptake, nor did it consider the possibility of nitrogen fertilization.

To address these and other uncertainties, we consider a matrix of different cases, as detailed in Table 6.3. For these cases, we vary the parameters

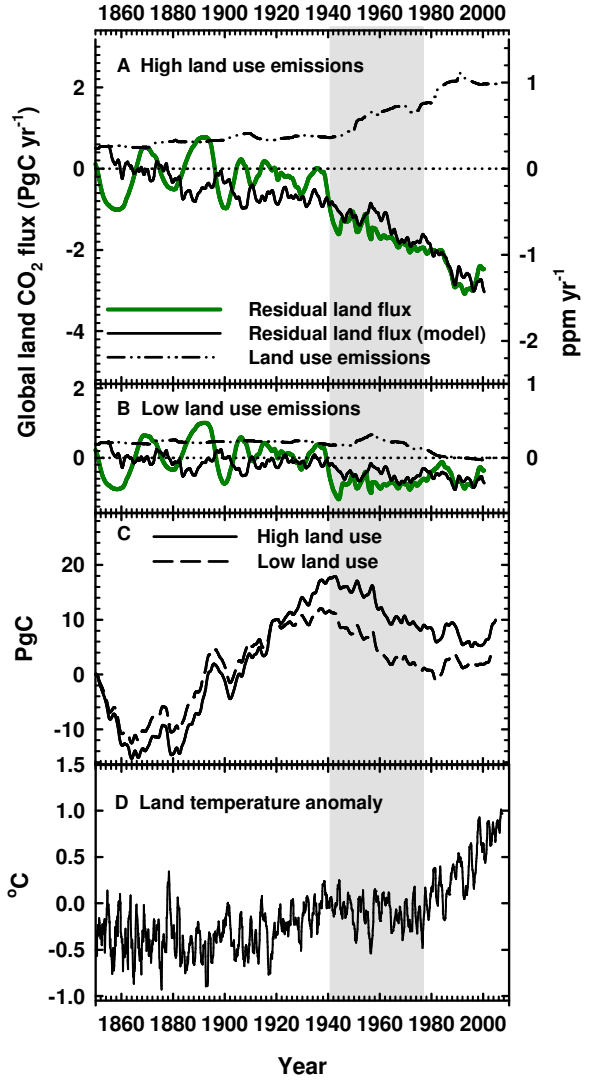

Figure 6.6: Residual land carbon fluxes based on a deconvolution and based on the temperature-dependent model. Sources to the atmosphere are plotted as positive, and sinks are plotted as negative. A. The high land use emissions case (CHM-V) and B. the low land use emissions case (CLM-V). C. The integrated difference between the model and residual land fluxes. D. Global land air temperature anomaly relative to the 1961-1990 mean (Brohan et al., 2006). Grey area highlights the period of relatively constant or decreasing global land air temperature from 1940-1976.

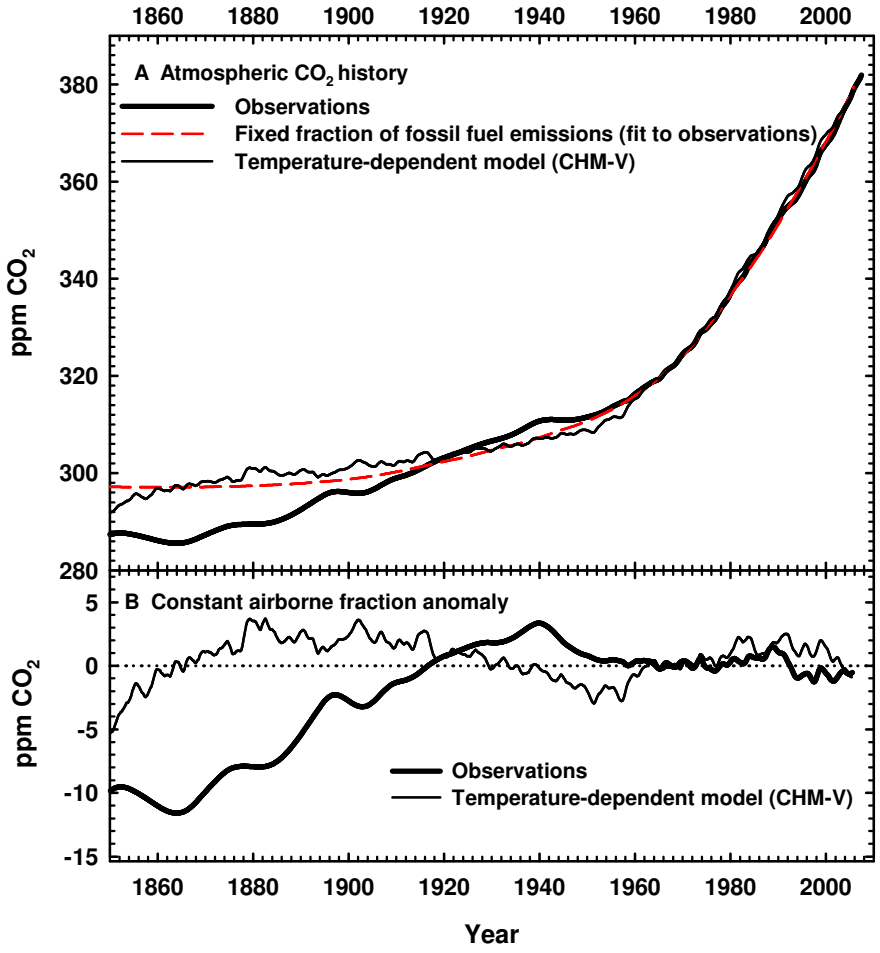

Figure 6.7: A. Atmospheric CO_2 record, atmospheric CO_2 modeled using the temperature-dependent model, and a curve depicting 57% of cumulative industrial (fossil fuel and cement) emissions. An integration constant has been added to the modeled atmospheric CO_2 to match observations from 1959-1979. B. Constant airborne fraction anomaly of the atmospheric record and model results, computed by taking the difference between the atmospheric record and 57% of fossil fuel emissions.

that determine the residual flux, and refit the fertilization parameter for the temperature-independent cases, or the fertilization and temperature parameters for the temperature-dependent cases, as previously. The CO_2 anomaly is again computed based on the difference between the residual flux and the fit.

For the ten temperature-independent model cases, the CO_2 anomaly curve is sensitive to assumptions, but the breaks in slope occur consistently around 1940 and 1976 (shown for six of the ten cases in Figure 6.8A). The only exception is the high land use case using N fertilization (CHM-CN), where the second break moves from 1976 to 1967. When we look at the difference between the modeled CO_2 (computed using Equation 6.1) and 57% of fossil fuel emissions (Figure 6.8B), we see that the variable ocean temperature cases (VHM-C and VLM-C) give similar results as the corresponding constant ocean temperature case (CHM-C and CLM-C). Compared with the standard case (CHM-C, shown also in Figure 6.5B), the nitrogen fertilization and low land use cases are in closer agreement with the observations from 1850 to 1900, but still show too slow a rise from 1900 to 1940.

For the ten temperature-dependent cases, we consistently find improvement compared to the corresponding temperature-independent cases (Table 6.3). The values of Q_{10} and the fertilization parameter for all ten cases are given in Table 6.3. For all of the CO_2 fertilization cases where constant ocean temperature is used, the Q_{10} values are around 4-5 to within error. Allowing for ocean warming reduces the Q_{10} values to around 3. Replacing CO_2 fertilization with N fertilization yields Q_{10} values of 1.5 and 2.8. Better fits are obtained for the low land use cases than the high land use cases. The Q_{10} values for all of the cases are significantly greater than 1, which suggests that despite uncertainties, the CO_2 record contains a clear signature of warming-related releases of CO_2 to the atmosphere on multidecadal timescales. The signature emerges despite the uncertainties in the magnitude of CO_2 and N fertilization and land use.

For these temperature-dependent model cases, we find that the model accounts for 17-86% of the variance of the residual flux (using low-pass filtering of both the model and the residual flux, as above). The fraction accounted for in the high land use cases is higher (74-86%) than in the low land use cases (17-54%),

Table 6.3: Best-fit parameters, errors, and land temperature feedback for cases described in Tables 6.1 and 6.2. Parameters are dimensionless unless otherwise noted.

Temperature-independent model			Temperature-dependent model					
Case	ε (or γ for -CN)[a]	Error[b]	Case	ε (or γ for -VN)[a]	Q_{10}	Error[b]	γ_{AB}[c] (PgC $^{o}C^{-1}$)	β_{AB}[d] (PgC ppm^{-1})
CHM-C	0.67 ± 0.01	0.0565	CHM-V	0.79 ± 0.02	4.91 ± 0.93	0.0449	-25.68	2.37
CLM-C	0.18 ± 0.01	0.0391	CLM-V	0.26 ± 0.01	3.98 ± 0.66	0.0313	-15.87	0.78
CHL-C	0.85 ± 0.01	0.0556	CHL-V	0.97 ± 0.02	4.95 ± 0.91	0.0444	-28.45	2.91
CHH-C	0.50 ± 0.01	0.0560	CHH-V	0.61 ± 0.02	4.74 ± 0.92	0.0455	-22.60	1.83
CLL-C	0.36 ± 0.01	0.0396	CLL-V	0.45 ± 0.01	4.12 ± 0.67	0.0310	-18.75	1.35
CLH-C	0.01 ± 0.01	0.0386	CLH-V	0.09 ± 0.01	3.78 ± 0.65	0.0317	-13.20	0.27
VHM-C	0.75 ± 0.01	0.0594	VHM-V	0.83 ± 0.02	3.30 ± 0.67	0.0531	-20.61	2.49
VLM-C	0.25 ± 0.01	0.0463	VLM-V	0.31 ± 0.02	2.73 ± 0.52	0.0423	-12.54	0.93
CHM-CN	0.025 ± 0.001	0.0363	CHM-VN	0.027 ± 0.001	1.52 ± 0.22	0.0353		
CLM-CN	0.007 ± 0.001	0.0329	CLM-VN	0.009 ± 0.001	2.78 ± 0.39	0.0277		

[a] Units of γ are $(PgC/year)^{-1}$

[b] Error measured as the square of the difference between the model and the residual flux, divided by the number of points. Units are $(ppm/yr)^2$

[c] We calculate the land feedback (γ_{AB}) as defined by Friedlingstein et al. (2003). We ran our model to 2100 using a prescribed atmospheric CO_2 based on the projected IPSL (L'Institut Pierre-Simon Laplace)-uncoupled CO_2 in Friedlingstein et al. (2003) and a prescribed temperature computed using Friedlingstein et al.s computed climate sensitivity to CO_2 ($\alpha = 0.0072$ K $ppmv^{-1}$). We ran this forward model with two cases: (1) using ϵ and Q_{10} from the temperature-dependent model, and (2) using all the same parameters except setting $Q_{10} = 1$. We then computed the difference in land carbon uptake between the cases and did a regression against temperature change to compute the feedback γ_{AB}. This approach allowed for the closest comparison to Friedlingstein et al.'s (2006) feedback analysis of the Coupled Climate-Carbon Cycle Model Intercomparison Project (C^4MIP) models. Further sensitivity studies showed that changes in α resulted in very little change in the feedback. Negative values of γ_{AB} denote carbon release to the atmosphere.

[d] We calculate the land flux sensitivity to CO_2 (β_{AB}), as defined by Friedlingstein et al. (2003) by taking results from the second case (see previous footnote) and regressing the cumulative land uptake against atmospheric CO_2.

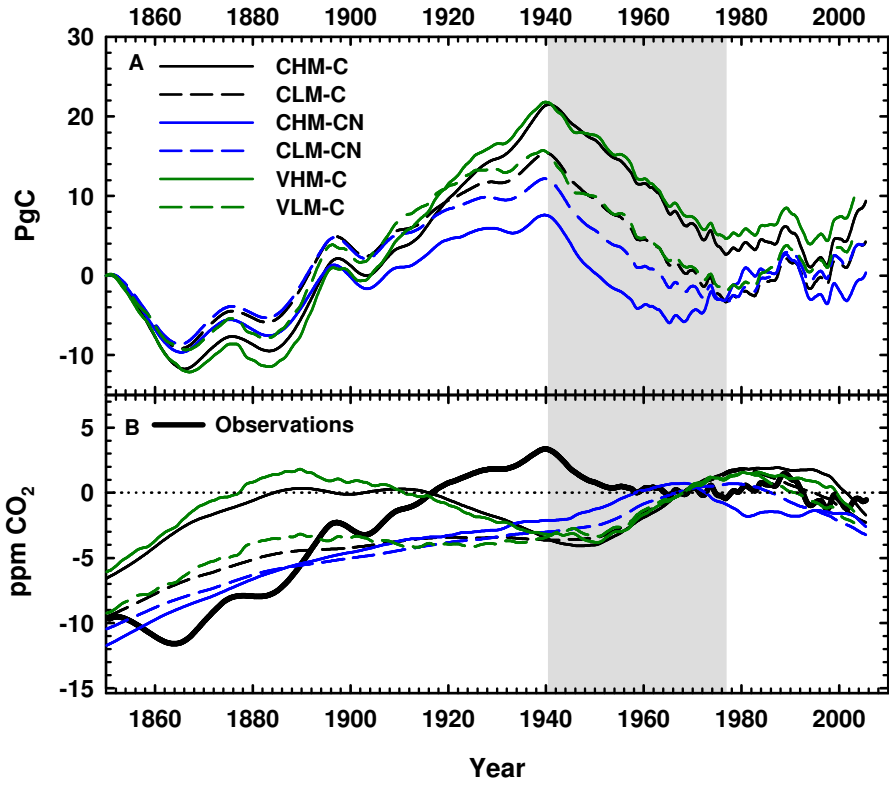

Figure 6.8: A. The integrated difference between the residual flux and temperature-independent model results for CO_2 fertilization (black and green) or N fertilization (blue). The residual flux was computed using high land use emissions (solid lines) or low land use emissions (dashed lines). For the green curves, the residual was computed using an ocean uptake that depended on SST. B. Constant airborne fraction anomaly of the atmospheric record and temperature-independent model results, computed by taking the difference between the atmospheric record and 57% of fossil fuel emissions. See Tables 6.1 and 6.2 for model definitions.

with much of the variance in the former cases coming from the long-term trend, as opposed to decadal variability.

Figure 6.9A shows the CO_2 anomalies (as in Figure 6.8A) for six of the ten temperature-dependent cases. These cases still show breaks in slope around 1940 and 1976, but the changes are less sharp than in the temperature-independent cases. These cases yield CAF anomalies (Figure 6.9B) that are generally similar to the standard case (CHM-V, shown also in Figure 6.7B). However, the high land use, N-fertilization case (CHM-VN) does a rather poor job of accounting for the trend from 1940-1960.

As an additional sensitivity test we subtract the best-fit linear trend from the temperature record, and fit ε (or γ) and Q_{10} using this new temperature record. We find that the correlation between the two fitted parameters (Q_{10} and ε or γ) is reduced from 0.70 $\pm$ 0.03 (mean and standard deviation of the cases presented in Table 6.3) to 0.33 $\pm$ 0.03, demonstrating that some of the correlation in the original temperature-dependent run was due to the long-term temperature trend. Using the detrended temperature record yields ε values only modestly smaller than when using the non-detrended temperature record, and estimates of Q_{10} that are still significantly larger than 1.0. Using the detrended temperature record, the quality of the fit is degraded slightly for most cases. Despite the high correlation between fitted parameters, we defend the non-detrended temperature record as being more biophysically reasonable, while acknowledging large uncertainties in parameter values.

As the specified turnover time of 2.5 years for the small box is somewhat arbitrary, we explore additional cases where the turnover time is varied from 1-20 years. This is accomplished by varying K_{a1} and K_{1a} while keeping the small box size constant (see Equations 6.2 and 6.3). We find that our ability to fit the decadal variability is not strongly dependent on the turnover time in this range. The best fits are obtained with turnover times in the range of 5-10 years, but improvements are modest relative to the 2.5 year case. Using time constants longer than 5 years yields seemingly unrealistic values of Q_{10} (17-44 for constant ocean temperature, CO_2 fertilization cases).

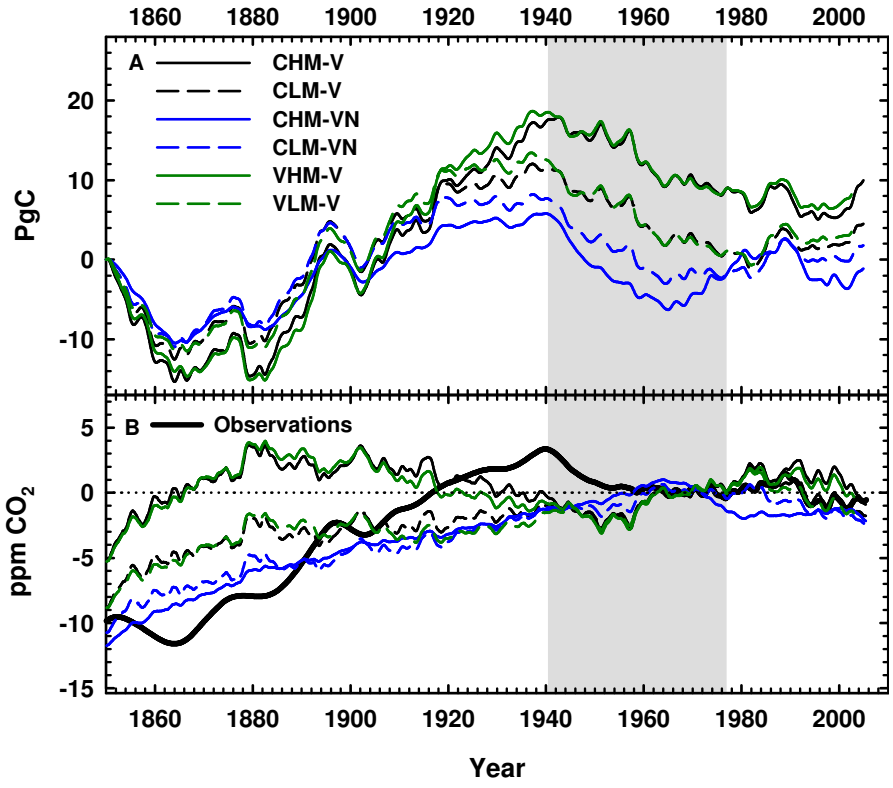

Figure 6.9: A. The integrated difference between the residual flux and temperature-dependent model results for CO_2 fertilization (black and green) or N fertilization (blue). The residual flux was computed using high land use emissions (solid lines) or low land use emissions (dashed lines). For the green curves, the residual was computed using an ocean uptake that depended on SST. B. Constant airborne fraction anomaly of the atmospheric record and temperature-dependent model results, computed by taking the difference between the atmospheric record and 57% of fossil fuel emissions. See Tables 6.1 and 6.2 for model definitions.

We also explore four alternate temperature records to drive our land model: 1) NPP-weighted global temperature, using an NPP mask from satellite Normalized Difference Vegetation Index (NDVI) data (James and Kalluri, 1994), 2) NPP-weighted Northern extratropical temperature (north of 23.5^{o}N), 3) NPP-weighted tropical temperature (23.5^{o}S - 23.5^{o}N) and 4) global SST. We apply these across all temperature-dependent model cases in Table 6.3. We find (results not shown) that the NPP-weighted temperature records and global SST yield slightly worse fits across most cases, but the differences from the fits using the original temperature record are small. The only exceptions are: 1) the Northern extratropical temperature record yields slightly better fits for the variable ocean temperature cases, and 2) the SST record yields slightly better fits for the CHL-V and CHM-VN cases.

Some studies of land box models have incorporated temperature-dependent photosynthesis (Dai and Fung, 1993; Jones et al., 2003). As an alternative, we ran our array of models using temperature-dependent photosynthesis instead of temperature-dependent respiration, replacing Equation 6.2 with:

$$F_{ai} = K_{ai} \times C^o_{atm} \times (1 + \varepsilon \Delta C_{atm}/C^o_{atm} + \gamma ff) \times (1 + \alpha \Delta T) \qquad (6.4)$$

where we fit α and ε or γ, and set $Q_{10} = 1$ in Equation 6.3. We find that these model fits are essentially identical to fits using Q_{10}, in having fitted values of ε or γ that are unchanged, and producing similar time-dependent fluxes. Optimum values of α in these fits are -0.13 to -0.15 $(^o\mathrm{C})^{-1}$, so the fits correspond to global average photosynthesis decreasing by 13-15% for a warming of 1^{o}C. The similarity between these model results and results fitting Q_{10} shows that, in the context of the available constraints, we cannot distinguish the signatures of reduced photosynthesis and enhanced respiration in the records.

In the results presented above, variability on the typical El Niño timescale of 3-7 years was removed by low-pass filtering the CO_2 record, forcing the box model to be optimized for longer timescales. Even though the model was not fit to the El Niño timescale, we find that our model can also account for much of the El Niño variability in the residual flux. Figure 6.10 shows the response of

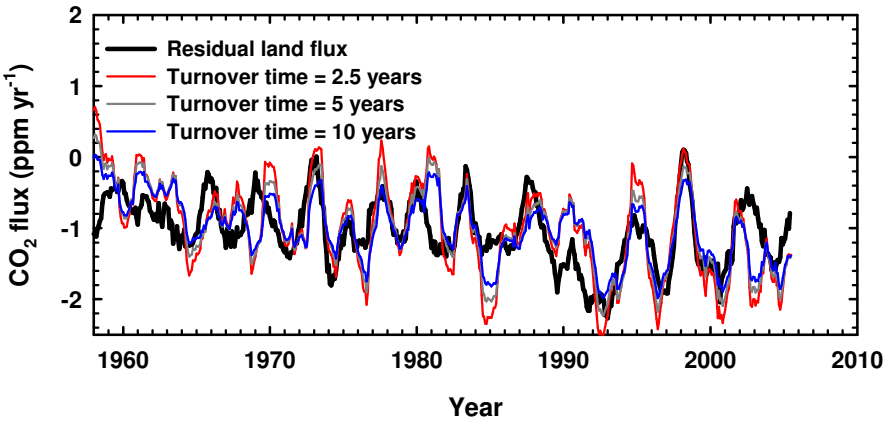

Figure 6.10: Unfiltered residual land flux, showing variability on short (e.g. El Niño) time scales. Also shown are unfiltered model results from the constant SST, high land use, CO_2 fertilization run (CHM-V) using a turnover time of 2.5, 5, or 10 years.

our standard model with the low-pass filtering removed (CHM-V, fit to match the filtered residual flux). The figure shows cases with turnover times of 2.5 to 10 years for the small box, against the unfiltered residual flux. As the turnover time is increased from 2.5 years to 10 years, the amplitude of the high frequency response diminishes. These unfiltered model results account for 34-39% of the variance in the unfiltered land uptake. A similar analysis using the other temperature-dependent model cases in Table 6.3 (with a 2.5 year turnover time) shows that in these cases, the model accounts for 18-46% of the variance, with the CHL-V model accounting for the highest fraction of the variance.

6.3.5 Adjustment of ice core data

As shown in Figure 6.9B, some model cases (e.g. CHM-V and VHM-V) show a rise in the late 1950s that was greater by around 2 ppm than indicated by the combined ice core and direct CO_2 records. One possible explanation for this feature is an offset between the ice core and direct records. The ice core record

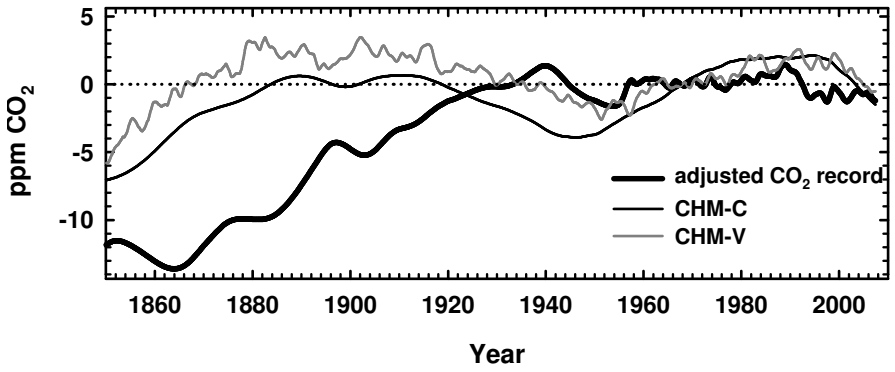

Figure 6.11: Constant airborne fraction anomaly of the atmospheric record and model results, with the ice core record shifted down 2 ppm. The anomaly was computed by taking the difference between the atmospheric record and 57% of fossil fuel emissions. Models have been updated through 2007 using the fitted parameters in Table 6.3. Fossil fuel emissions were updated using the most recent BP data (BP, 2008). The global land air temperature record was also updated using the most recent datasets (Brohan et al., 2006). Land use emissions were extended using the extrapolations described in Methods. See Tables 6.1 and 6.2 for model definitions.

has a reported uncertainty of 1.2 ppm (Etheridge et al., 1996), but this is clearly only a rough estimate and an offset in the ice core record as large as 2 ppm may be hard to firmly exclude.

To explore sensitivity to possible systematic errors in the ice core CO_2 record, we shifted the ice core record down by 2 ppm and refit our model to the adjusted data. The best-fit parameters give lower values for both ε and Q_{10}, and higher values of γ. As shown in Figure 6.11, the model now does a better job of reproducing the CO_2 record across the transition from the ice core to the direct records.

A discrepancy in 1958 might also arise due to our combining Antarctic data only (ice core record) before 1958 with the average of Antarctic (South Pole) and Mauna Loa data after 1958. However, in 1958, the difference in CO_2 concentration between Mauna Loa and the South Pole was only 0.4 ppm, which is too small to explain a 2 ppm offset.

6.4 Discussion

To balance the carbon budget over the past 150 years requires a residual flux not accounted for by fossil fuel emissions, ocean uptake, or land use change. As has long been known, this residual flux has the form of a sink that grows over time with multidecadal variability. The overall growth over time can be accounted for by CO_2 or N fertilization, but these processes appear unable to account for the observed patterns of multidecadal variability. The residual flux may have a contribution from errors in the fossil fuel emissions estimates, but fossil fuel emissions are too small to contribute much uncertainty before 1958. Uncertainty in emissions more recently (e.g. $\sim$1990s) is in the range of ± 0.4 to ± 0.6 PgC yr^{-1} (Marland and Rotty, 1984). What is most critical to our analysis, however, is uncertainty in the decadal growth rate of emissions. These uncertainties are not well quantified but certainly must be much smaller than ± 0.4 to ± 0.6 PgC yr^{-1}, and therefore likely of secondary importance. A greater contribution to uncertainty in the residual flux is uncertainty in land use emissions. Although the residual flux is not well constrained due to land use uncertainty, aspects of the multidecadal variability appear to be insensitive to uncertainties.

We have shown that the multidecadal variability in the residual flux since 1940 has a connection to the variations in global climate reflected in global land air temperatures. This connection is most evident when the residual flux is expressed as an anomaly relative to the uptake accounted for by either CO_2 or N fertilization (e.g. Figure 6.8A). Much of the variability in the residual land flux can be accounted for by a simple land box model driven by global land air temperature. Although we have represented the relationship between temperature and carbon fluxes using temperature-dependent respiration or photosynthesis, the temperature dependence in our model could also be interpreted as an expression of other processes tied to temperature, such as drought or fire. Sensitivity tests of our model suggest that the carbon pools active in the multidecadal exchanges have turnover times of 2.5-10 years. Although well-resolved, the multidecadal CO_2 fluxes are typically small compared to land use and fertilization fluxes, being at most 1 PgC yr^{-1} when averaged over 10 years.

Fluxes of carbon tied to variations in land temperature on multidecadal timescales may at least in part account for two prominent features of the CO_2 record. The plateau in CO_2 growth in the 1940s coincides with the period when temperatures stopped rising and became more constant. As shown in Figures 6.7 and 6.9, although we can see signs of this feature in our temperature-dependent model results, the modeled plateau is offset from observations by about 2 ppm, and does not show a faster rate of increase before 1940. We have shown that when we adjust the ice core record to account for a potential 2 ppm offset, the models better reproduce the record from 1940 to 1991 (Figure 6.11).

Our study also provides a context for understanding the constancy of the airborne fraction from 1958 to the present. Figures 6.6 and 6.9 demonstrate that our temperature-dependent models do a reasonable job of accounting for this constant airborne fraction. This constancy arises due to a cancellation of two effects. A reduction in the airborne fraction expected from the decrease in the growth rate of fossil fuel emissions around 1980 was compensated for by the enhanced land emissions due to a warming trend that began around the same time.

We find that the same model parameters can account for a significant fraction of the multidecadal and El Niño scale variability (Figure 6.10). Zhang et al. (1997) have shown that the physical climate system (e.g. SST and sea-level pressure) exhibits very similar spatial variability on decadal and interannual timescales, suggesting a close connection between the phenomenology operating on these distinct timescales. Our model results suggest that the same may be true of the carbon responses: multidecadal and interannual variability may simply be different manifestations of the same underlying phenomenology.

A link with El Niño supports our assumption that the multidecadal variability may be attributed primarily to land biosphere exchange. While the ocean and land both contribute to El Niño CO_2 variability, the land component has been shown to dominate, with the ocean component tending to oppose rather than reinforce the pattern (Keeling and Revelle, 1985; Nakazawa et al., 1997; Le Quéré et al., 2003). An extension of the oceanic component of El Niño to multidecadal timescales would presumably similarly oppose the decadal CO_2 variability. A link

to land processes is also suggested by the relative success of our regressions using different temperature records, which showed that using the land temperature records yielded the best fits, while the SST record yielded inferior fits for many cases. Our interpretation, which attributes the plateau in the 1940s mostly to land processes is at odds, however, with the analysis of Trudinger et al. (2005), who attribute this feature to enhanced ocean uptake based on ice core δ^{13}C data.

Several recent studies have shown that biomass burning may be a substantial driver of the El Niño CO_2 variability (Langenfelds et al., 2002; van der Werf et al., 2004; Randerson et al., 2005). It is possible that fires could also contribute to the variations that we see on decadal timescales, but we lack records extending back to the early 20th century to test this notion.

Despite our sensitivity analysis, it remains possible that some of the multidecadal variability in CO_2 is tied to human activities. Although temperature-dependent processes on land may account for much of the anomalous CO_2 variability after 1940, it is not clear that these processes are adequate to account for anomalous fluxes before 1940. The suite of models considered here consistently underestimates the CO_2 increase from 1900 to 1940, suggesting there is a missing source of CO_2 over this period. Our results are consistent with a recent study by Ricciuto et al. (2008), which also showed difficulty reproducing the CO_2 record from 1900-1950 using a similar model. The difficulty could be due to errors in the land use emissions estimates in the early part of the 20th century. Decadal variability in land use emission is not well known, and could be as large as the multidecadal fluxes resolved here (McGuire et al., 2001). The land use emissions estimates of Houghton are computed based on reported land use statistics, and do not account for a range of human impacts on land that may be tied to climate, such as biomass burning. Nepstad et al. (1999) have shown that burning of downed biomass increases during El Niño-induced droughts. More work is needed to determine the importance of these influences globally and on multidecadal timescales. The difficulty in accounting for the rise from 1900 to 1940 may also result from an overestimation of land or ocean CO_2 sinks over this period. If so, this suggests that some of the processes controlling the long-term behavior of these sinks are

poorly understood.

Several studies have called attention to the possibility that recent high growth rate in CO_2 may be partly due to decreasing efficiency of CO_2 sinks (Canadell et al., 2007; Le Quéré et al., 2007). In Figure 6.11, we update the records through the end of 2007 to explore the possibilities of any very recent anomalies. Fossil fuel emissions were updated using the most recent BP data (BP, 2008). The global land air temperature record was also updated using the most recent datasets (Brohan et al., 2006). Land use emissions were extended using the extrapolations described in Methods. The model was run through 2007 using the fitted parameters listed in Table 6.3. The largest discrepancy is seen after 1991, when the anomaly fell faster than the model predictions. This feature is almost certainly accounted for by the climate impacts of the eruption of Mt. Pinatubo, which produced large biospheric carbon fluxes via processes not adequately represented in our model. However, the discrepancy decreases in recent years, consistent with a recovery from past perturbations. At the end of 2007, the temperature-dependent model has only a 0.5 ppm offset from the CO_2 record, showing that there are no outstanding recent discrepancies.

The relationship between the multidecadal variability of CO_2 and temperature implies a positive climate feedback. A metric for quantifying this feedback during transient warming has been developed by Friedlingstein et al. (2003, 2006), and applied across the Coupled Climate-Carbon Cycle Model Intercomparison Project (C^4MIP) models. This metric gives the change in land carbon storage in PgC per ^oC change in temperature. We derive this metric for our models, and find a range of -12.54 to -28.45 PgC $^oC^{-1}$ (Table 6.3), which is on the low end of the -20 to -177 PgC $^oC^{-1}$ reported for the C^4MIP models (Friedlingstein et al., 2006). Our results therefore indicate that the multidecadal variability that is resolvable in the CO_2 records is related to processes that, by themselves, do not imply a large climate feedback.

Similarly, we compute the land flux sensitivity to atmospheric CO_2 using a metric defined by Friedlingstein et al. (2003, 2006). We find a sensitivity of 0.27 to 2.91 PgC per ppm atmospheric CO_2 (Table 6.3). The C^4MIP models give a

similar range of 0.2 to 2.8 PgC ppm^{-1} (Friedlingstein et al., 2006). However, most of the C^4MIP models have a sensitivity between 1.1 and 1.6 PgC ppm^{-1}, whereas for most of our cases, the sensitivity is less than 1 PgC ppm^{-1} or greater than 2 PgC ppm^{-1}, tied to the high and low land use scenarios that we employ.

An important caveat is that our analyses are only able to resolve the temperature sensitivity of the short-lived carbon pools and do not address the possibility of feedbacks tied to longer-lived carbon pools. There is no reason to discount a possible temperature sensitivity of longer-lived pools (Fang et al., 2006). Some studies suggest that long-lived pools may be at least as sensitive to temperature as short-lived pools (Knorr et al., 2005; Conant et al., 2008). However, the climate sensitivity of long-lived pools cannot be readily discerned in the global records over the past century because of confounding uncertainties in land use emissions and processes which may lead to carbon uptake on long timescales, such as CO_2 or N fertilization.

6.5 Conclusions

A two-box land model with a carbon flux driven by CO_2 or N fertilization and temperature-dependent respiration shows that multidecadal variations in the land CO_2 sink can be partly explained by variations in temperature, possibly through processes such as temperature-dependent respiration or fires. This response of land carbon uptake to temperature can help explain the constancy of the airborne fraction since 1980. Our analysis highlights the possibility that the ice core records might be in error by as much as 2 ppm. By allowing for a potential 2 ppm error in the ice core CO_2 record, the CO_2 plateau in the 1940s can be partly explained as well, but the record before 1940 is not well represented. Our analysis does not point to any large recent changes in the behavior of the global carbon sinks. Furthermore, the model suggests a connection between multidecadal variability and variability on El Niño timescales, supporting the conclusion that the multidecadal variability can be attributed to carbon exchanges in the land biosphere.

The model results suggest that the multidecadal variability in the atmospheric CO_2 record can be partly accounted for by exchanges with carbon pools with relatively short turnover times in the range of 2.5-10 years. The multidecadal responses are in the direction of positive climate feedback, i.e. warming causing additional CO_2 increase, but the exchange that we attribute to these short-lived carbon pools may be too small to constitute a significant climate feedback. The global CO_2 records appear insufficient to determine the response of carbon pools with longer turnover times because of the confounding uncertainties in land use emissions and CO_2 or N fertilization. Improving our understanding of the short-term responses, along with improved constraints on the land use and fertilization effects, will be important for resolving the signature of any long-term carbon pools in the global CO_2 record.

6.6 Acknowledgements

We thank Tim Barnett for his helpful comments. This work was supported by a grant from BP, by the National Science Foundation under Grant No. ATM-0632770, the U.S. Department of Energy under grant DE-FG02 07ER64362, the National Aeronautics and Space Administration under grant NNG06GB98B, and a National Science Foundation Graduate Research Fellowship.

This chapter, in full, is a reprint of material previously published as "Climate effects on atmospheric carbon dioxide over the last century," by Lauren Elmegreen Rafelski, Stephen C. Piper, and Ralph F. Keeling, in *Tellus*, 2009, Vol, 61B, pp. 718-731. I was the primary investigator and author of this paper.

References

Achard, F., Eva, H. D., Stibig, H.-J., Mayaux, P., Gallego, J., Richards, T., and Malingreau, J.-P., 2002: Determination of deforestation rates of the world's humid tropical forests. *Science*, **297**, 999–1002.

Bacastow, R., and Keeling, C., 1979: Models to predict future atmospheric CO_2 concentrations. In *Workshop on the Global Effects of Carbon Dioxide from Fossil Fuels*, editors W. P. Elliott, and L. Machta, 72–90. U.S. Department of Energy, Washington, D. C.

Bacastow, R., and Keeling, C. D., 1973: Atmospheric carbon dioxide and radiocarbon in the natural carbon cycle: II. Changes from A.D. 1700 to 2070 as deduced from a geochemical model. In *Carbon and the Biosphere*, editors G. M. Woodwell, and E. V. Pecan, 86–135. United States Atomic Energy Commission, Springfield, VA.

Bolin, B., 1986: How much CO_2 will remain in the atmosphere? In *SCOPE 29: The Greenhouse Effect, Climate Change, and Ecosystems*, editors B. Bolin, B. R. Doos, J. Jager, and R. A. Warrick, 93–155. John Wiley & Sons, Chichester.

BP, 2008: *BP statistical review of world energy June 2008.* British Petroleum, P.L.C., London.

Brohan, P., Kennedy, J. J., Harris, I., Tett, S. F. B., and Jones, P. D., 2006: Uncertainty estimates in regional and global observed temperature changes: A new data set from 1850. *Journal of Geophysical Research*, **111**(D12106), doi:10.1029/2005JD006548.

Canadell, J. G., Le Quéré, C., Raupach, M. R., Field, C. B., Buitenhuis, E. T., Ciais, P., Conway, T. J., Gillett, N. P., Houghton, R. A., and Marland, G., 2007: Contributions to accelerating atmospheric CO_2 growth from economic activity, carbon intensity, and efficiency of natural sinks. *Proceedings of the National Academy of Sciences, USA*, **104**(47), 18866–18870.

Conant, R. T., Drijber, R. A., Haddix, M. L., Parton, W. J., Paul, E. A., Plante, A. F., Six, J., and Steinweg, J. M., 2008: Sensitivity of organic matter decomposition to warming varies with its quality. *Global Change Biology*, **14**, 868–877.

Cox, P. M., Betts, R. A., Jones, C. D., Spall, S. A., and Totterdell, I. J., 2000: Acceleration of global warming due to carbon-cycle feedbacks in a coupled climate model. *Nature*, **408**, 184–187.

Cramer, W., Bondeau, A., Woodward, F. I., Prentice, I. C., Betts, R. A., Brovkin, V., Cox, P. M., Fisher, V., Foley, J. A., Friend, A. D., Kucharik, C., Lomas, M. R., Ramankutty, N., Sitch, S., Smith, B., White, A., and Young-Molling, C., 2001: Global response of terrestrial ecosystem structure and function to CO_2 and climate change: Results from six dynamic global vegetation models. *Global Change Biology*, **7**, 357–373.

Dai, A., and Fung, I. Y., 1993: Can climate variability contribute to the "missing" CO_2 sink? *Global Biogeochemical Cycles*, **7**(3), 599–609.

DeFries, R. S., Houghton, R. A., Hansen, M. C., Field, C. B., Skole, D., and Townshend, J., 2002: Carbon emissions from tropical deforestation and regrowth based on satellite observations for the 1980s and 1990s. *Proceedings of the National Academy of Sciences, USA*, **99**(22), 14256–14261.

DeLucia, E. H., Hamilton, J. G., Naidu, S. L., Thomas, R. B., Andrews, J. A., Finzi, A., Lavine, M., Matamala, R., Mohan, J. E., Hendrey, G. R., and Schlesinger, W. H., 1999: Net primary production of a forest ecosystem with experimental CO_2 enrichment. *Science*, **284**, 1177–1179.

Denman, K. L., Brasseur, G., Chidthaisong, A., Ciais, P., Cox, P. M., Dickinson, R. E., Hauglustaine, D., Heinze, C., Holland, E., Jacob, D., Lohmann, U., Ramachandran, S., da Silva Dias, P. L., Wofsy, S. C., and Zhang, X., 2007: Couplings between changes in the climate system and biogeochemistry. In *Climate change 2007: The physical science basis. Contribution of Working Group I to the Fourth Assessment Report of the Intergovernmental Panel on Climate Change*, editors S. Solomon, D. Qin, M. Manning, Z. Chen, M. Marquis, K. B. Averyt, M. Tignor, and H. L. Miller. Cambridge University Press, Cambridge, United Kingdom and New York, NY, USA.

Etheridge, D. M., Steele, L. P., Langenfelds, R. L., Francey, R. J., Barnola, J.-M., and Morgan, V. I., 1996: Natural and anthropogenic changes in atmospheric CO_2 over the last 1000 years from air in Antarctic ice and firn. *Journal of Geophysical Research*, **101**(D2), 4115–4128.

Fang, C., Smith, P., and Smith, J. U., 2006: Is resistant soil organic matter more sensitive to temperature than the labile organic matter? *Biogeosciences*, **3**, 65–68.

Friedlingstein, P., Cox, P., Betts, R., Bopp, L., von Bloh, W., Brovkin, V., Cadule, P., Doney, S., Eby, M., Fung, I., Bala, G., John, J., Jones, C., Joos, F., Kato, T., Kawamiya, M., Knorr, W., Lindsay, K., Matthews, H. D., Raddatz, T.,

Rayner, P., Reick, C., Roeckner, E., Schnitzler, K.-G., Schnur, R., Strassmann, K., Weaver, A. J., Yoshikawa, C., and Zeng, N., 2006: Climate-carbon cycle feedback analysis: Results from the C^4MIP model intercomparison. *Journal of Climate*, **19**(3337-3353).

Friedlingstein, P., Dufresne, J.-L., Cox, P. M., and Rayner, P., 2003: How positive is the feedback between climate change and the carbon cycle? *Tellus*, **55B**, 692–700.

Galloway, J. N., and Cowling, E. B., 2002: Reactive nitrogen and the world: 200 years of change. *Ambio*, **31**(2), 64–71.

Houghton, R. A., 1995: Effects of land-use change, surface temperature, and CO_2 concentration on terrestrial stores of carbon. In *Biotic Feedbacks in the Global Climatic System: Will the Warming Feed the Warming?*, editors G. M. Woodwell, and F. T. Mackenzie, 333–350. Oxford University Press, New York.

Houghton, R. A., 2003: Revised estimates of the annual net flux of carbon to the atmosphere from changes in land use and land management 1850-2000. *Tellus*, **55B**, 378–390.

Houghton, R. A., 2007: Balancing the global carbon budget. *Annual Review of Earth and Planetary Sciences*, **35**, 313–347.

House, J. I., Prentice, I. C., Ramankutty, N., Houghton, R. A., and Heimann, M., 2003: Reconciling apparent inconsistencies in estimates of terrestrial CO_2 sources and sinks. *Tellus*, **55B**, 345–363.

Jain, A. K., and Yang, X., 2005: Modeling the effects of two different land cover change data sets on the carbon stocks of plants and soils in concert with CO_2 and climate change. *Global Biogeochemical Cycles*, **19**(GB2015), doi:10.1029/2004GB002349.

James, M. E., and Kalluri, S. N. V., 1994: The Pathfinder AVHRR land data set: An improved coarse resolution data set for terrestrial monitoring. *International Journal of Remote Sensing*, **15**, 3347–3363.

Jones, C. D., Cox, P., and Huntingford, C., 2003: Uncertainty in climate-carbon-cycle projections associated with the sensitivity of soil respiration to temperature. *Tellus*, **55B**, 642–648.

Jones, C. D., and Cox, P. M., 2005: On the significance of atmospheric CO_2 growth rate anomalies in 2002-2003. *Geophysical Research Letters*, **32**(L14816), doi:10.1029/2005GL023027.

Joos, F., Bruno, M., Fink, R., Siegenthaler, U., Stocker, T. F., Le Quéré, C., and Sarmiento, J. L., 1996: An efficient and accurate representation of complex oceanic and biospheric models of anthropogenic carbon uptake. *Tellus*, **48B**, 397–417.

Keeling, C. D., Bacastow, R. B., Carter, A. F., Piper, S. C., Whorf, T. P., Heimann, M., Mook, W. G., and Roeloffzen, H., 1989: A three-dimensional model of atmospheric CO_2 transport based on observed winds: 1. Analysis of observational data. In *Aspects of Climate Variability in the Pacific and the Western Americas*, editor D. H. Peterson, Geophysical Monograph Series, 165–236. American Geophysical Union, Washington, D.C.

Keeling, C. D., and Revelle, R., 1985: Effects of El Niño/Southern Oscillation on the atmospheric content of carbon dioxide. *Meteoritics*, **20**(2), 437–450.

Keeling, C. D., Whorf, T. P., Wahlen, M., and van der Plicht, J., 1995: Interannual extremes in the rate of rise of atmospheric carbon dioxide since 1980. *Nature*, **375**, 666–670.

Knorr, W., Prentice, I. C., House, J. I., and Holland, E. A., 2005: Long-term sensitivity of soil carbon turnover to warming. *Nature*, **433**, 298–301.

Langenfelds, R. L., Francey, R. J., Pak, B. C., Steele, L. P., Lloyd, J., Trudinger, C. M., and Allison, C. E., 2002: Interannual growth rate variations of atmospheric CO_2 and its $\delta^{13}C$, H_2, CH_4, and CO between 1992 and 1999 linked to biomass burning. *Global Biogeochemical Cycles*, **16**(3), 1048, doi:10.1029/2001GB001466.

Le Quéré, C., Aumont, O., Bopp, L., Bousquet, P., Ciais, P., Francey, R., Heimann, M., Keeling, C. D., Keeling, R. F., Kheshgi, H., Peylin, P., Piper, S. C., Prentice, I. C., and Rayner, P. J., 2003: Two decades of ocean CO_2 sink and variability. *Tellus*, **55B**, 649–656.

Le Quéré, C., Rödenbeck, C., Buitenhuis, E. T., Conway, T. J., Langenfelds, R., Gomez, A., Labuschagne, C., Ramonet, M., Nakazawa, T., Metzl, N., Gillett, N., and Heimann, M., 2007: Saturation of the Southern Ocean CO_2 sink due to recent climate change. *Science*, **316**, 1735–1738.

MacFarling Meure, C., Etheridge, D., Trudinger, C., Steele, P., Langenfelds, R., van Ommen, T., Smith, A., and Elkins, J., 2006: Law Dome CO_2, CH_4, and N_2O ice core records extended to 2000 years BP. *Geophysical Research Letters*, **33**(L14810), doi:10.1029/2006GL026152.

Magnani, F., Mencuccini, M., Borghetti, M., Berbigier, P., Berninger, F., Delzon, S., Grelle, A., Hari, P., Jarvis, P. G., Kolari, P., Kowalski, A. S., Lankreijer, H., Law, B. E., Lindroth, A., Loustau, D., Manca, G., Moncrieff, J. B., Rayment,

M., Tedeschi, V., Valentini, R., and Grace, J., 2007: The human footprint in the carbon cycle of temperate and boreal forests. *Nature*, **447**, 848–850.

Manning, A. C., and Keeling, R. F., 2006: Global oceanic and land biotic carbon sinks from the Scripps atmospheric oxygen flask sampling network. *Tellus*, **58B**, 95–116.

Marland, G., Boden, T. A., and Andres, R. J., 2006: Global, regional, and national CO_2 emissions. In *Trends: A Compendium of Data on Global Change*. Carbon Dioxide Information Analysis Center, Oak Ridge National Laboratory, U. S. Department of Energy, Oak Ridge, Tenn., U.S.A.

Marland, G., and Rotty, R. M., 1984: Carbon dioxide emissions from fossil fuels: A procedure for estimation and results for 1950-1982. *Tellus*, **36B**, 232–261.

McGuire, A. D., Sitch, S., Clein, J. S., Dargaville, R., Esser, G., Foley, J., Heimann, M., Joos, F., Kaplan, J., Kicklighter, D. W., Meier, R. A., Melillo, J. M., Moore III, B., Prentice, I. C., Ramankutty, N., Reichenau, T. G., Schloss, A., Tian, H., Williams, L. J., and Wittenberg, U., 2001: Carbon balance of the terrestrial biosphere in the twentieth century: Analysis of CO_2, climate and land use effects with four process-based ecosystem models. *Global Biogeochemical Cycles*, **15**(1), 183–206.

Nakazawa, T., Morimoto, S., Aoki, S., and Tanaka, M., 1997: Temporal and spatial variations of the carbon isotopic ratio of atmospheric carbon dioxide in the western Pacific region. *Journal of Geophysical Research*, **102**(D1), 1271–1285.

Nepstad, D. C., Verissimo, A., Alencar, A., Nobre, C., Lima, E., Lefebvre, P., Schlesinger, P., Potter, C., Moutinho, P., Mendoza, E., Cochrane, M., and Brooks, V., 1999: Large-scale impoverishment of Amazonian forests by logging and fire. *Nature*, **398**, 505–508.

Oeschger, H., and Heimann, M., 1983: Uncertainties of predictions of future atmospheric CO_2 concentrations. *Journal of Geophysical Research*, **88**(C2), 1258–1262.

Pearman, G. I., Etheridge, D., de Silva, F., and Fraser, P. J., 1986: Evidence of changing concentrations of atmospheric CO_2, N_2O and CH_4 from air bubbles in Antarctic ice. *Nature*, **320**, 248–250.

Plattner, G.-K., Joos, F., Stocker, T. F., and Marchal, O., 2001: Feedback mechanisms and sensitivities of ocean carbon uptake under global warming. *Tellus*, **53B**, 564–592.

Randerson, J. T., van der Werf, G. R., Collatz, G. J., Giglio, L., Still, C. J., Kasibhatla, P., B., M. J., White, J. W. C., DeFries, R. S., and Kasischke, E. S., 2005: Fire emissions from C_3 and C_4 vegetation and their influence on interannual variability of atmospheric CO_2 and $\delta^{13}CO_2$. *Global Biogeochemical Cycles*, **19**(GB2019), doi:10.1029/2004GB002366.

Ricciuto, D. M., Davis, K. J., and Keller, K., 2008: A Bayesian calibration of a simple carbon cycle model: The role of observations in estimating and reducing uncertainty. *Global Biogeochemical Cycles*, **22**(GB2030), doi:10.1029/2006GB002908.

Sabine, C. L., Feely, R. A., Gruber, N., Key, R. M., Lee, K., Bullister, J. L., Wanninkhof, R., Wong, C. S., Wallace, D. W. R., Tilbrook, B., Millero, F. J., Peng, T.-H., Kozyr, A., Ono, T., and Rios, A. F., 2004: The oceanic sink for anthropogenic CO_2. *Science*, **305**, 367–371.

Siegenthaler, U., and Oeschger, H., 1987: Biospheric CO_2 emissions during the past 200 years reconstructed by deconvolution of ice core data. *Tellus*, **39B**, 140–154.

Townsend, A. R., Braswell, B. H., Holland, E. A., and Penner, J. E., 1996: Spatial and temporal patterns in terrestrial carbon storage due to deposition of fossil fuel nitrogen. *Ecological Applications*, **6**(3), 806–814.

Trudinger, C., Enting, I., Etheridge, D., Francey, R., and Rayner, P., 2005: The carbon cycle over the past 1000 years inferred from the inversion of ice core data. In *A History of Atmospheric CO_2 and its Effects on Plants, Animals, and Ecosystems*, editors J. R. Ehleringer, T. E. Cerling, and M. D. Dearing, Ecological Studies, 329–349. Springer, New York.

van der Werf, G. R., Randerson, J. T., Collatz, G. J., Giglio, L., Kasibhatla, P. S., Arellano, A. F., Jr., Olsen, S. C., and Kasischke, E. S., 2004: Continental-scale partitioning of fire emissions during the 1997 to 2001 El Niño/La Niña period. *Science*, **303**, 73–76.

Zhang, Y., Wallace, J. M., and Battisti, D. S., 1997: ENSO-like interdecadal variability: 1900-93. *Journal of Climate*, **10**, 1004–1020.